UiT
THE ARCTIC UNIVERSITY OF NORWAY

Faculty of Science and Technology

Department of Geosciences

Late Miocene Ice Rafting in the Iceland Sea

-Evidence from coarse fraction analysis of ODP Site 907-

Rebekka Dischington

Geo-3900 Master's thesis in geology

May 2018

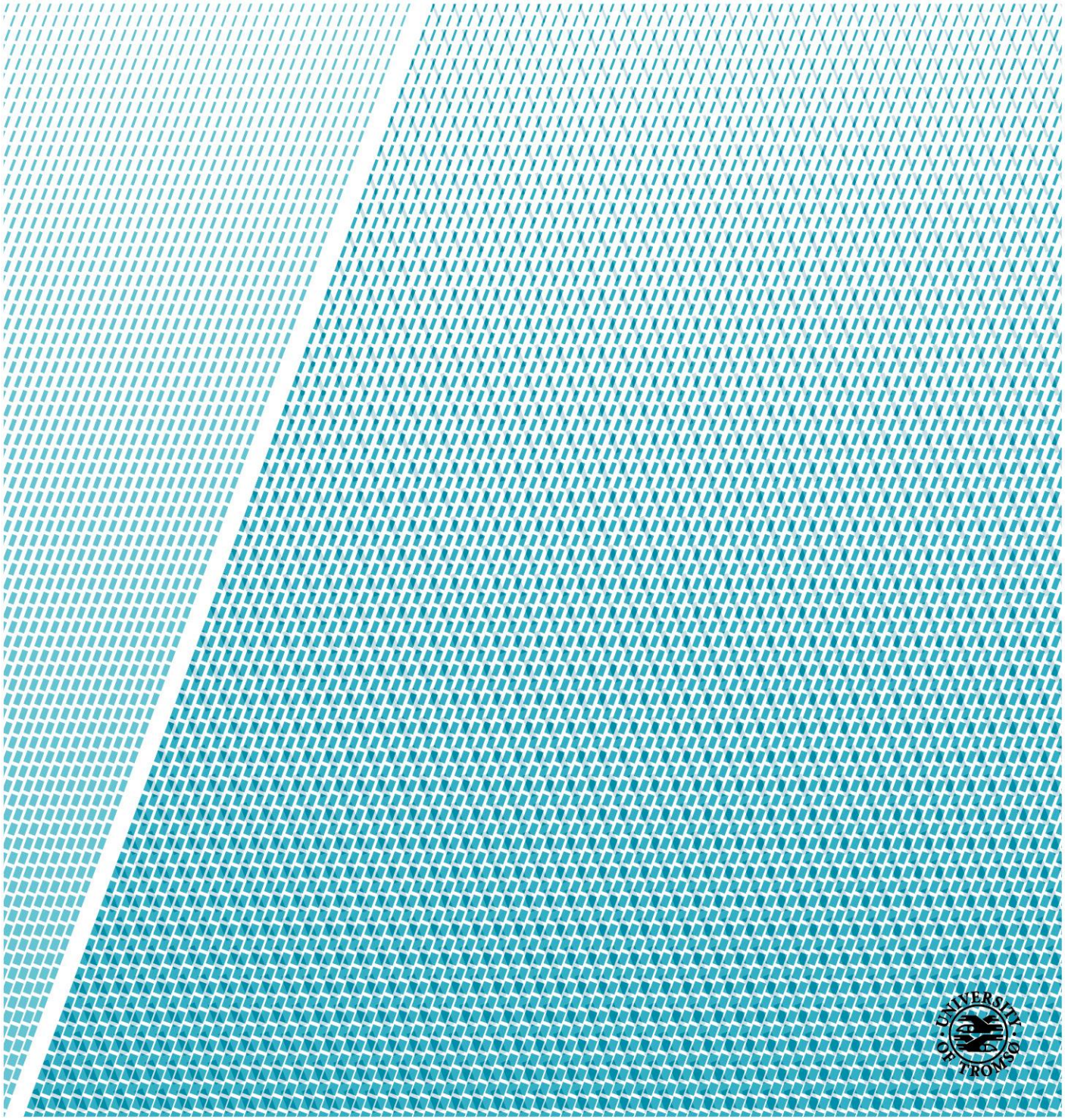

Abstract

A high-resolution sedimentary record from ODP Leg 151 Hole 907A has been investigated with sedimentological and geochemical methods to study the paleoenvironmental evolution of the Iceland Sea over a 1-Myr time interval in the Late Miocene. Climate deterioration characterizes the Neogene period, culminating in a transition to bipolar glaciations in the Late Pliocene (Thiede and Myhre, 1996). Ice rafting has been reported in the Iceland Sea back to ~8 Ma (Fronval and Jansen, 1996). Despite evidence of older IRD pulses from several other high northern latitude sites (e.g. Helland and Holmes, 1997, Winkler et al., 2002), IRD analyses has not been carried out further back in time.

This thesis extends the IRD record beyond 8 Ma and reveals continuous ice rafting in the Iceland Sea between 11 to 9.98 Ma as suggested by the common occurrence of coarse-fraction terrigenous sediment (>125 μm) throughout the studied interval in ODP Hole 907A. Surface texture analysis of sand-sized quartz grains (250–1000 μm) indicates iceberg transport of IRD to the Iceland Sea during the early Late Miocene. The IRD observed in this study has been related to small-scale glaciers on Greenland large enough to reach sea level in the Late Miocene. This is supported by a similar source proposed for IRD at Irminger Basin ODP Site 918 at the same time (Helland and Holmes, 1997). A southwards flowing East Greenland Current-precursor was presumably established (Wei, 1998) and may have transported icebergs to the study site.

In addition, coarse fraction analysis reveals a biological turnover at 10.4 Ma, which coincides with changes observed in diatom and dinoflagellate cyst assemblages at ODP Site 907 (Stabell and Koç, 1996; Schreck et al., 2013). The biological turnover corresponds to maxima in quartz grain abundance and a significant coarsening of the bulk sediment grain-size, which may reflect intensified ice rafting at around 10.4 Ma. The timing of the changes observed in ODP Hole 907A correspond favourably to a short-term global Miocene cooling event (Mi-6 event, 10.7–10.4 Ma, Westerhold et al., 2005), thus, this thesis provides the first direct indications for the Mi-6 event in the high northern latitudes.

Acknowledgements

I would first and foremost like to thank my supervisor, Michael Schreck, for the opportunity to write this thesis. Thank you for all the help and good advice, and for always taking time to answer questions. Your help has been invaluable.

I also want to thank the co-supervisor of this thesis, Matthias Forwick, for all advice and the open office policy.

Further, I would like to thank Trine, Karina, and Ingvild at the Geoscience Laboratory. Especially Trine, for productive consultations on how to proceed with a rather challenging sediment.

I want to thank my geology friends for five amazing years in Tromsø!

I also want to thank my family for being my biggest support through these five years. I especially want to thank Daniela, for helping me with the final corrections on this thesis, you are amazing!!

Last but not least, I want to thank my boyfriend Richard, for supporting me and keeping my motivation up through this whole year. And also for picking me up after long days and bringing me food and snacks. You are my rock!

Rebekka Dischington

Tromsø 15.05.2018

Table of Contents

1 Introduction 1
1.1 Objectives 2
1.2 Background 3
1.2.1 Study Area 3
1.2.2 Present-day Ocean Circulation in the Norwegian-Greenland Sea 3
1.2.3 Plate Tectonic Evolution of the Norwegian-Greenland Sea 6
1.2.4 Miocene Paleoenvironmental Evolution 9
2 Material and Methods 15
2.1 Data collected by the Shipboard Scientific Party 15
2.1.1 Coring 15
2.1.2 Lithology 15
2.1.3 Age control 18
2.1.4 Sediment sampling 19
2.2 Laboratory work 20
2.2.1 Geochemical bulk parameters 20
2.2.2 Particle size analysis using coulter counter 21
2.2.3 Wet sieving 23
2.2.4 Coarse fraction analysis 23
2.2.5 Surface Textural Analysis of Quartz 24
3 Results 27
3.1 Geochemical bulk parameters 27
3.2 Grain size Distribution 27
3.2.1 Temporal variation of grain size distribution 30
3.3 Coarse Fraction Description 32
3.3.1 Sediment Composition 32
3.3.2 Relative Abundance of Sediment Components 34
3.3.3 Temporal Variation of Sediment Components 35

3.4 Surface Texture Analysis of Quartz 41
4 Discussion 45
4.1 A 1-Myr record of ice rafting in the Iceland Sea 45
4.1.1 Iceberg or Sea Ice Rafted Debris 46
4.1.2 Late Miocene IRD in the Norwegian-Greenland Sea 49
4.2 Rare Pumice Occurrence— possible indications of surface currents? 50
4.3 Biological Turnover 50
4.4 Iceland Sea cooling and ice rafting in response to the Mi-6 event 52
5 Conclusions 55
6 Future Work 57
Works cited 61
Appendix 66

List of Tables

Table 1: Grain size classification used to describe grain sizes. After Wentworth (1922). 22
Table 2: Categories used to describe the coarse fraction composition in ODP Hole 907A. 23
Table 3: Surface textures used to describe individual quartz grains in ODP Hole 907A. 25
Table 4: Minimum, maximum and average wt.% of TC, TOC and $CaCO_3$ in cores 13H and 14H.... 27
Table 5: Comparison of results obtained from coulter counter analysis and sieving. 29
Table 6: The abundance (%) of microfeatures in quartz grains in ODP Hole 907A. 41

List of Figures

Figure 1: Map of the Norwegian-Greenland Sea, showing ODP Sites and ocean surface currents. 4
Figure 2: Illustration thermohaline circulation. 6
Figure 3: Map of the fundamental bathymetrical features of the Norwegian-Greenland Sea. 7
Figure 4: The plate tectonic evolution of the Fram Strait 9
Figure 5: Global oxygen isotope record, position of Mi-events and Miocene IRD occurrences 11
Figure 6: Lithological logs for cores 13H and 14H of ODP Hole 907A. 17
Figure 7: Age/depth plot for ODP Hole 907A. 18
Figure 8: Flow chart illustrating the order of procedures during analysis. 20
Figure 9: TC, TOC, and $CaCO_3$ content (wt.%) and grains size distribution 28
Figure 10:Coulter counter grain size distribution. 31
Figure 11: Sieving grain size distribution. 32
Figure 12: Examples of coarse fraction sediment components. 33
Figure 13: Abundance of various sediment components 34
Figure 14: Temporal variation of volcanoclastic and terrigenous components. 39
Figure 15: Temporal variation of biogenic components 40
Figure 16: Temporal variation of authigenic and unidentified components 40
Figure 17: Position of samples and results of quartz surface texture analysis. 42
Figure 18: SEM micrographs of representative quartz surface texture analysis. 44
Figure 19: Comparison of results from this thesis to other proxy records 46
Figure 20: Quartz micro-textures typical for differen environments 47
Figure 21: Figure summarizing the conclusions of this thesis 52

1 Introduction

The modern global climate is characterized by a steep latitudinal temperature gradient, with a warm equator and freezing poles. Ice sheets on the Antarctic continent and on Greenland accentuates the extremes of present day climate. The polar regions have been glaciated several times through the Cenozoic (66–0 Ma), while the transition from "Greenhouse" to "Icehouse" global climate conditions in the Early Oligocene (33.9–28.1 Ma) ultimately initiated a stepwise long-term cooling and descent into a bipolar glaciated world in the Late Pliocene (Katz et al., 2008). The cause of this unique global climate transition remains uncertain, however several mechanisms such as topographic uplift and drawdown of atmospheric CO_2 (Raymo, 1994), variations in the Earths orbital parameters (e.g. Lourens and Hilgen, 1997), and opening and closing of oceanic gateways (Wright and Miller, 1996) have been suggested.

The Arctic cryosphere is very sensitive to climatic change, as indicated by high-frequency ice volume fluctuations through the Quaternary (Berggren, 1972). Also today, the average temperature increase in the Arctic region is twice as fast as the global average (Cohen et al., 2014). The Arctic is thus an important contributor to climate forcing mechanisms, in particular due to albedo effects caused by snow and ice cover, and greenhouse gas storage in permafrost grounds (Schuur et al., 2008). Furthermore, deep water generated in the high northern latitudes is a significant driver of thermohaline circulation, which distributes heat and moisture around the globe (Broecker, 1991). Through the past decades, the future of the polar ice sheets and global climate has been a topic of intense debate, as observations of melting ice sheets on Antarctica and Greenland, along with diminishing sea ice cover in the Arctic, has raised worries with regards to rising sea level and global warming (e.g. Huybrechts et al., 2004, Zachos et al., 2008). Only through the understanding of the ocean-atmosphere-cryosphere interactions found in the geologic record, can predictions be made with regards to climate evolution of the future.

The timing of the onset and the subsequent evolution of glaciation in the Northern Hemisphere is still an open question (Thiede et al., 2011). Since most terrestrial evidence for pre-Quaternary paleoclimates have been erased during the last glacial cycle, we have to utilize marine sediment records for indicators of past climate. The International Ocean Discovery Program (IODP) and its precursor, the Ocean Drilling Program (ODP), is an international scientific drilling program set out to study the Earth's long-term history from sediments found the world's deep ocean basins. Through the IODP and ODP expeditions, traces of pre-Quaternary glaciations has been uncovered, amongst them evidence suggesting glaciers existed in the Northern Hemisphere already long before the global climate transition into the "Icehouse" world (e.g. Eldrett et al., 2007).

The Miocene Epoch (23.03–5.33 Ma) is a time of significant changes when the global climate transitioned from relatively warm and humid conditions with low seasonality, into the bipolar glaciated world with pronounced seasonality found today (Flower and Kennett, 1994, Bruch et al., 2006). In the Norwegian-Greenland Sea, the onset modern circulation and deep water formation is indicated in the early Late Miocene (Henrich et al., 1989), and several reports of ice rafted debris (IRD) suggest the presence Northern Hemisphere continental based glaciers and sea ice (Fronval and Jansen, 1996, Helland and Holmes, 1997, Winkler et al., 2002, St John, 2008). Sedimentological and geochemical methods were used to study a high-resolution sedimentary record from ODP Site 907. This thesis will focus on the paleoenvironmental evolution in the Iceland Sea over a 1 million-year time span in the in the Late Miocene.

1.1 Objectives

The overall objectives of this thesis focus on paleoclimate reconstruction in the Iceland Sea during the Late Miocene. The high-resolution sedimentological study carried out in the framework of this thesis may provide valuable insights into the paleoenvironmental variability in the Iceland Sea during the Late Miocene and may improve knowledge of the on Northern Hemisphere climate evolution during this time (e.g. Thiede and Myhre, 1996, Thiede et al., 1998). Global paleoclimate reconstruction indicate cooling events in the Miocene, known as Miocene events commonly related to ice volume growth on Antarctica and bottom water cooling (Miller et al., 1991). Miocene-event 6 (Mi-6, 10.7–10.4 Ma) has been described from Southern Hemisphere records (e.g. Wright and Miller, 1988, Miller et al., 1991, Westerhold et al., 2005) and thought to reflect increase in global ice volume (Turco et al., 2001). Few records from the Northern Hemisphere have been able to relate their findings to the Mi-6 event, hence the Mi-6 ice volume increase is primarily attributed to growth of the Antarctic ice sheet (Miller et al., 1991). Miocene IRD is reported from a few sites at high northern latitude prior to the Mi-6 event (e.g. ODP Site 642, Fronval and Jansen, 1996; ODP Site 909, Winkler et al., 2002; ODP Site 918, Helland and Holmes, 1997; IODP Site 302, St.John et al., 2008). However IRD from the Iceland Sea ODP Site 907 has only been investigated back to 8 Ma (Fronval and Jansen, 1996), while no sedimentological evidence for ice rafting is available to date.

Q: Is there evidence for older IRD, in particular, from the Mi-6 event, in sediments from the Iceland Plateau?

Terrigenous grains larger than > 125 μm deposited in hemipelagic setting are transported by icebergs or sea ice (e.g. Jansen and Sjøholm, 1991, Fronval and Jansen, 1996). The possible

presence of IRD contemporaneous with the Mi-6 event may reflect the existence of small-scale glaciers on continents surrounding the Norwegian-Greenland Sea, or possibly sea ice transported from the Arctic Ocean. Distinguishing between iceberg and sea ice rafted debris is important as both affect climate differently. Sea ice affects the ocean-atmosphere interaction (DeConto et al., 2007), while ice based on the continents influences sea level and consequently ocean acidity (Merico et al., 2008). Several IRD studies have analysed the surface textures of sand-sized quartz grains using Scanning Electron Microscope (SEM), in order to distinguish between iceberg and sea ice rafter debris (e.g. St John, 2008, Stickley et al., 2009).

Q: Can SEM analysis of quartz grain shape and texture help differentiate the transport mode for IRD at the study site?

Sedimentological evidence for the presence and variability of ice rafting in the Late Miocene Iceland Sea will extend the IRD record from Site 907 beyond 8 Ma. If iceberg transport is indicated, this will provide further insights into the long-term development of glaciations in the circum-Arctic regions and may help to understand the response of the high northern latitude to the global Miocene climate cooling trend. Understanding the boundary conditions for Northern Hemisphere glaciations is an important issue not only for scientific reasons, but is also of significant value for society— as the future of the Northern Hemisphere cryosphere may have great regional and global political and socio-economic consequences.

1.2 Background

1.2.1 Study Area

ODP Site 907 is located on the Icelandic Plateau, an area defined by the 1800-m contour, which is geographically situated between Iceland and Jan Mayen (Fig.1). The following sections will describe the study area in regards to present day ocean circulation, general physiography, tectonic development, as well as, the Miocene paleoenvironmental evolution.

1.2.2 Present-day Ocean Circulation in the Norwegian-Greenland Sea

The Norwegian-Greenland Sea (NGS), also known as the Nordic Seas, is in the northernmost part of the Atlantic Ocean. In the literature it usually refers to the combination of the Norwegian, Greenland and Iceland Sea (Blindheim and Østerhus, 2005). The ocean circulation in the NGS (Fig.1) is greatly controlled by its sea-floor bathymetry (Figure 3). The main bathymetrical features of the Norwegian Sea are the Norwegian Basin, Lofoten Basin and Vøring Plateau, while

the Greenland Sea comprises the Greenland and Boreas Basin. The Iceland Plateau is located between Iceland and Jan Mayen (Hansen and Østerhus, 2000). The NGS is separated from the rest of the Atlantic Ocean by the Greenland-Scotland Ridge (GSR), and from the Arctic Ocean by the Fram Strait. The GSR forms the southern gateway for water exchange — where warm and saline water from the Atlantic is channeled into the NGS, and dense bottom water exists into the Atlantic Ocean. The Fram Strait forms the northern gateway, where cold and fresh water from the Arctic Ocean enters the NGS. These two ocean gateways have strong control on the circulation in and out of the NGS, as they affect the rate of water exchange with the world's ocean basins, thus the NGS is an important contributor to the global ocean circulation (Blindheim and Østerhus, 2005).

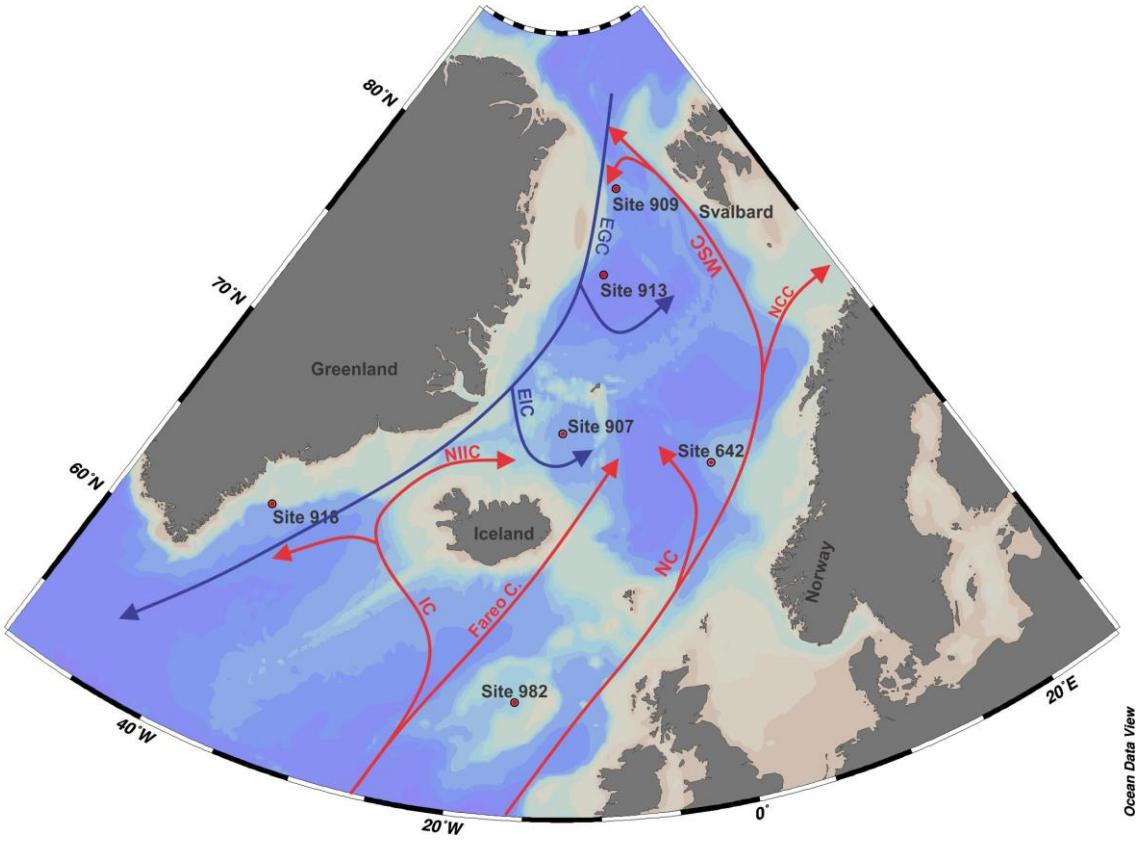

Figure 1: Map of the Norwegian-Greenland Sea and surrounding landmasses. ODP Site 907 is located on the Iceland Plateau between Iceland and Jan Mayen. Also shown are the present day surface currents in the Norwegian-Greenland Sea. Red arrows indicate warm surface waters originating from the Atlantic Ocean: IC= Irminger Current, NIIC: North Icelandic Irminger Current, NC= Norwegian Current, NCC=North Cape Current, WSC= West Spitsbergen Current. Blue arrows refer to cold surface water originating from the Arctic Ocean: EGC= East Greenland Current, EIC= East Icelandic Current (Redrawn from Hansen and Østerhus, 2000, Blindheim and Østerhus, 2005).

The North Atlantic Current enters the NGS in three branches across the GSR. The western most branch is the Irminger current, flowing around the west coast of Iceland towards the Denmark Strait. Warm water of the Irminger current bifurcates west of Iceland and a portion carries on along the north coast of Iceland as the North Icelandic Irminger Current (NIIC). As NIIC flows

north, it mixes with the cold and fresh water Arctic waters of the southwards flowing East Greenland Current. The mixing of Arctic and Atlantic water in the Icelandic Sea forms Modified East Icelandic Water, which has a winter temperature of 2 to 3°C, and salinities ranging from 34.85 to 34.90 psu (Hansen and Østerhus, 2000).

The Faroe current is the second branch of the North Atlantic Current entering the NGS across the GSR. The current transports Modified North Atlantic Water (mean annual temp. range 7–8.5 °C, salinity 35.10 to 35.30 psu, Hansen and Østerhus, 2000) through the Iceland-Faroe Channel. Some of the water mixes with water in the Faroe-Shetland Channel, while most of the water continues into the Norwegian Basin (Hansen and Østerhus, 2000). At Jan Mayen, some of the Faroe Current water enters the Iceland Sea, but most continues north of Jan Mayen where it meets water from the East Greenland Current (EGC).

The third branch of the Atlantic water inflow crosses the Faroe-Shetland Channel and becomes the Norwegian Current (NC). This is the warmest (mean annual temp. 9–10.5°C) and most saline (35.3–35.45 psu) of the three Atlantic branches (Hansen and Østerhus, 2000). The NC continues as a slope current along the Norwegian continental shelf break. At the Bear Island Through, the current divides and a substantial part enters the Barents Sea as the North Cape Current (NCC). The rest continues as the West Spitsbergen Current (WSC) towards the Fram Strait. At the Fram Strait some of the water enters the Arctic Ocean, but most of it is deflected south and is recirculated with the south flowing EGC (Rudels et al., 2002).

As mentioned previously, cold and Arctic Ocean waters enters the NGS through the Fram Strait as the EGC. The EGC continues south along the eastern margin of Greenland and transports Polar surface water— including sea ice, as well as Arctic Ocean intermediate- and deep waters (Hansen and Østerhus, 2000). The Greenland Fracture zone acts as a topographic barrier, redirecting some of the EGC waters into the Boreas Basin. Continuing south, some of the EGC waters are deflected at the Jan Mayen Fracture zone, subsequently forming the southern limb of the counter clockwise Greenland Basin cyclonic gyre (Hansen and Østerhus, 2000). The remaining waters of the EGC continues south, where a part of the current branches off to the east as the East Icelandic Current, forming the southern limb of the Iceland Sea gyre (Blindheim and Østerhus, 2005). The remaining water of the EGC exist the NGS through the Denmark Strait.

The main configuration of surface circulation with warm surface water flowing north and cold surface water flowing south leads to the establishment of a strong temperature salinity gradient

across the NGS, subdividing the area into a temperate Atlantic domain off Norway and a cold Arctic domain off Greenland (Hansen and Østerhus, 2000).

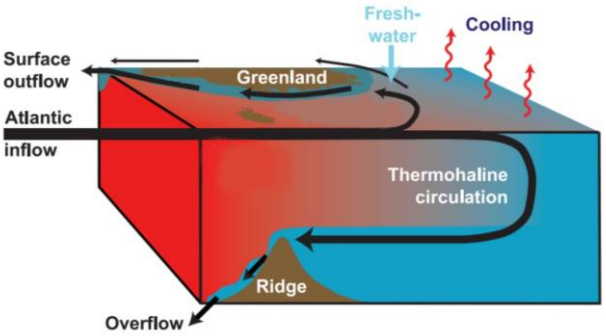

Figure 2: The thermohaline circulation in the Norwegian-Greenland Sea (modified from Hansen et al., 2008).

On its way through in the NGS, Atlantic water loses heat and becomes progressively denser (Figure 2). Subsequent convection and sinking of denser Atlantic surface water, and thus formation of deep water, occurs mainly in the gyres of the Greenland and Iceland Seas (Rudels et al., 2005). The newly formed deep water mixes with Arctic water carried by the EGC, and is finally exported out of the NGS as dense overflow water through the deeper sills of the GSR (Hansen and Østerhus, 2000). The dense overflow waters sink after crossing the GSR, and joins Labrador Sea deep water to form North Atlantic Deep Water (NADW), replenishing the deep waters in the North Atlantic. As water exits the NGS, a lateral pressure gradient from the Atlantic and Arctic Ocean draws more water into the NGS. This convective circulation of surface waters in to the NGS and export of deep water to the North Atlantic Ocean is known as Atlantic Meridional Overturning (AMOC)(Bradley, 1999). The water mass exchange through the Fram Strait and across the GSR controlling the circulation system in the NGS, thus affecting AMOC and the supply of NADW to the world's deep ocean basins. The NGS circulation is therefore an important contributor to global thermohaline circulation, which in turn affects global climate by moving water masses, distributing heat and moisture to the atmosphere and surrounding continents (Rahmstorf, 2002). Through geologic time, the circulation in the NGS and variations of AMOC have ultimately affected Earth's climate history (e.g. Broecker, 1991, Flower and Kennett, 1994, Wright and Miller, 1996).

1.2.3 Plate Tectonic Evolution of the Norwegian-Greenland Sea

Present day ocean circulation in the Nordic Seas is strongly controlled by its bathymetry, which in turn reflects the plate tectonic history of the area (Perry, 1986). Today the bathymetry of the

Norwegian-Greenland Sea is divided into sections between the Greenland-Scotland Ridge, and the Jan Mayen, Greenland-Senja and Spitsbergen fracture zones (Fig.3) (Thiede et al., 1998).

The Greenland-Scotland Ridge forms the southern bathymetric boundary of the Norwegian-Greenland Sea. The Kolbeinsey Ridge stretches from the Greenland-Scotland Ridge north towards the Jan Mayen Fracture Zone. The Iceland Plateau is located east of the Kolbeinsey ridge, and is a thicker part of the oceanic crust likely due to the underlying Icelandic plume (Kodaira et al., 1998). The Jan Mayen Fracture Zone forms the northern border of the Iceland Plateau, where the mid ocean ridge shifts westwards, and subsequently continues north as the Mohns Ridge. The Mohns Ridge separates the Lofoten and Greenland basins, and terminates to the north where it meets the Greenland-Senja Fracture Zone. The Greenland Senja Fracture Zone separates the Greenland and Boreas Basins. The Knipovich Ridge forms the Eastern boundary of the Boreas Basin, and stretches up to the Svalbard fracture zone and the Fram Strait. The Kolbeinsey, Mohns, and Knipovich ridges are active spreading ridges, with a present day spreading rate around 20 mm/yr or less, thus they are regarded as slow-spreading ridges (Kodaira et al., 1998).

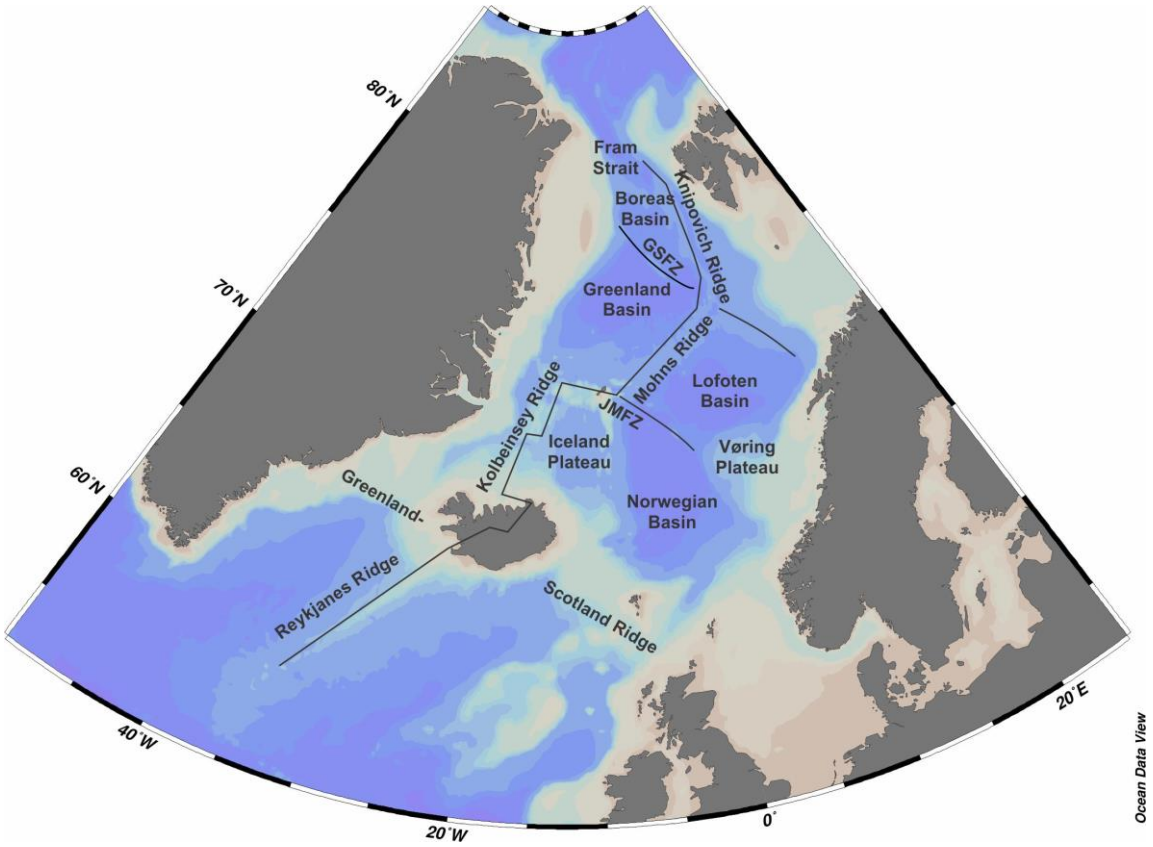

Figure 3: Map illustrating the fundamental bathymetrical features of the Norwegian-Greenland Sea and its main tectonic elements (redrawn from Thiede and Myhre, 1996).

A prolonged history of alternating extension and basin formation since the post-Caledonian orogenic collapse in the Devonian led to beginning of passive margin development in the Early Eocene, and resulted in the widening and deepening of the North Atlantic (Faleide et al., 2008). The tectonic evolution of the Norwegian-Greenland Sea can be separated into pre-break up basin formation, initial spreading at the Mesozoic-Cenozoic transition, and an Early Oligocene shift in rifting direction leading to the development of a deep water passageway to the Arctic Ocean.

At the Late Jurassic-Early Cretaceous boundary, various rift episodes resulted in the development of the Møre and Vøring basins. Basin formation also occurred off East Greenland and in the SW Barents Sea at the time. An epicontinental sea with thinned crust existed between Greenland and NW Europe prior to opening and margin formation. Rifting and seafloor spreading initially occurred along the regional De Geer Zone megashear system in the Late Cretaceaous-Paleocene, linking the Nordic Seas spreading to the Arctic basin and the Vøring, Møre and Greenland margins developed during this time (Faleide et al., 2008). Subsequently, active spreading occurred in the Labrador Sea and Greenland drifted in a NW direction with respect to the Eurasian continent until the end of the Eocene. By that time, the Norway and Lofoten basins, and the southern part of the Greenland basin were established and a narrow oceanic basin existed along the southern margin of Svalbard. When seafloor spreading in the Labrador Sea ceased in the earliest Oligocene, the relative motion of the Eurasia and Greenland plates shifted from transform to divergent (Engen et al., 2008). The new direction of motion led to rifting along the northern Hornsund fault zone and opening of the Fram Strait (Fig.4). The Fram Strait constitutes the only deep water connection between the Arctic Ocean and the North Atlantic and thus exerts major influence on ocean circulation (for details see Chapter 1.2.2). Despite its importance, the exact timing of its opening is still under debate, but the gateway had probably reached sufficient depth for deep water exchange by the early Middle Miocene (Jakobsson et al., 2007).

The Greenland-Scotland Ridge forms the southern gateway for water mass exchange passage between the Norwegian-Greenland Sea and the Atlantic Ocean, and has developed as a trail of the south-westward migrating Icelandic plume (Hanan and Schilling, 1997). Variations in mantle plume activity throughout the Neogene have controlled the sill-depth of the Greenland-Scotland Ridge, thus modulated water mass exchange across the ridge and therefore influenced ocean circulation in both, the Norwegian-Greenland Sea and the North Atlantic (Wright and Miller, 1996). Water is channelled across three main conduits of the GSR, namely the Denmark Strait (~620 m), Faroe-Iceland Channel (~500 m), and Faroe-Shetland Channel (~800–900 m)(Wright and Miller, 1996). Oceanic crust in the Denmark Strait is dated to 55 Ma, but it did not act as a

barrier for deep water connection found between Greenland and Iceland before around 18-14 Ma (Kodaira et al., 1998), while, a deep water passageway probably already existed in the Faroe-Shetland Channel east of the Faroe Island (Thiede et al., 1998).

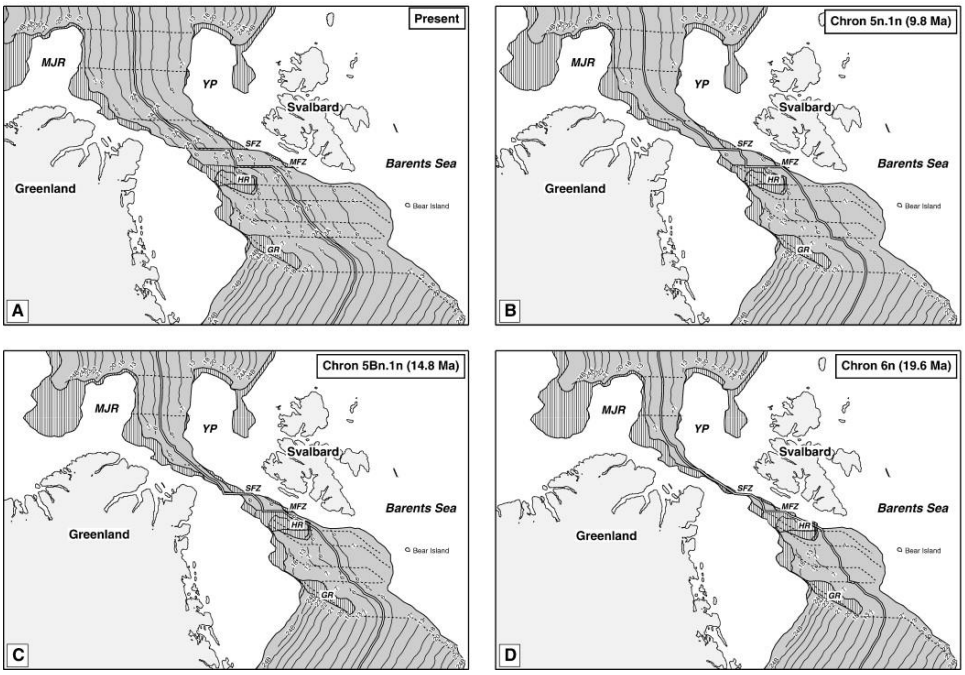

Figure 4: The plate tectonic evolution of the Fram Strait (from Engen et al., 2008). Magnetic anomalies are lines and oceanic crust is shaded. ***A****. Present day Fram Strait* ***B****. The first well developed magnetic anomalies in the Fram Strait, ~10 Ma.* ***C****. Initial formation of a narrow oceanic corridor, ~20–15 Ma.* ***D****. Closure between NE Greenland and Svalbard, ~20 Ma.*

1.2.4 Miocene Paleoenvironmental Evolution

1.2.4.1 Global Miocene paleoenvironmental evolution - *a short review*

The earliest Cenozoic glaciers probably developed on East Antarctica in the Late Eocene (~45 Ma), and likely persisted for most of the Oligocene until 26–27 Ma. After which, a general warming trend, interrupted by only temporary cooling events, controlled repeated build-up and melting of ice on the Antarctic continent (Zachos et al., 2001). Cenozoic climate variations are commonly reconstructed from deep-sea oxygen ($\delta^{18}O$) and carbon isotopes ($\delta^{13}C$) measured on calcite shells of marine organisms (e.g. foraminifera). Where heavier $\delta^{18}O$ are interpreted to represent bottom water cooling and/or continental ice volume increase, and $\delta^{13}C$ is used to reconstruct global carbon cycle changes and to trace deep water sources (Miller et al., 1991, Wright et al., 1992).

Developments in constructing astronomically-tuned chronologies for deep-sea sedimentary records has enabled precise dating of climatic events, and helped to decipher the causal

relationships between causes and consequences of global climate change (Zachos et al., 2001, Westerhold et al., 2005). Global $\delta^{18}O$-records exhibits a gradual trend towards heavier values throughout the Cenozoic, thus reflecting the global cooling trend. After the Oligocene-Miocene transition and a subsequent initial Miocene cooling, a brief warm period, known as the Miocene Climate Optimum (MCO, 17–14.5 Ma) commenced. This interval regarded as the globally warmest since the Middle Eocene (Zachos et al., 2008).

Global climate started to deteriorate towards the end of the MCO, leading into the Middle Miocene Climate Transition (MMTC, 14.2 –13.7 Ma, Fig.5) (Flower and Kennett, 1994, Shevenell et al., 2004). Several $\delta^{18}O$-increases are observed in the global stacked oxygen isotope record of the Miocene. These short-term cooling events are referred to as Miocene isotope events (Mi-events sensu Miller et al., 1991) and have been related to low amplitude variations in the 1.2 Myr obliquity cycle (Lourens and Hilgen, 1997). A two-step cooling (at 14.2 and 13.8 Ma) characterizes the MMCT, and since then, global $\delta^{18}O$-values have never returned to pre-event values (Zachos et al., 2001). Stepwise expansion of local ice caps in the Middle Miocene led to glaciation of the entire Antarctic continent (Anderson, 1999), while IRD records from the MMCT reflect extensive growth of the East Antarctic Ice Sheet (Flower and Kennett, 1994). In addition, cooling is inferred from turnovers in terrestrial and marine biota, and evidenced by aridification at mid-latitudes and in the Northern Hemisphere (Flower and Kennett, 1994). The mechanisms behind the MMCT may include uplift of continents and related CO_2 drawdown (Raymo, 1994), as well as opening and closing of oceanic gateways, e.g. closing of the Eastern Tethys passageway to the Mediterranean (Shevenell et al., 2004). Which according to a modelling study by Butzin et al. (2011) ultimately altered the global ocean circulation.

Subsequent to the MMCT, global climate is characterized by a general long-term cooling trend punctuated by two increases in the $\delta^{18}O$- record, the Mi-5 (11.8–11.4 Ma) and Mi-6 (10.7–10.4 Ma) events (e.g. Turco et al., 2001, Abels et al., 2005, Westerhold et al., 2005). Both events are associated with extensive growth of the East Antarctic Ice Sheet and sea level drop. The Mi-6 event, for example, is suggested to equal a ~50 m global sea level drop attributed to ice volume increase (John et al., 2004, Westerhold et al., 2005). Throughout the Late Miocene, mean global $\delta^{18}O$ continues to shift towards heavier values, indicating further cooling and ice growth on East Antarctica but also on West Antarctica and potentially the Arctic (Zachos et al., 2001).

The Pliocene Epoch (5.33–2.58 Ma) is characterized by warmer-than-present day average global temperatures (up to ~3°C, Seki et al., 2010) with similar to present day atmospheric CO_2 concentrations (~330–400 ppm, Seki et al., 2010). At around 3.3 Ma global ocean circulation

changes, along with declining atmospheric CO_2 concentrations, led to significant cooling which gradually intensified glaciations in the circum-Arctic regions, in the Northern Hemisphere as well as on the Antarctic continent (De Schepper et al., 2014). While the general Cenozoic history of Antarctic glaciations are comparatively well understood (e.g. Zachos et al., 2001), the timing of the onset of Neogene glaciation in the Northern Hemisphere is rather poorly constrained (e.g. Thiede et al., 2011).

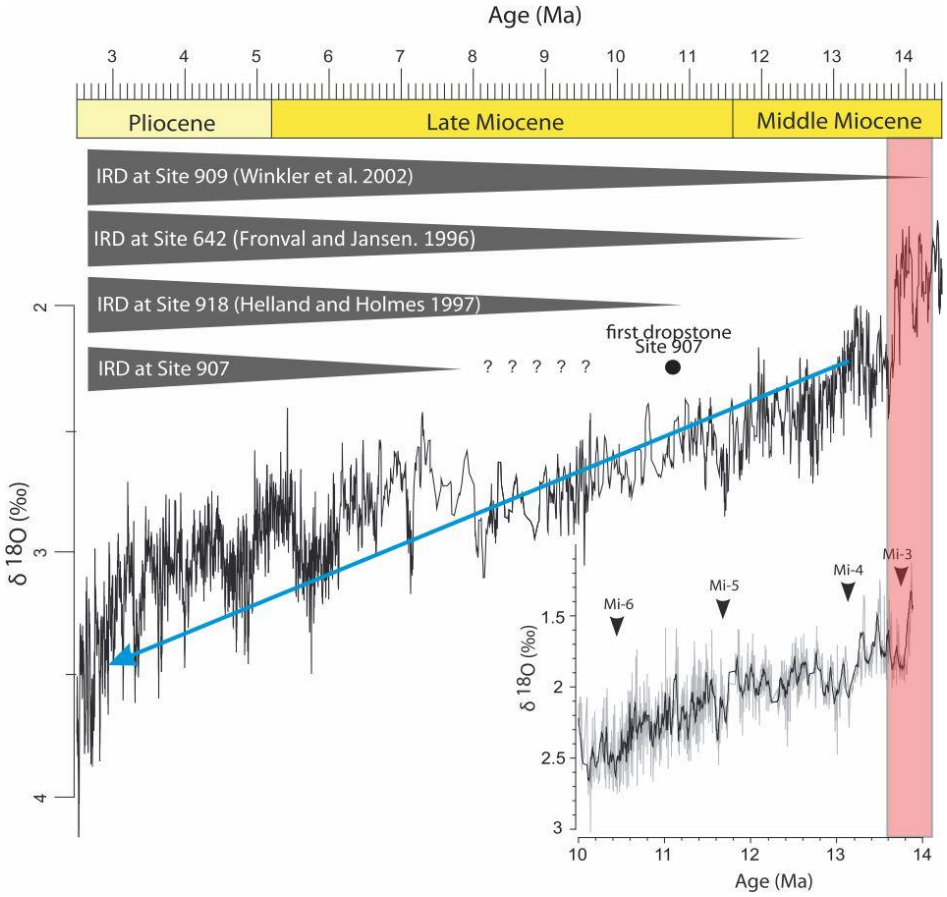

Figure 5: Global oxygen isotope record of Zachos et al. (2001) illustrating climate evolution in parts of the Miocene and Pliocene. Red shaded area highlights the Middle Miocene Climate Transition (MMCT, Flower and Kennett, 1994). The blue arrow indicates the general long-term cooling trend after the MMCT towards the Pliocene. Also indicated is the occurrence of IRD at ODP Site 909 in the Fram Strait (Winkler et al., 2002), ODP Site 642 on the Vøring Plateau (Fronval and Jansen, 1996), ODP Site 918 in the Irminger Basin (Helland and Holmes, 1997), and ODP Site 907 in the Iceland Sea (Fronval and Jansen, 1996). The first dropstone at Site 907 is observed at ~10.4 Ma (Shipboard Scientific Party, 1995). Smaller insert illustrates the $\delta^{18}O$ record from ODP Site 1085 and the timing of the Mi-events, as proposed by Westerhold et al. (2005).(Figure is courtesy of M. Schreck, modified for this thesis).

1.2.4.2 Norwegian-Greenland Sea Miocene Paleoenvironmental Evolution

Discoveries of IRD in sediments of up to Middle Eocene age suggests that Arctic ice has formed several times during the Cenozoic (e.g. Eldrett et al., 2007, St John, 2008). Sea ice probably formed seasonally in the central Arctic Ocean around ~47 Ma (Stickley et al., 2009), supporting a Middle

Eocene cooling phase (Zachos et al., 2001). Also, Eocene continental ice on Greenland is suggested by glacially abraded dropstones at ODP Site 913 in the Greenland Sea ~38 Ma (Eldrett et al., 2007).

The oldest (potential) Miocene IRD is reported from the Fram Strait at around 17 Ma (Thiede et al., 1998), although ice rafting in the Norwegian-Greenland Sea may have not intensified until after the MMCT (Fig.5) (Thiede et al., 1998). Prior to the MMCT, a zonal circulation pattern with poorly ventilated and stratified water masses likely characterized the Norwegian-Greenland Sea (Henrich et al., 1989, Thiede and Myhre, 1996), and warm and nutrient-rich water persisted as indicated by predominantly siliceous microfossil assemblages (e.g radiolaria, diatoms, and sponge spicules) and agglutinated foraminifera (Henrich et al., 1989).

A generally weaker circulation is indicated in the sedimentary record by well laminated sediments (Henrich et al., 1989). The modern-type circulation, characterized by an cold East Greenland Current influencing the western margin of NGS, and relatively warm Atlantic water along the eastern margin was not established, and thus, NADW formation and deep water overflow across the GSR was likely not significant (Bohrmann et al., 1990, Poore et al., 2006).

Sedimentary records from the Norwegian-Greenland Sea reveal intensified IRD input after the MMCT (e.g. Wolf-Welling et al., 1996, Fronval and Jansen, 1996). IRD pulses are observed in the Fram Strait at 14 Ma (Wolf-Welling et al., 1996), and at the Vøring Plateau starting from 12.6 Ma (Fronval and Jansen, 1996). An early Barents Sea Ice Sheet has been suggested as a source for Middle Miocene IRD in the Fram Strait (Knies and Gaina, 2008). A heavy mineral clay provenance study suggests perennial ice cover existed in the Arctic Ocean since about 13 Ma (Krylov et al., 2008). The reported IRD pulses occur contemporaneous to major shifts in NGS circulation (Thiede and Myhre, 1996). The Fram Strait had significantly deepened since the initial opening ~17 Ma, reaching modern day water depths (>2000 m) by the end of the MMCT (Jakobsson et al., 2007). Shoaling of the Central American Seaway led to strengthening of the North Atlantic Drift and, subsequently, a stronger east-west temperature salinity gradient was established within the NGS (Nisancioglu et al., 2003). Furthermore, convection and deep water formation increased and proto-NADW initially formed around 13.6 Ma (Henrich et al., 1989). Benthic foraminiferal $\delta^{18}O$-values from the Vøring Plateau Site 642 further suggests bottom water cooling and increased ventilation around this time (Fronval and Jansen, 1996). Uplift and subsidence of the Greenland-Scotland Ridge has controlled the exchange of both surface and deep waters, as revealed by the inverse relationship between increased amounts of proto-NADW in deep ocean basins and periods of deepening of the GSR (Wright and Miller, 1996, Poore et al., 2006). Large quantities of deep water overflow across the Greenland-Scotland ridge occurred episodically at least since ~12

Ma (Poore et al., 2006), while calcareous nannofossil assemblages at ODP Site 918 suggests initiation of a proto-East Greenland Current at about 12 Ma (Wei, 1998). Intensified circulation after the MMCT is also indicated by widespread erosion and hiatuses observed in the Middle Miocene sedimentary records (Henrich et al., 1989). Altered circulation pattern is also reflected in periodic changes from predominantly biogenic siliceous sediments to biogenic carbonate deposition in the Middle Miocene (Bohrmann et al., 1990). Increased carbonate deposition/preservation in the NGS has been interpreted as increased influence of Atlantic water, and thus enhanced overturning (Bohrmann et al., 1990, Fronval and Jansen, 1996).

Further intensification of ocean circulation is indicated by a noticeable shift of sediment source region and increased bulk accumulation rates in the Fram Strait ODP Site 909 at ~11 Ma (Winkler et al., 2002). In addition, IRD records from ODP Site 918 in the Irminger Basin suggests iceberg rafting from southeast Greenland at the same time (~11 Ma, Helland and Holmes, 1997). The IRD is interpreted to reflect small-scale glaciation on Greenland, somewhat contemporaneous with suggested Middle Miocene onset of a cold proto EGC (Wei, 1998).

In the Late Miocene, clay mineral assemblages in the Fram Strait indicate gradual cooling culminating in increased IRD input at ~9 Ma (Winkler et al., 2002), which coincides with the Late Miocene cooling between 10.8 to 8.6 Ma as already suggested by Wolf-Welling et al. (1996). At the Vøring Plateau, IRD is observed from ~12.6 Ma to ~9.5 Ma; however, two intervals from ~9.5–9 Ma and 8–7 Ma are barren of IRD (Fronval and Jansen, 1996). Strong ice rafting signals are observed across the entire Norwegian-Greenland Sea roughly around 7 Ma (Wolf-Welling et al., 1996, Fronval and Jansen, 1996, Thiede et al., 2011), and also further south at ODP Site 918 in the Irminger Basin (St.John and Krissek, 2002). In addition, benthic foraminiferal $\delta^{18}O$-values on the Vøring Plateau increase significantly around 7 Ma, supporting enhanced glaciation in the Northern Hemisphere at that time (Fronval and Jansen, 1996). Towards the end of the Late Miocene, further cooling is indicated from increased ice rafting between 6.3–5.5 Ma at Site 909 (Wolf-Welling et al., 1996). Cooling in the latest Miocene has also been suggested by an alkenone sea surface temperature record (Herbert et al., 2016) and dinoflagellate cyst assemblages (Schreck et al., 2013) from ODP Site 907 in the Iceland Sea. While ice rafting is reported from ODP Site 907 in the Iceland Sea until 8 Ma (Fronval and Jansen, 1996), no sedimentological studies have described the sediments from this site further back than ~8 Ma.

Ice rafting ultimately intensified in the Pliocene. Continuous ice rafting is reported in the Norwegian Sea starting at 6 Ma (Jansen and Sjøholm, 1991). Continuous IRD is also reported as from the Iceland Sea starting at ~3.6 Ma, with a major peak at 3.3 Ma (Jansen et al., 2000, Kleiven

et al., 2002). In contrast, the first North Atlantic IRD pulse is observed around 3.3 Ma (Kleiven et al., 2002). The timing and distribution of IRD observed in Pliocene record from the North Atlantic and the Norwegian-Greenland Sea is interpreted to indicate an earlier response of the Greenland ice sheet to regional cooling compared to the Scandinavian ice sheet (Kleiven et al., 2002).

Despite evidence for episodic glaciations on continents surrounding the Norwegian-Greenland Sea following the MMCT (e.g. Thiede et al., 2011), unequivocal correlation to the globally observed Miocene cooling events is still missing. Changing clay mineral assemblages at Fram Strait ODP Site 909 indicate cooling which may have occurred contemporaneous with the Mi-6 and Mi-7 events (Winkler et al., 2002). Schreck et al. (2013) observed changes in marine palynomorph assemblage composition in the Iceland Sea, which may correspond to the Mi-3 to Mi-7 events. Interestingly, a dinoflagellate cyst disappearance event at ODP Site 907 correlates well with the proposed timing of the Mi-6 event (Schreck et al., 2013). At Site 907, however, IRD has not been analyzed beyond ~8 Ma (Fig.5) (Fronval and Jansen, 1996). This results in a gap in understanding of the development of Miocene glaciations in the Norwegian-Greenland Sea and their possible relationship to the Mi events. This highlights the importance of the main objective of this thesis.

2 Material and Methods

This paleoclimate study is based on investigation of sediments collected in 1993 aboard research vessel *JOIDES Resolution*, during the Ocean Drilling Program (ODP) Leg 151 at Site 907, Hole 907A.

2.1 Data collected by the Shipboard Scientific Party

2.1.1 Coring

The drilling at Site 907 took place from the 5th of august to the 8th of august, 1993. Hole 907A was drilled using an advanced hydraulic piston corer (APC). A relatively shallow and flat area was selected as coring site, providing access to an undisturbed sequence of hemipelagic sediments. Water depth to the seafloor at the chosen location was 2035.5 meters. The hole was drilled 216.3 meters below seafloor (mbsf), where it hit the basement consisting of basalt. Twenty-six cores were recovered at Hole 907A; total length of cored section was 224.1 meters. The two cores analysed within this thesis (13H and 14H) represent depths between 111.8–130.8 mbsf.

2.1.2 Lithology

Core descriptions were published in the Initial Cruise Report (Myhre et al., 1995), encompassing sedimentary logs and core pictures taken aboard the ship. The Shipboard Scientific Party (1995) described the lithology with regards to colour variations, dominant grain sizes, tephra layers, biogenic components, degree of bioturbation, and existing dropstones, and a total of five lithological units were distinguished. Cores 13H and 14H studied in this thesis are a part of lithological Unit III (from the lower part of subunit IIIB) but also include the upper ~10 meters of Unit IV (Fig.6).

Unit I accounts for the uppermost 17 meters of the hole and is of Quaternary age. Lithology consists of clayey silt, silty clay, including biogenic calcareous material, mostly foraminifera. There is little volcanic glass and few dropstones.

Unit II (~17-56 mbsf) consists of Pleistocene to Pliocene clayey silts and silty clays. The sediment bears abundant silt- and sand-sized siliciclastic grains. It lacks biogenic carbonate while volcanic glass is rare.

Unit III (~56-118 mbsf), Pliocene to Late Miocene in age, is described as clayey silts and silty clays, containing biogenic silica, increasing amounts of volcanic glass, but a decrease in quartz and feldspar. All layers (except ash layers) are gradational in contact, likely due to pervasive bioturbation. This unit is divided into two subunits, separated by the presence of nannofossil ooze

and nannofossil silty clay in subunit IIIA. The lowermost 7 meters of subunit IIIB are a part of core 13H, down to section 13-H6, 30cm. This interval is characterized by higher content of biosilica and an apparent lack of biogenic carbonates. Three dropstones are present in section 13H-4. A layer of ash- and biosilica-bearing clay is described from section 13H-5, 50cm through section 13H-6, 30cm. Moderate bioturbation occurs throughout core 13H.

Unit IV (~118-197 mbsf) is described as silty clays and clayey silt, biosilica-bearing with graded ash layers common in the upper part of the unit. The unit is of Middle to Late Miocene age and contains only little quartz and no dropstones. The speckled appearance of the sediment is a result of extensive bioturbation. The upper 13 meters of this unit are included in this study. They are characterized as biosilica-bearing silty clays, slightly bioturbated and containing ash layers.

Unit V (~197-216 mbsf) has a higher quartz and clay content, and a lower biogenic silica content compared to Unit IV. The major lithologies of Unit V are clayey mud and silty clay. There are no discrete ash layers but volcanic glass is common.

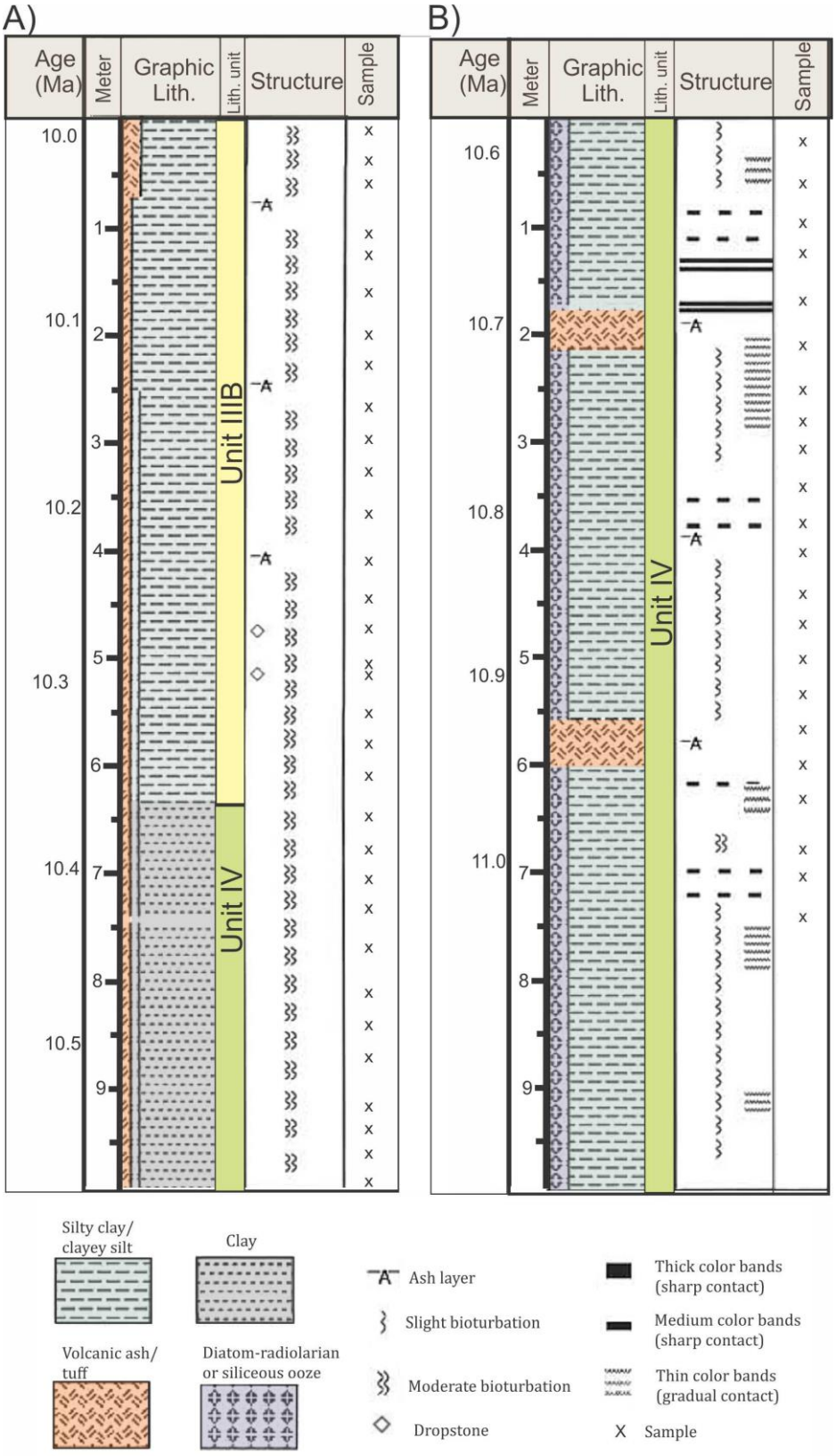

Figure 6: Lithological logs for cores 13H (A) and 14H (B) of ODP Hole 907A. Also shown is the position of samples used within this study. Lithological log modified from Shipboard Scientific Party (1995).

2.1.3 Age control

The age model for Site 907 is primarily based on magnetostratigraphic interpretation supported by biostratigraphic datums. Measurements of magnetic polarity was done onboard using a cryogenic pass-through magnetometer, while due to the lack of calcareous microfossils the biostratigraphic pin points are mainly based on diatoms and silicoflagellates supplemented by dinoflagellate cysts (Myhre et al., 1995). The initial shipboard age model has later been revised by Channell et al. (1999), based on the composite record of holes 907A, B, and C. Therefore, it represents the best age model for the Miocene to Pliocene interval in the entire Norwegian-Greenland Sea. For this thesis the ages of tie points have been updated to the latest geologic time scale (Gradstein et al., 2012, Hilgen et al., 2012).

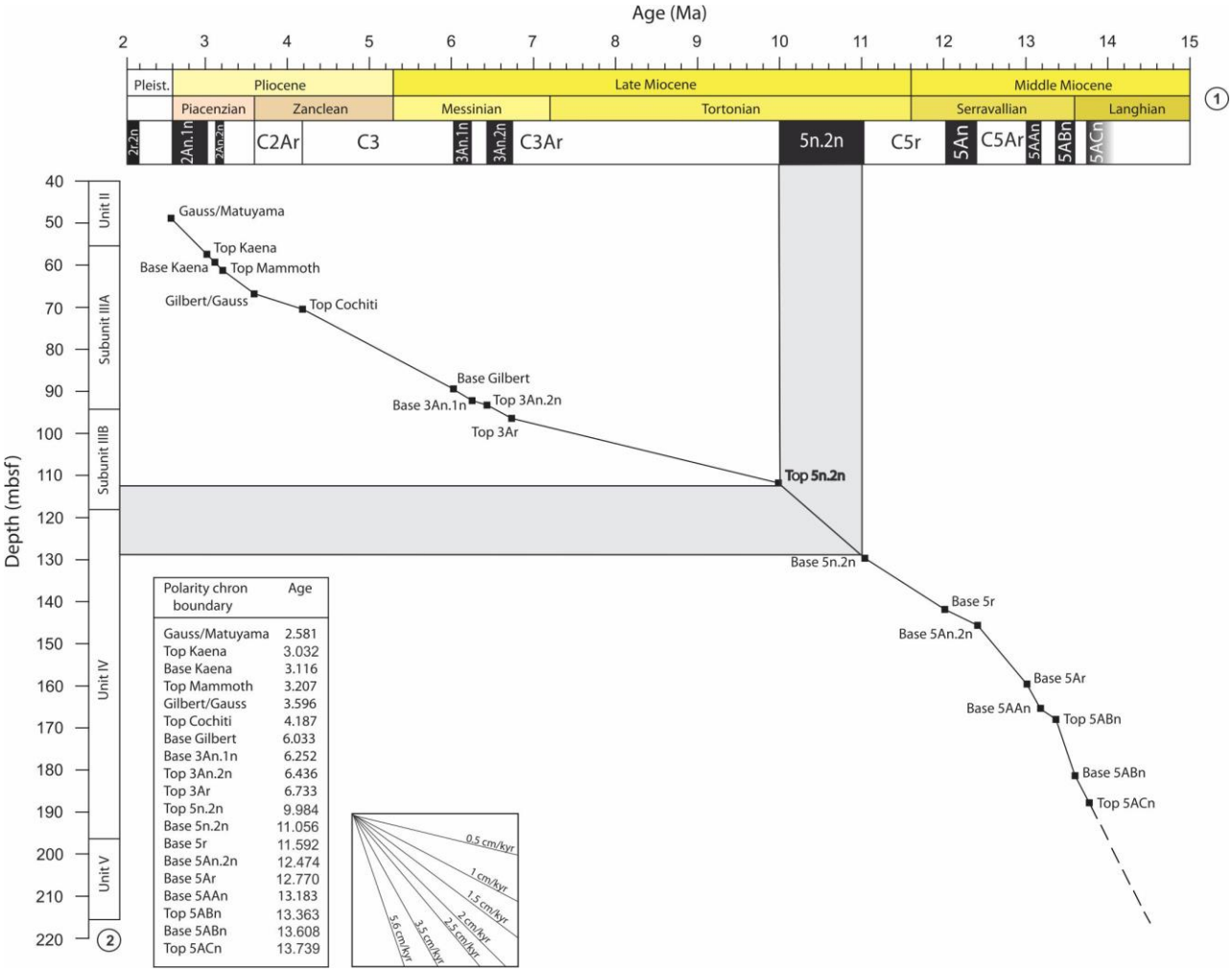

Figure 7: Age/depth plot for ODP Hole 907A using the age model of Channel et al. (1999). Highlighted in grey is the interval studied in this thesis, which is well-constrained by magnetostratigraphy. ***1.*** *Epochs and subepochs of the Neogene (Miocene, Pliocene) and Quaternary (Pleistocene).* ***2.*** *Lithological uits (Shipboard Scientific Party, 1995). The insert table shows the polarity chrohn boundaries and the smaller box the corresponding sedimentation rates (modified from Channell et al., 1999 and Schreck et al., 2012).*

The study interval (cores 13H and 14H) has a particularly well constrained age control with age markers positioned at the top of core 13H and at the bottom of core 14H. Tie points at depths of 111.80 and 129.70 mbsf assigns the top of core 13H a minimum age of 9.984 Ma, and the bottom of core 14H a maximum age of 11.056 Ma, respectively. This results in a linear sedimentation rate of ~1.67 cm/kyr across the studied interval. Absolute ages can therefore be assigned to individual samples (Figs. 6 and 7).

2.1.4 Sediment sampling

The cores are stored in the International Ocean Discovery Program (IODP) core repository at Marum in Bremen, Germany. Based on the age model of Channell et al. (1999), a total of 54 sediment samples were collected from Hole 907A-13H and 14H in the interval between 10-11 Ma. Sample spacing had to be adjusted according to sediment preservation but translates into temporal resolution of ~20 kyr. Samples (~20–30 grams each) were freeze dried and weighed, and subsequently split for analysis of marine palynomorphs (dinoflagellate cysts and acritarchs) and for the analytical procedures conducted within this study (see below), which ensures comparability of the different proxies used.

2.2 Laboratory work

All laboratory work described below was performed in the laboratory of the Department of Geosciences, The Arctic University of Norway in Tromsø, from August 2017 to February 2018. The steps included in the laboratory work are illustrated in Figure 8.

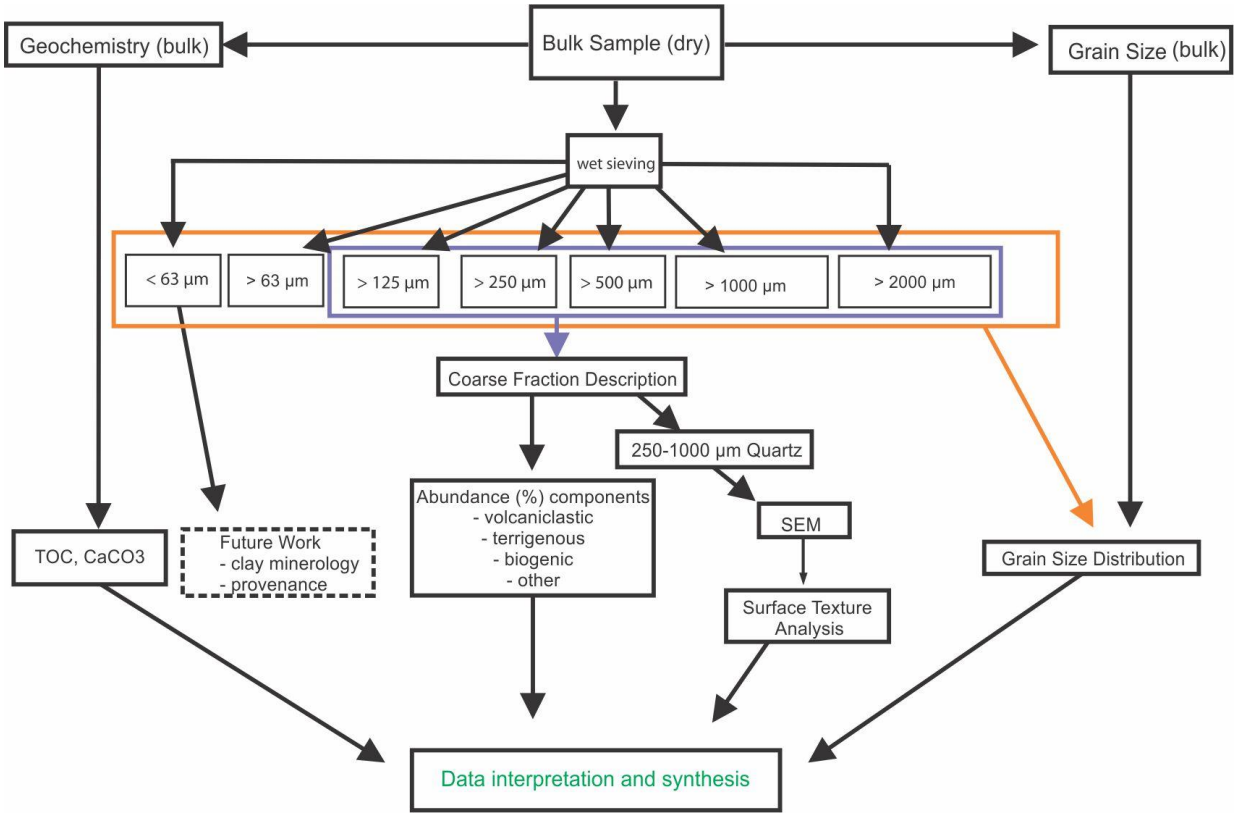

Figure 8: Flow chart illustrating the order of procedures during analysis of sediments from ODP Hole 907A.

2.2.1 Geochemical bulk parameters

Determination of bulk organic geochemistry allows a first characterization of the sedimentary environment. Fluctuation of organic carbon in marine sediments may indicate variation in marine paleo-productivity and/or influence from terrestrial organic matter. Therefore its concentration in the sediment may be used as a proxy for the controlling factors of productivity and terrestrial input to the ocean, such as nutrient availability and vertical mixing of water masses, or fresh water runoff from land (Meyers, 1997). The carbonate content in hemipelagic sediments may be an indicator for the provenance of sediments. However, with increasing distance from land and increasing water depth it is more likely an indicator for the content of calcareous microfossils (Milliman, 1993). Preservation of carbonate ($CaCO_3$) in the geologic record depends on the chemistry and temperature of the sea water, hence fluctuations of $CaCO_3$ may be used as a proxy

for pale-oceanographic conditions (Huber et al., 2000). Variations in the amount of carbon (inorganic and organic) is also a factor of the sedimentation rate (Meyers, 1997).

Determination of sedimentary total carbon (TC) and total organic carbon (TOC) was done by means of combustion analyses using LECO CS744. Which uses infrared absorption measures the amount of CO_2 and SO_2 during combustion in a sterile oxygenated environment. Approximately, 1 gram per sample was crushed in a grinder prior to further treatment and analyses. In order to compare the amount of TC to TOC the powdered samples were divided in two parts, around ~0.2 grams for TC and ~0.5 grams for TOC measurements respectively. Prior to measuring TC contents, the samples were put into non-porous crucibles. Each crucible was placed on a scale connected to the LECO CS744 and tared. Subsequently, the sediment was added and sample mass was automatically transferred into the data spreadsheet. One scoop of both Lecocel II and iron chip accelerator was added before transferring the crucible to the apparatus for analysis.

For the TOC analysis, sediment was put in a porous crucible and weighed prior to treatment with HCl in order to remove inorganic carbon. In order to prevent sample loss due to excessive fizzing, drops of 10% solution HCl were carefully added. The acid was left to drain through the sample, repeating the process three times or until samples stopped fizzing. After acid treatment the sediments were rinsed with distilled water 8 to 10 times. Samples were then dried in a drying cabinet set to 105°C for at least 12 hours, before the temperature was reduced to 40°C and samples were let to cool off. Dry samples were put into non-porous crucibles for combustion analysis in the same way as for TC analysis. The TOC content was calculated from sample mass recorded prior to inorganic carbon removal. $CaCO_3$ was determined from TC and TOC contents using the equation (Knies et al., 2003):

$$CaCO_3 = (TC\text{-}TOC)*8.33$$

Values of TC, TOC and $CaCO_3$ are reported as weight percentage (wt. %) and data are plotted in Grapher.

2.2.2 Particle size analysis using coulter counter

Particle size analyses was performed to study the grain size distribution throughout the cores. Characterizing the grain size distribution may yield valuable information on depositional processes and environments, possibly indicating events of increased sand input related to ice rafting (e.g. Wolf-Welling et al., 1996).

Particle size analyses was conducted using a Beckman Coulter LS 13320. Prior to analysis the carbonate and organic material was removed by adding HCl and H_2O_2. This was done to ensure measuring only the minerogenic portion of sediments, however, this treatment does not remove biogenic silica. A 20 % solution of HCl was added to each sample and left to work for 24 hours. After the acid treatment, sediments were rinsed with distilled water two times. Excess acid and water was decanted after centrifuging for 4 minutes at 4000 rpm between each rinsing cycle. A 20 % solution of H_2O_2 was added to each sample and left in an 80°C water bath for two hours. Following the same washing procedure as after the HCl-treatment, the samples were left to dry inside a fume hood. Approximately ~0.2 g was extracted from each sample, and 20 cl distilled water applied before they were shaken for 24 hours. To disintegrate aggregates, two drops of Calgon were added just before a 5-minute ultrasound bath, followed by analysis.

By using a light source and registering the scatter of light when hitting particles, the Beckman Coulter LS 13320 measures the size of each individual grain and gives its abundance value in weight %. Each sample was measured three times and the mean grain size values were calculated. The Wentworth size classification was used for sorting sediments (Table 1).

Table 1: Grain size classification used to describe grain sizes. After Wentworth (1922).

Size (µm)	**Name**
>2000	Granule
2000–1000	Very Coarse Sand
1000-500	Coarse Sand
500–250	Medium Sand
250-125	Fine Sand
125–63	Very Fine Sand
63–3.9	Silt
< 3.9	Clay

2.2.3 Wet sieving

Each sample was weighed before sieving. Sample weight ranged from ~7–21 g (average ~12 g). Mesh sizes used were 2 mm, 1 mm, 500 µm, 250 µm, 125 µm, and 63µm. Individual size fractions larger than 63 µm were collected in separate glass bowls. All sediment smaller than 63 µm were collected for possible future analysis of the fine fraction.

Twenty-one samples were sieved before discovering that a substantial amount of finer sediment was clumped in aggregates within the coarser fractions. In order to evaluate their nature, individual aggregates were picked and treated with hydrogen peroxide (H_2O_2) and hydrochloric acid (HCl), where H_2O_2 had the most prominent reaction and thus, could aid disintegration. The sediment was put in 100ml of water along with a 10ml of 20% solution H_2O_2. The mixture was shaken for 2–3 hours, followed by a 15 second ultrasonic treatment immediately before sieving began. The initial 21 samples were re-mixed and sieved a second time applying the new procedure (see appendix B for which samples were sieved twice). The additional fine fraction originating in disintegration of aggregates was collected in the same beakers as used for the first round of sieving.

Sieving was performed using the least amount of water possible to increase the preservation of the <63 µm fraction for future analysis. Each sieved fraction, including the beakers holding the <63 µm fraction, was then left to desiccate in a drying cabinet set to 40°C. Sieved fractions were weighed after drying for further investigation of composition.

2.2.4 Coarse fraction analysis

A quantitative investigation of sediment composition was performed using a *Leica MZ 125* binocular. All grain size fractions larger than 125 µm were described visually and different grain types were counted. Categories describing the sediment are summarized in

Table 2.

Table 2: Categories used to describe the coarse fraction composition in ODP Hole 907A.

Volcanoclastic	Terrigenous	Biogenic	Authigenic/Unidentified
Ash (incl. glass shards, altered basalt fragments and obsidian)	Quartz	Agglutinated foraminifera	Aggregates
	Feldspar	Calcareous foraminifera	Oxidized aggregates
Pumice	Biotite	Radiolarians	Gypsum
	Rock fragments	Sponge spicules	Unidentified

There is a high relative proportion of ash throughout the core and all the samples, consequently fluctuations of ash input will likely affect the abundance of other sediment components. To estimate the relative proportion of each constituent, the sediment was placed on a gridded tray as typically used for counting foraminifera. Wherever possible, at least 400 grains were counted for every sample from each grain size fraction. As the last square on the tray was always counted as a whole, the number of grains counted was always 400 or more, except in samples comprised of less than 400 grains. Relative abundance of individual components was calculated using the formula:

*%X = number of X/total number counted grains*100*

(Where X is the grain type)

2.2.5 Surface Textural Analysis of Quartz

Surface texture of quartz grains can reflect the sedimentary environment and transport prior to deposition (Helland and Holmes, 1997, Stickley et al., 2009, Vos et al., 2014). The presence of quartz grains larger than 125 μm in deep marine sediments is usually interpreted as transported by sediment gravity flows, such as turbidity currents or slumps, or as IRD transported by sea ice and/or icebergs (Fronval and Jansen, 1996). As the sediment analysed are likely not influenced by gravity flows (Myhre et al., 1995), the surface texture of quartz grains was examined to distinguish between sea ice and iceberg transport (Helland and Holmes, 1997, St John, 2008, Stickley et al., 2009), using a HITACHI TM3030 Tabletop Scanning Electron Microscope (SEM). Photo micrographs of some reference grains from the 250–500 μm and 500 μm to1 mm fractions have been taken and elemental analysis by Energy Dispersive X-Ray Spectroscopy (EDS) was used to confirm the grains were made of quartz.

Samples composed of over 20% or less than 5% quartz were chosen for analysis; these criteria were set due to time constrains and to enable comparison of surface texture on grains from intervals of higher and lower abundance of quartz grains. The quartz was identified using the same binocular as used for coarse fraction counting. A minimum of 6 quartz grains were handpicked from each chosen sample. All quartz grains were picked if there were less than 6 in total. To remove clay and other contaminants the grains were cleaned using distilled water and a 10-second ultrasonic treatment, minimizing potential formation of new surface textures (Porter,

1962). The grains were left to dry overnight in a drying cabinet set to 50°C, after which they were mounted on aluminium specimen stubs covered with carbon tape for SEM analyses. Up to two photomicrographs of each grain were obtained. Elemental (EDS) analysis was used to verify the grains as quartz in the 500 μm to 1mm fraction. Unfortunately, the EDS system stopped for unknown technical reasons while studying grains in the 250-500 μm fraction and we had to continue without EDS analysis.

Each grain was evaluated for the surface textures listed in Table 3. These textures were chosen as they have previously been described as characteristic of either glacially abraded or sea ice rafted quartz (St John et al., 2015, Woronko, 2016). To unravel the sedimentary history, the grain morphology and surface textures were compared to those reported from previous studies (Helland and Holmes, 1997, Eldrett et al., 2007, St John, 2008, Stickley et al., 2009, Vos et al., 2014, St John et al., 2015, Woronko, 2016).

Table 3: Surface textures used to describe individual quartz grains in ODP Hole 907A.

Morphological	**Mechanical**	**Chemical**
Angular Outline	Conchoidal Fractures	Silica Precipitation
Rounded Outline	Breakage Blocks	Dissolution
Low Relief	Subparallel Lineations	
Medium Relief	Arcuate Steps	
High Relief	Straight Steps	
	Chattermarks	

3 Results

3.1 Geochemical bulk parameters

The total carbon content in the analyzed samples ranges from 0.14 to 0.66 wt. %, with an average of 0.41 wt. % (Fig. 9, Table 4). It exhibits continuously higher values (around 0.6 w.t. %) in the lowermost part of the analyzed interval between 11 to 10.8 Ma, after which it constantly decreases to values around 0.2 wt. % at 10.57 Ma. Subsequently, the TC content increases gradually until 10.45 Ma followed by a significant drop to minimum values (0.14 wt %) at 10.4 Ma. In the upper part of the analyzed section, from 10.3 to 10 Ma, the total carbon content is characterized by fluctuations around 0.3 wt. %. The total organic carbon content displays essentially the same trend as the TC record, but with overall slightly lower values (Fig.9, Table 4).

Table 4: Minimum, maximum and average wt.% of TC, TOC and $CaCO_3$ in cores 13H and 14H, ODP Hole 907A.

	TC (wt. %)	TOC (wt. %)	$CaCO_3$ (wt. %)
Min	0.14	0.13	0.06
Max	0.67	0.63	0.53
Mean	0.41	0.38	0.26

The amount of $CaCO_3$ is lower than TOC, ranging from 0.06 to 0.53 wt.% with an average of 0.26 wt.% (Fig.9, Table 4). From 11 to 10.55 Ma, the $CaCO_3$ displays smaller fluctuations superimposed on a constant trend around 0.3 wt.%, before it increases significantly to over 0.4 w.t.% at 10.55 Ma. A decrease similar to that observed in the TC and TOC records is observed at 10.45 Ma. From 10.37 to 10.0 Ma, the $CaCO_3$ content again displays smaller fluctuations superimposed on a constant trend around 0.3 wt.%.

3.2 Grain size Distribution

Sediment size distribution data was obtained from both coulter counter analysis and wet sieving. Both datasets are presented together in Table 5 to allow for a direct comparison of results. Temporal variation of grain size is shown in (Figs. 10 and 11). Although the sieved sediment contains calcareous material as opposed to the sediment analyzed with coulter counter (see Material and Methods Chapter), the two results are overall comparable as most of the sediment is composed of non-calcareous material such as ash, biogenic-silica and minerogenic components

(Fig.16). Due to the high abundance of ash in the sediment (up to 80 %, Figs.13 and 14) sortable silt analysis was not applied to the coulter counter data. Ash was likely transported to the site by wind, and not by bottom currents. Furthermore, ash has different physical properties than terrigenous silt, and will behave differently with respect to settling velocity of grains sizes (McCave et al., 2006).

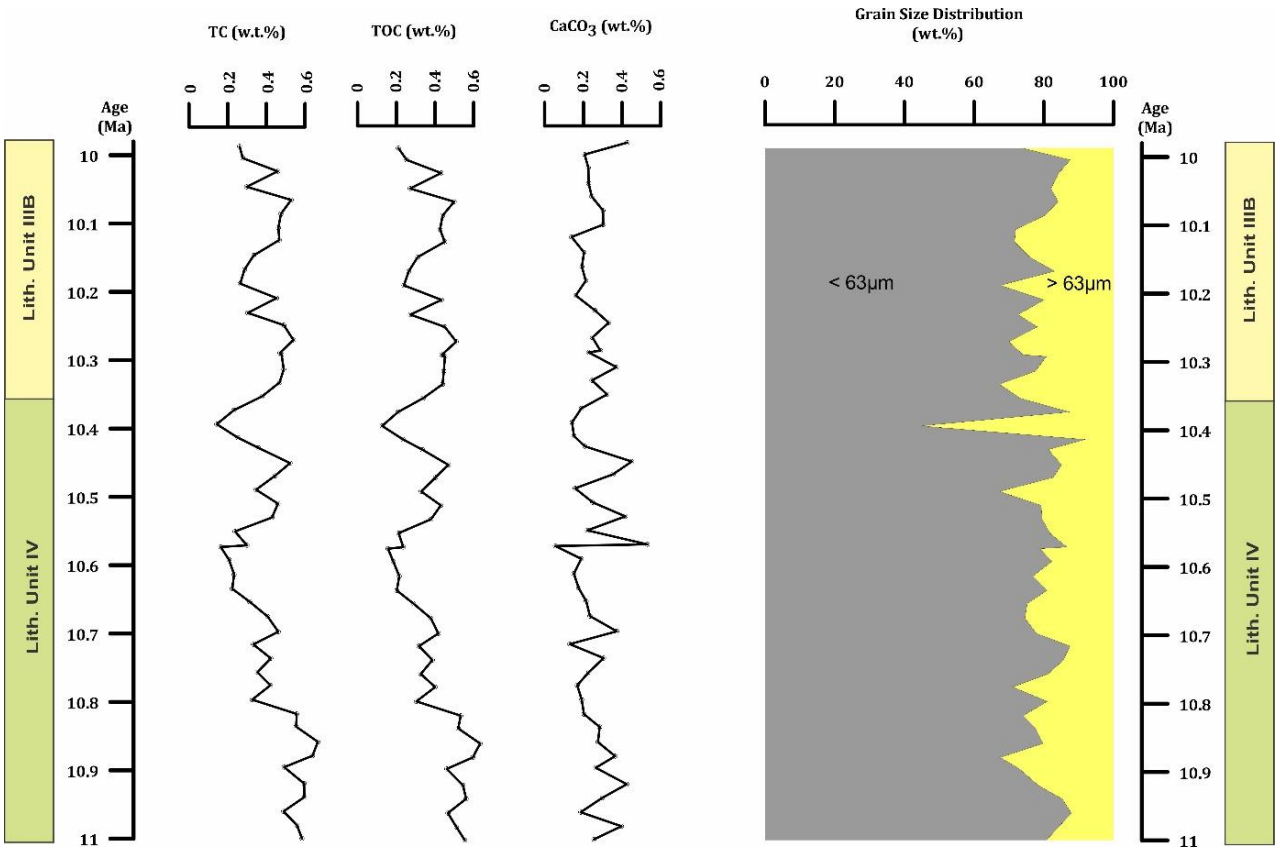

Figure 9: TC, TOC, and $CaCO_3$ content (wt.%) in ODP Hole 907A. Also shown is grain size distribution in Hole 907A obtained from coulter counter analysis.

Coulter counter analysis (CCA) indicate silt (3.9-63 µm) as the most common grain size, ranging from 30 wt. % to 73 wt. %, with an average around 60 wt. % of the sediment composition (Table 5). The second largest contribution comes from clay (< 3.9 µm), ranging from a minimum of 13 wt.% to a maximum of 29 wt. %, with an average of around 20 wt. %. The sand size sediment (63 µm to 2 mm) is most abundant in the 63–125 µm sub-fraction (average 12 wt. %), and becomes gradually less abundant in the larger sub-fractions (Table 5).

Table 5: Comparison of minimum, maximum and mean values (in wt. %) of grain size distribution results obtained from coulter counter analysis and wet sieving in ODP Hole 907A.

Grain Size (µm)		Coulter Counter (wt.%)	Sieving (wt.%)
>3.9	Min	13.30	Min: 63.92
	Max	29.31	
	Mean	19.07	Max: 89.84
3.9–63	Min	29.89	
	Max	72.57	Mean: 83.08
	Mean	59.20	
63–125	Min	4.29	2.43
	Max	21.88	19.27
	Mean	12.23	7.21
125–250	Min	2.14	0.26
	Max	12.66	3.14
	Mean	6.32	0.38
250–500	Min	0.00	0.02
	Max	7.35	3.14
	Mean	1.99	0.38
500–1000	Min	0.00	0.00
	Max	12.99	0.33
	Mean	0.65	0.02
1000–2000	Min	0.00	0.00
	Max	27.88	0.44
	Mean	0.53	0.02
>2000	Min		0.00
	Max		9.04
	Mean		0.17

Results from wet sieving generally show comparable trends as those obtained from CCA, although the < 63 μm fractions (clay and silt) are combined (Table 5). This fraction makes up 83 wt. % of the sediment on average, compared to the average of around 78 wt.% in CCA. The proportion of the sand fraction, however, is consistently lower than that obtained from CCA. Wet sieving also includes the fraction >2 mm, which is composed of granule size pumice in two samples at 116.9 mbsf, and pumice up to 1 cm in diameter at 118 mbsf (~10.35 Ma, Sample 907A-13H5 50-52). Thin volcanic glass shards were also present in this grain size fraction in two samples, at 125.7 and 127.4 mbsf, respectively.

3.2.1 Temporal variation of grain size distribution

Coulter counter analysis shows that the clay fraction (< 3.9 μm) fluctuates from 15 –25 wt. %, with a prominent peak greater than 25 wt. % centered around 10.75 Ma (Fig.10). Between 10.65 and 10 Ma, clay shows an increasing trend with smaller superimposed variability. The silt fraction (3.9–63 μm) shows little variation and constantly remains around 60 wt.% throughout the analyzed interval, with one exception around 10.4 Ma, where it decreases below 40 wt. %. Sieving analysis (Fig.11) combines the clay and silt fractions, which generally contributes 85 wt.% or more to the sediment composition, with three distinct minima at 10.9, 10.73 and 10.35 Ma.

CCA shows that sand in the 63–125 μm and 125-250 μm fractions behaves comparable to each other, with prominent decreases around 10.73, 10.40 and 10.10 Ma. However, peak values in the two fractions are different, with maximum values at 10.90 Ma in the 63–125 μm fraction, and at 10.50 Ma in the 125–250 μm fraction. Sieving analysis confirms the decreases at 10.73, 10.40 and 10.10 Ma in the 125–250- and 250–500 μm fractions. Sand fractions larger than 250 μm are sparse in CCA, generally not exceeding 2 wt.%, except for a few intervals with abrupt, short-term increases in wt. %. CCA display high–frequency variability of sand content in the 250–500 μm fraction.

Sand fractions of the sieving analysis display an overall smaller wt.% compared to CCA, and also shows a lower frequency of variation. The 250–500 μm fraction from sieving analysis display a general trend of increased w.t.% towards 10 Ma, with superimposed fluctuations.

In the fractions larger than 250 μm, the most prominent increases in CCA occur at 10.39 Ma, where sediments in the 500 μm–1 mm and 1–2 mm fractions constitute 15 wt. % and 28 wt.%, respectively. Sieving analysis reflect a similar grain size distribution pattern as the CCA for grain sizes larger than 250 μm, although the prominent increases have a slightly different timing—

occurring at 10.35 Ma in the 250–500 µm and 500 µm-1 mm fraction, and at 10.37 Ma in the 1–2 mm and >2 mm fractions.

An overrepresentation of the coarse fraction is observed in the CCA results, likely due to the presence of aggregates in the sediment. Disintegration of aggregates during sieving causes the difference in wt.% observed between the two methods. Figure 9 shows the highest coarse fraction wt. % at 10.39 Ma, where sediments in the >63 µm size fraction comprise over 50 wt.% of the sediment, while highest coarse fraction wt.% obtained from sieving is 27 wt.% at 10.37 Ma (Fig.11).

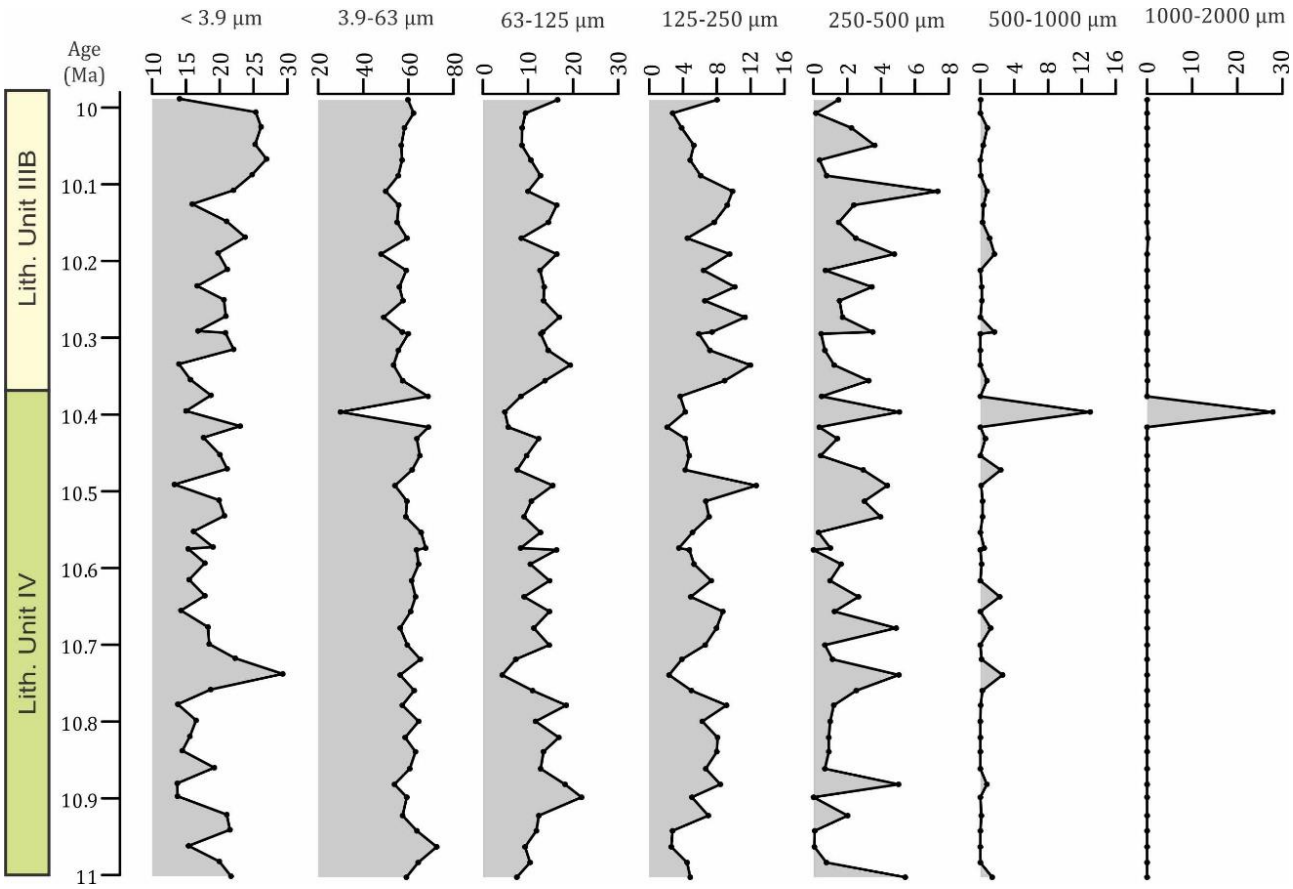

Figure 10: Results from coulter counter grain size analysis showing the relative abundance (in wt. %) of sediments in the different grain size classes in ODP Hole 907A.

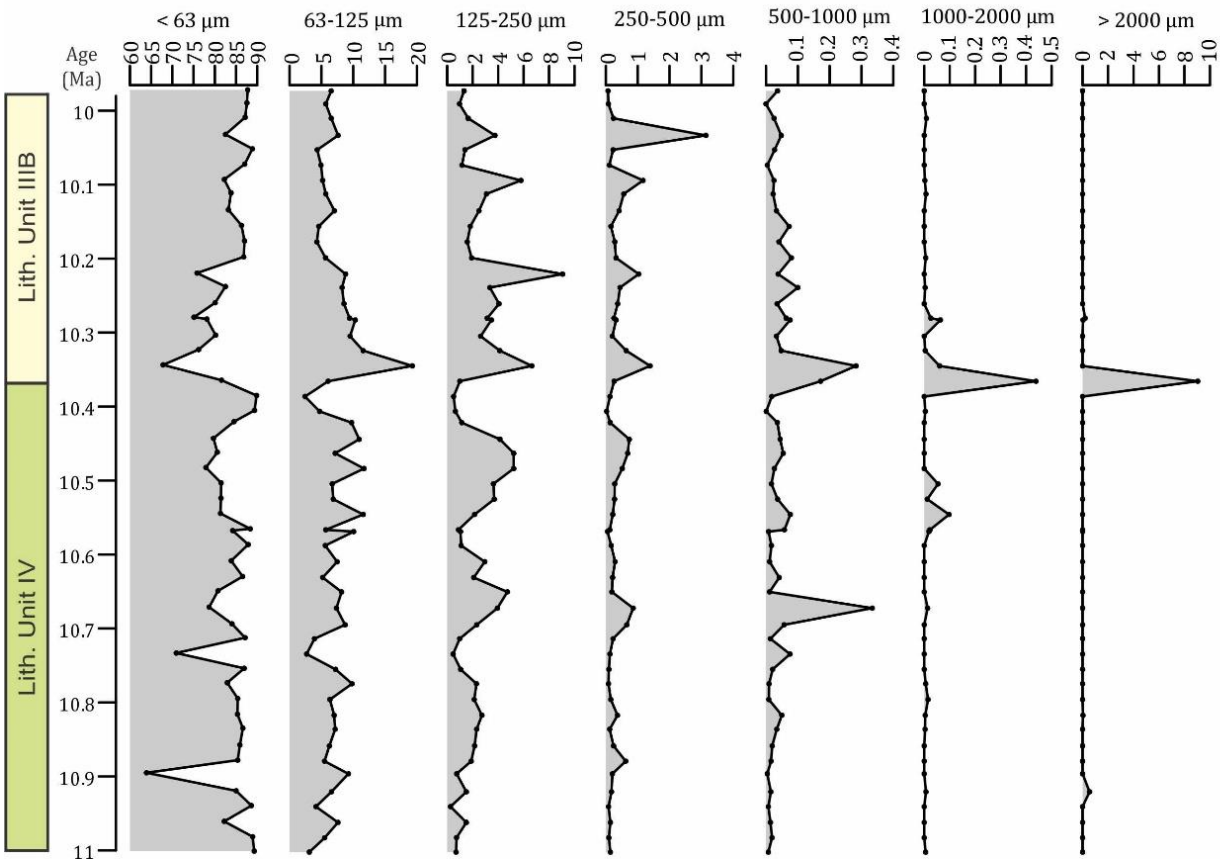

Figure 11: Results from sieving grain size analysis showing the relative abundance (in wt. %) of sediments in the different grain size classes in ODP Hole 907A. Note that in contrast to the coulter counter analysis, the < 63 µm fraction is not subdivided, and grain sizes larger than 2000 µm are included.

3.3 Coarse Fraction Description

3.3.1 Sediment Composition

For the description of the coarse fraction composition, the individual sediment components have been subdivided into volcanoclastic, terrigenous, biogenic, authigenic, and unidentified particles (Fig.12).

The volcanoclastic material is composed of granule sized pumice and ash. The latter consists of both felsic and mafic glass shards, obsidian and sometimes pumice. Volcanoclastic material larger than 2 mm is classified as lapilli according to Fisher (1961). The pumice lapilli are well persevered and do not show any signs of mechanical breakage or chemical weathering. They have a porous appearance when studied under the microscope, while the pores are not visible to the naked eye. Some of the pumice contain phenocrysts of clear, black, or green minerals (Fig.12)

Terrigenous component present are quartz, biotite, feldspar, and rock fragments. Biogenic material is composed of agglutinated and calcareous foraminifera, radiolarians, and sponge spicules. Some of the agglutinated foraminifera observed were over 1 mm in length but only one species could be identified (*Martinotinella communis*), which was also recognized by the Shipboard Scientific Party . Calcareous foraminifera are usually well preserved, although mineral alteration/precipitation seem to have affected some of the specimen observed. The most common calcareous foraminifera are miliolid foraminifera of the genus *Quinqueloculina*.

The authigenic sediment components identified are gypsum crystals and aggregates. The latter are composed of everything the sediment is composed of, such as radiolarians and ash, consolidated by fine particles. The attempt to dissolve the aggregates with H_2O_2 (see Methods chapter) suggests that organic material is involved in their formation. While probably composed of the same material, some aggregates are characterized by a rusty color suggesting oxidation.

Unidentified components are possibly authigenic minerals or altered volcanic fragments.

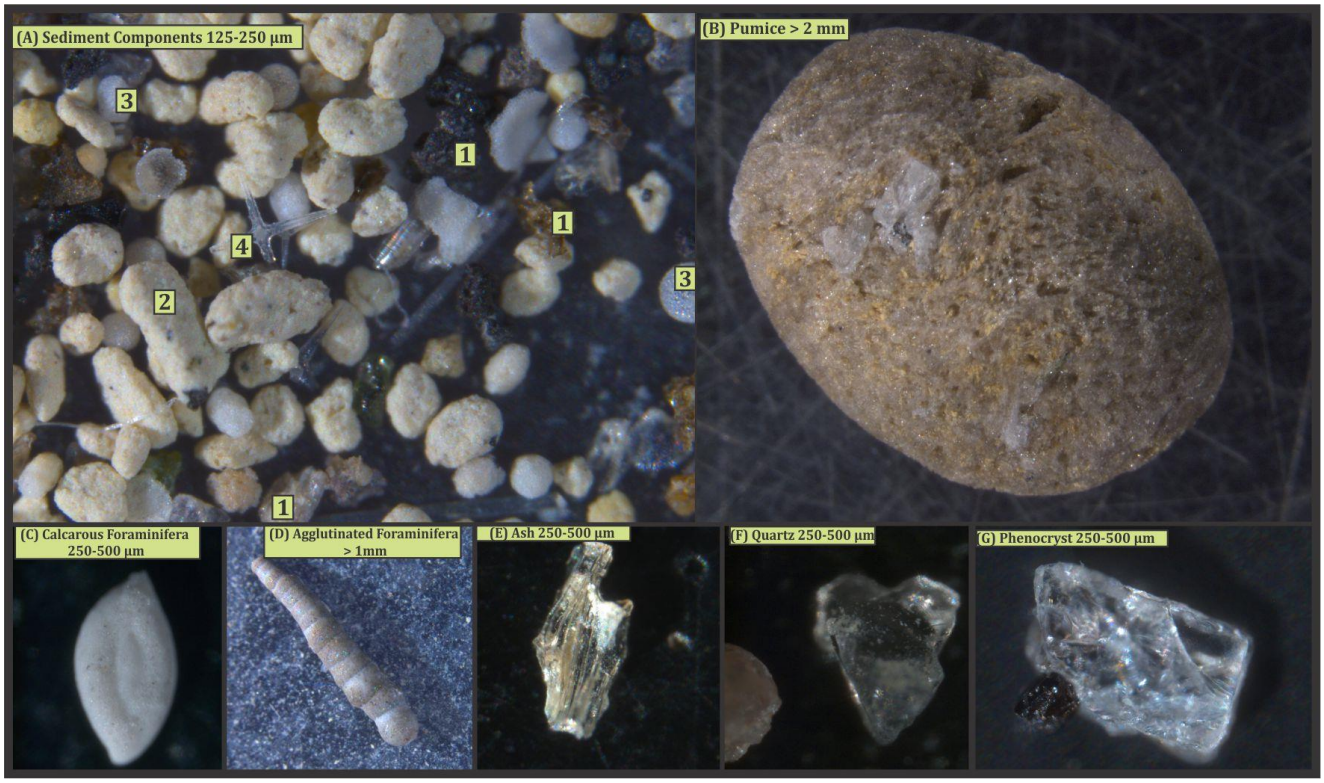

Figure 12: Examples of coarse fraction sediment components observed in the sediment of sections 13H and 14H in Hole 907A. ***A)*** *Sediment example including various ash grains (1), aggregates (2), radiolarians (3), and a sponge spicule (4).* ***B)*** *Rounded pumice containing white and black colored phenocrysts.* ***C)*** *Calcareous foraminifera, Quinqueloculina spp.* ***D)*** *Agglutinated foraminifera, Martinotinella communis.* ***E)*** *Felsic ash glass shard.* ***F)*** *Angular quartz grain.* ***G)*** *Individual phenocrysts of clear and black minerals, counts included in the ash category.*

3.3.2 Relative Abundance of Sediment Components

Sediment components were counted in the 125–250 µm, 250–500 µm, 500–1000 µm, 1000–2000 µm, and >2000 µm fractions. The relative abundance (in %) of the different sediment components has been calculated in order to identify possible changes in depositional patterns and conditions. Figure 13 illustrates the relative abundance of the different components in the 125–250 µm, 250–500 µm, 500–1000 µm fractions.

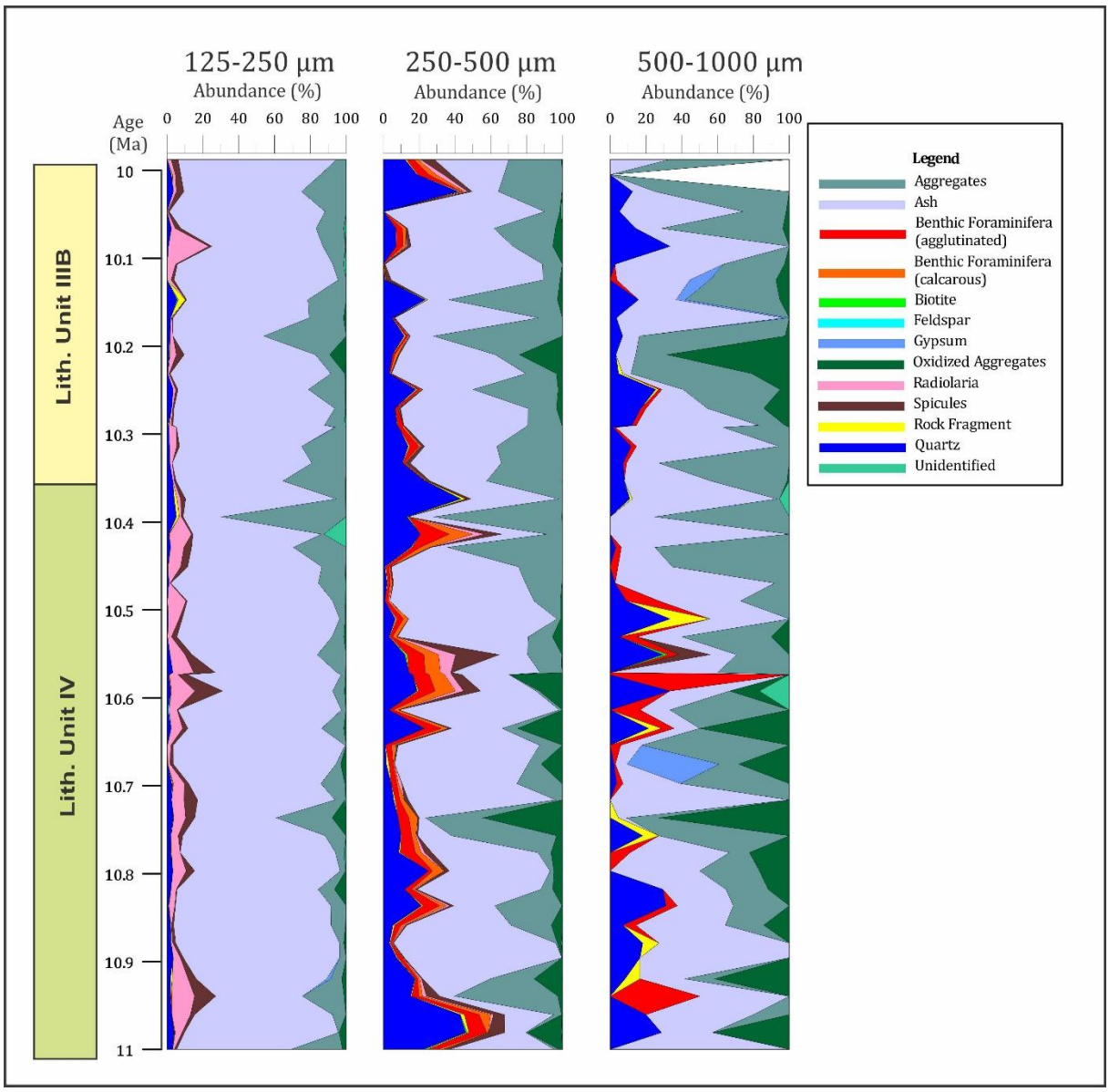

Figure 13: Abundance of various sediment components in the 125−250 µm, 250−500 µm and 500 µm−1 mm fractions in ODP Hole 907A. Particles larger than 1mm (not included in this figure) are rare and consists mainly of aggregates, ash, and pumice (Fig.12).

Ash is the major constituent of the 125–250 μm and 250–500 μm fractions (Fig.13). Other significant components in the 125-250 μm fraction are terrigenous quartz grains, radiolarians, sponge spicules, and aggregates. Significant components in the 250-500 μm fraction are quartz, agglutinated and calcareous foraminifera, sponge spicules, and aggregates, which exhibit higher relative abundances when compared to the 125–250 μm fraction. The most abundant components in the 500–1000 μm fraction are quartz, ash and aggregates. The relative abundance of ash is lower in the 500–1000 fraction compared to the 125–250 μm and 250–500 μm.

3.3.3 Temporal Variation of Sediment Components

3.3.3.1 Volcaniclastic and terrigenous components

Ash is most abundant in the 125–250 μm fraction, with continuously high values fluctuating around 80 wt. % (Fig.14). Prominent declines, however, have been observed at 10.95, 10.75, 10.4 and 10.2 Ma. The abundance of ash in the 250–500 μm and 500 μm to 1 mm fractions show a higher variability than in the 125–250 μm fraction, ranging from ~80 wt% to 0 wt.%. In the 250–500 μm fraction the highest abundance of ash is observed around 10.9 Ma, 10.7, 10.5 and 10.1 Ma. A similar trend is present in the 500 μm to 1 mm fraction. Ash is present in the 1–2 mm fraction as scattered occurrences from 11 to 10.8 Ma, followed by a barren interval from 10.76 to 10.55 Ma, before continuing as scattered occurrences again up to 10 Ma. In this grain size fraction, rounded pumice grains are present in two samples at 10.37 Ma and 10.29 Ma (Fig.14). Two isolated occurrences of bubble-wall shaped glass tephra (similar to picture E in Figure 12), as well as three occurrences of pumice, are observed in the in the > 2mm fraction. The bubble-wall shaped glass occurs between 11 and 10.8 Ma, while the rounded pumice is present at 10.37 and 10.29 Ma.

Quartz is continuously present in sediments < 1mm (Fig.14). It has higher abundance in the 250–500 μm and 500 μm – 1 mm fractions than in the 125–250 μm fraction. In the 125–250 μm fraction, quartz constitutes only up to ~4% of the sediment, in contrast to almost 50 % at 11 Ma in the 250–500 μm fraction. In the three grain-size fractions, quartz is very abundant from 11 to 10.8 Ma. In the 125–250 μm fraction, this interval of high abundance continues until 10.7 Ma, followed by an interval of lower abundance lasting until 10.4 Ma. At 10.39 Ma, quartz increases to 5% in this fraction. Subsequently, a pattern of stepwise decrease characterizes quartz abundance until 10.3 Ma, after which an increase in abundance is observed two times, at 10.25 and 10.15 Ma. The latter showing the maximum values of this fraction. Thereafter, quartz is less abundant and even absent at 10.12, 10.10, and 9.98 Ma. The 250–500 μm fraction displays a gradual decrease following 10.8 Ma, when the abundance decreases to 1.7 % at 10.67 Ma— a significant drop compared to the 46 % observed at 10.98 Ma. From 10.59 to 10.55 Ma, the abundance fluctuates

around 15 %, followed by an interval of lower abundance until 10.42 Ma. The abundance increases to over 40 % at 10.37 Ma, after which it remains below 20 % until 10.02 Ma, where the last peak with over 40 % quartz is observed. The 500 µm–1 mm fraction displays a higher frequency of abundance-variation than the other two fractions. After 10.8 Ma, there is an interval of low abundance until 10.59 Ma, interrupted by an isolated increase at 10.75 Ma. An interval of high-frequency variability is prominent from 10.63–10.48 Ma. Between 10.46 to 10.37 Ma, there is little and even no quartz observed, however, the abundance increases to 11 % at 10.37 Ma and is continuously observed thereafter until 10.14 Ma. It reaches over 33 % at 10.08 Ma, before gradually decreasing towards the top of the studied interval.

Feldspar is only sporadically present in the 125–250- and 250–500 µm fractions, and constitute between 0.2–0.8 % of the total sediment where it occurs (Fig.14). It is more frequently observed between 11 and 10.6 Ma in the 125–250 µm fraction, but only occurs prior to 10.5 Ma in the 250–500 µm fraction.

Biotite is present in grain size fractions up to 1 mm (Fig.14). Occurrences of this mineral are mostly isolated. The only continuous occurrence is between 11.0 to 10.9 Ma in the 250–500 µm fraction.

Rock fragments are present in all fraction up to 2 mm in size (Fig.14). Rock fragment abundance is up to 4 % in the 125-250 µm fraction, and up to 3 % in the 250-500 µm fraction. Rock fragments occur continuously in the 250-500 µm fraction but are most abundant between 11 and 10.8 Ma. They have discontinuous occurrences in the 500 µm – 1mm fraction until 10.5 Ma. At which point they constitute up to 20 % of the sediment, after which only isolated occurrences have been observed at 10.40 and 10.25 Ma. A rock fragment larger than 1 mm is observed at 10.29 Ma.

3.3.3.2 Biogenic components

Biogenic components occur in all grain size fractions except > 2 mm (Fig.15). Foraminifera are most abundant in the lower part of the record between 11 to 10.4 Ma in all counted grain size fractions, but only rarely occur thereafter. Agglutinated and calcareous foraminifera are rare (less than 1 %) in the 125–250 µm fraction, while calcareous foraminifera do not occur after 10.3 Ma in this size fraction. Both agglutinated and calcareous foraminifera are more abundant in the 250–500 µm fraction; both comprising up to 16 % of the sediment in certain intervals. However, the abundance of both clearly declines after 10.4 Ma. A slight increase is observed in the upper part of the analyzed interval between 10.1 to 10.0 Ma. In contrast to calcareous foraminifera, agglutinated foraminifera also occur in the 500 µm –1 mm fraction, being most abundant around

10.6 Ma (~80 %). Two specimens of agglutinated foraminifera have been observed in the 1–2 mm fraction.

Radiolaria and sponge spicules show a more continuous occurrence in the 125–250 µm fraction than foraminifera, but are similar to foraminifera also most abundant in the lower part of the analyzed interval between 11 to 10.4 Ma (

Figure 15). Radiolaria comprise up to 30 % in this fraction, while sponge spicules comprise up to 16 % of the sediment. A reversed abundance pattern, with sponge spicules being more abundant than radiolarians, is observed in the 250–500 µm fraction. Both sponge spicules (20 %) and radiolaria (8 %) exhibit a distinct maximum around 10.55 Ma. Similar to agglutinated and calcareous foraminifera, they only occur sporadically after 10.4 Ma in this size fraction. Sponge spicules occur in the 500 µm – 1 mm only in one sample at 10. 55 Ma (16 %) and one specimen has been observed at 10.11 Ma in the 1–2 mm fraction.

In summary, all biogenic components are common constituents of the sediment (125–500 µm fractions). They show varying abundance in the lower part of the studied section (11 to 10.4 Ma), after which they only occur sporadically. This indicates decisive changes occurring around this time.

3.3.3.3 Authigenic and unidentified components

Authigenic and unidentified components occur in all fractions except the > 2mm fraction (Fig.16). Gypsum crystals are rare but occur in the 125–250 µm (10.9 and 10.3 Ma) and 500 µm–1mm fractions (at 10.68 and 10.12 Ma).

Aggregates occur in all size fractions up to 1 mm and their abundance varies significantly throughout the analyzed section (Fig.16). In the 125–250 µm fraction aggregates typically constitutes 5 to 15 % of the sediment, but increase up to 45% at 10.18 Ma, and 69% at 10.39 Ma. Aggregate abundance shows high-frequency variability throughout the analyzed interval within the 250–500 µm and 500 µm – 1mm fractions. Three peaks with abundances above 35 % occur between 11 and 10.7 Ma in the 250–500 µm fraction, followed by an interval of lower abundances between 10.7 and 10.5 Ma. The upper part of the studied interval (above 10.5 Ma) shows a higher frequency of fluctuations in this fraction and overall higher abundance of aggregates than in the lower part. The 500 µm– 1mm fraction display a lower abundance with an increasing trend from 11 to 10.8 Ma, and high frequency variability from 10.8 to 10 Ma.

Oxidized aggregates occur in the same fraction as the other aggregates except in the >1 mm fraction (Fig.16). They are present between 11 to 10.5 Ma, and around 10.28 Ma in the respective fractions. In the 125–250 μm fraction, oxidized aggregates commonly constitute less than 1 %, with a peak value of 7.8 % at 10.73 Ma. In the 250–500 μm fraction the amplitude of abundance-variation is greater than in the former fraction, varying from a minimum of 0% to a maximum of 44 % between 11 and 10.5 Ma. After 10.5 Ma, oxidized aggregates only occur sporadically in this fraction and abundances never reach above 5 %. In the 500 μm – 1 mm fraction oxidized aggregates commonly constitute less than 20% between 11 and 10.5 Ma, interrupted by superimposed peaks, the largest (72%) at 10.73 Ma. A nearly barren interval continues to 10.28 Ma, after which a peak (68%) is observed at 10.2 Ma.

Unidentified grains occur in all fractions up to 2 mm. In the 125–250 μm fraction, they are rare and occur only sporadically, but comprise over 8% of sediments at 10.4 Ma. They occur more frequently in the 250-500 fraction but always constitute less than 1 % of the sediments. In the 500 μm – 1mm fractions, unidentified grains occur in two samples at 10.37 and 10.6 Ma, reaching abundances of 6 % and 16 %, respectively.

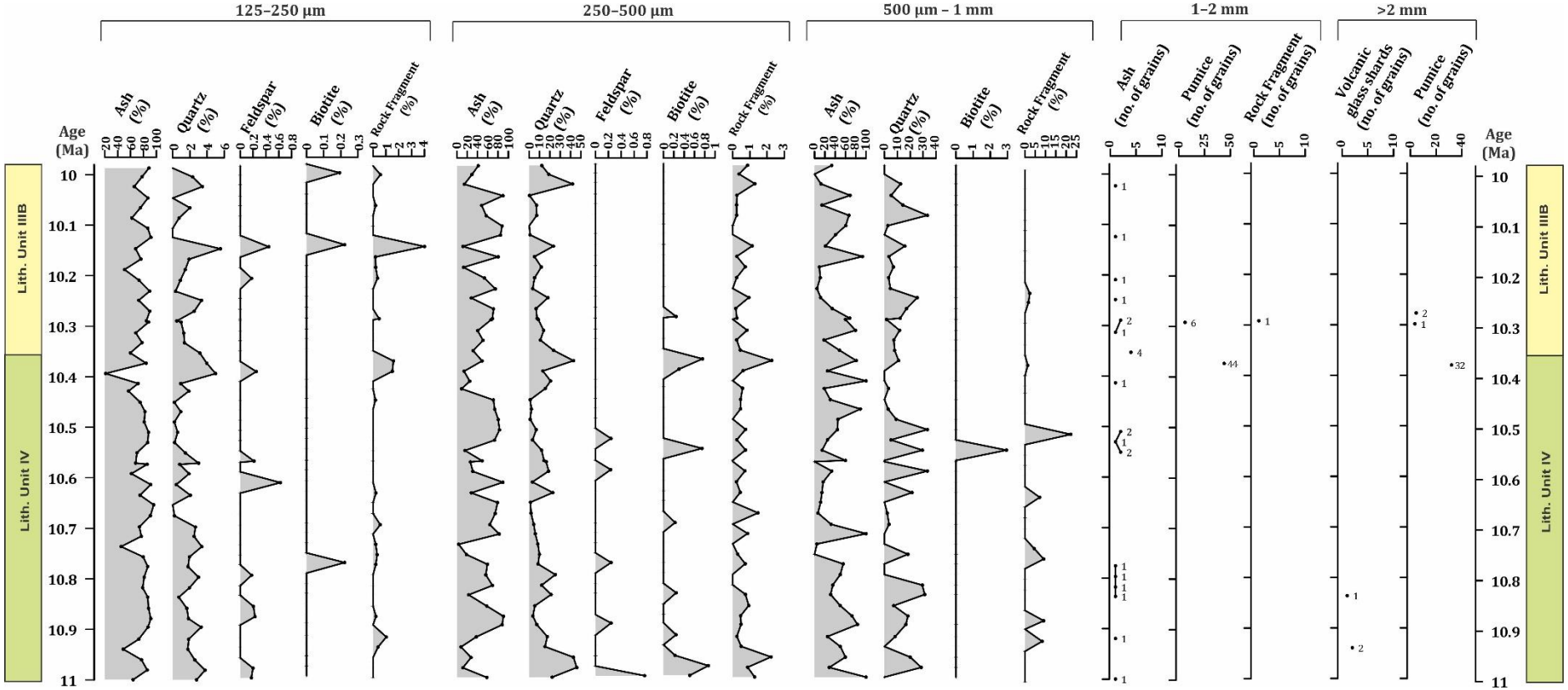

Figure 14: Temporal variation of volcanoclastic and terrigenous components (given in %) in ODP Hole 907A.

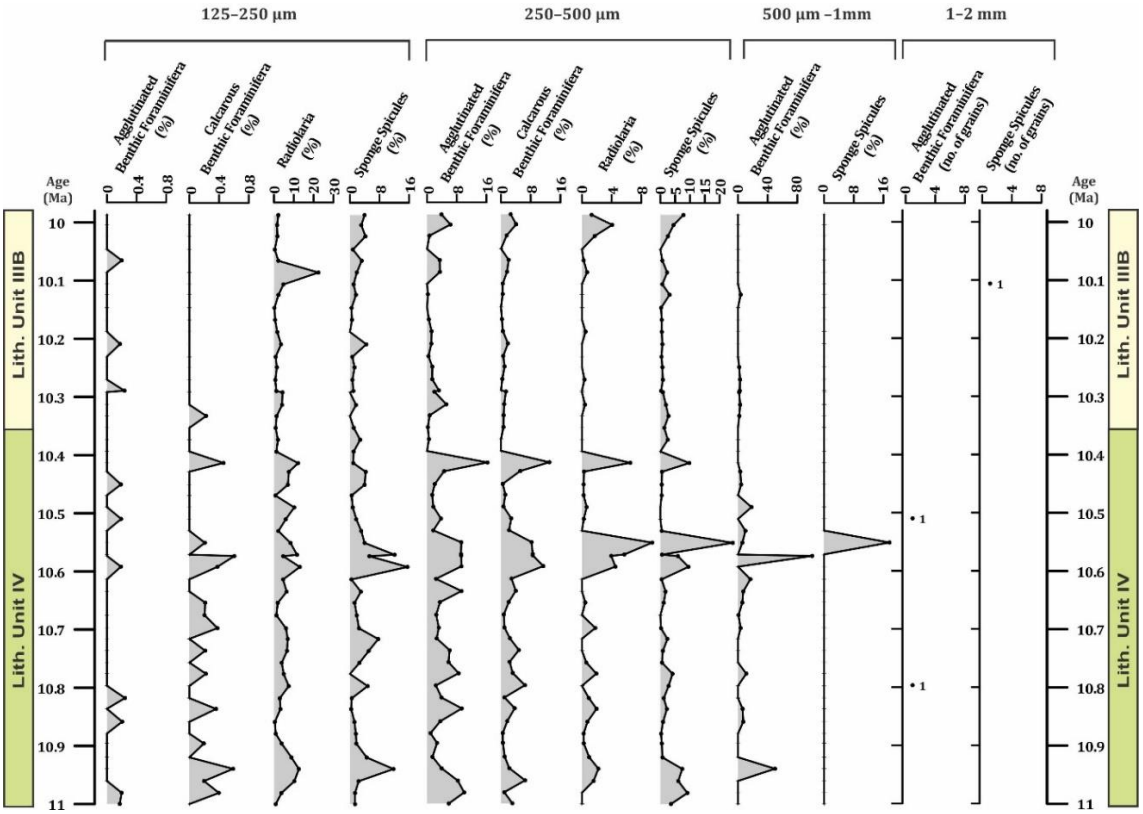

Figure 15: Temporal variation of biogenic components in the 125–250 µm, 250–500 µm, 500 µm – 1 mm, and 1–2 mm fractions in ODP Hole 907A. The abundance is given in percentage relative to the total sediment composition for fraction 125 µm to 1mm, while it is given as number of grains for the 1–2 mm fraction.

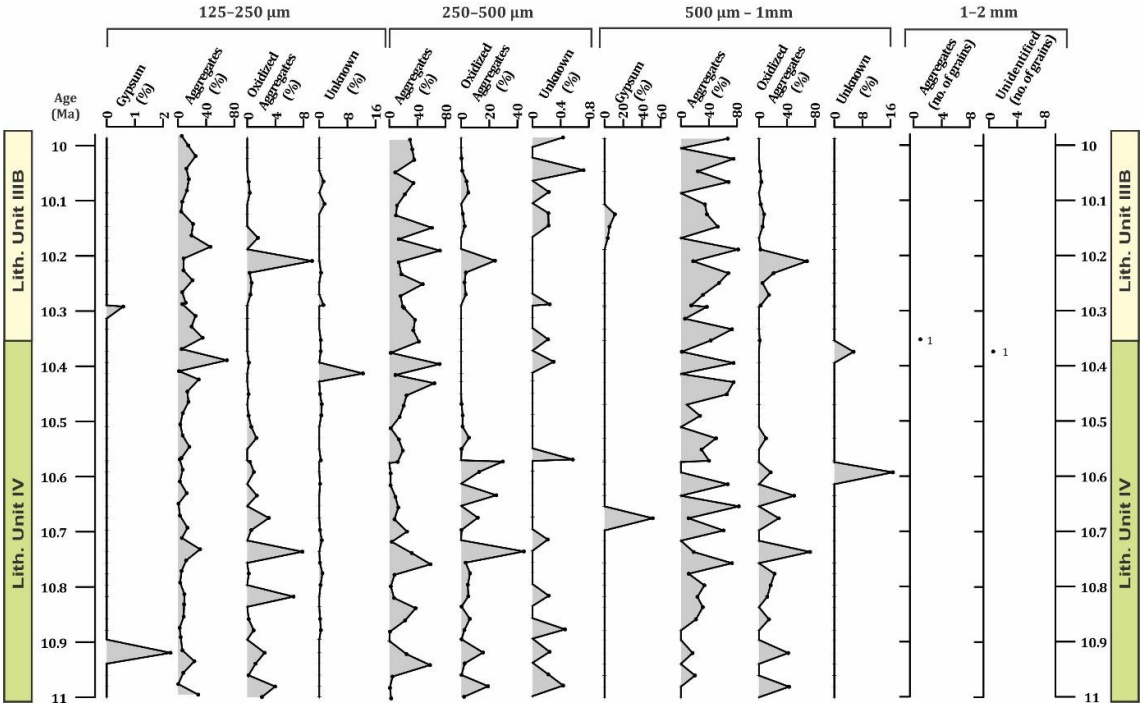

Figure 16: Temporal variation of authigenic and unidentified components in the 125-250 (A), 250-500 (B), 500-1000 (C), and 1000-2000 (D) fractions ODP Hole 907A. The abundance is given in percentage relative to the coarse sediment composition for the 125 µm to 1 mm fraction, while it is given in number of grains for the 1–2 mm fraction.

3.4 Surface Texture Analysis of Quartz

Quartz from 33 samples in the 250–500 μm and 500–1 mm fractions were studied using SEM (Fig.17), for grain shape (angular, subangular, subrounded or rounded), surface relief (high, medium, or low) and surface textures. The surface textures were differentiated into mechanical surface textures, which include conchoidal fractures, breakage blocks, straight and arcuate steps, subparallel lineations, and chattermarks, and chemically induced surface textures, which include silica precipitation and dissolution. In all the examined quartz grains, the most common textures observed are conchoidal fractures (79%), silica precipitation (74%) and dissolution (64%). The majority of analyzed grains have medium relief (52%) and a subangular shape (43%) (Table 6).

Table 6: The abundance (%) of microfeatures in quartz grains in ODP Hole 907A.

Grain Microfeature Category	Microfeature	Grains Showing Feature(%)
Grain Shape	Angluar	13.64
	Subangular	43.39
	Subrounded	29.75
	Rounded	13.22
Grain Relief	Low relief	19.84
	Medium relief	52.48
	High relief	28.10
Grain Surface Textures	Chattermarks	8.26
	Straight steps	41.32
	Arcuate steps	35.54
	Subparallell striations	4.13
	Breakage blocks	52.10
	Conchoidal fractures	78.51
	Dissolution	64.05
	Silica precipitation	73.97

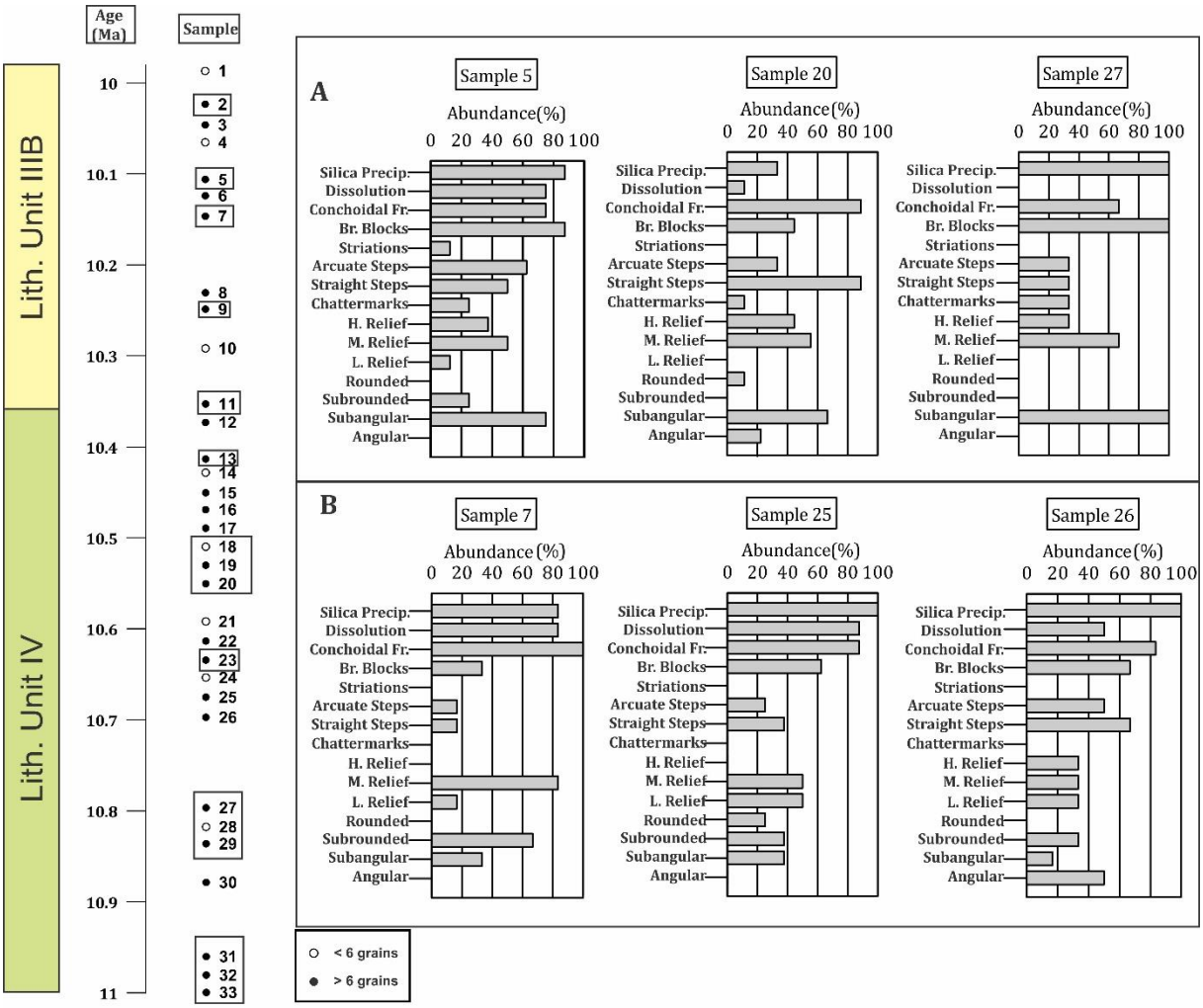

Figure 17: Samples used in quartz surface texture analysis in ODP Hole 907A. Filled dots are samples where six or more quartz grains are studied; blank dots are samples where less than six quartz grains are studied. Samples numbers placed in boxes are samples that contain over 20 % quartz. ***A****.Samples 5, 20, and 27 are the three samples (consisting of more than 6 grains) with the highest abundance of typical glacial surface textures.* ***B****. Samples 7, 25, and 26 are the three samples (consisting of more than 6 grains) with the lowest abundance of typical glacial surface textures.*

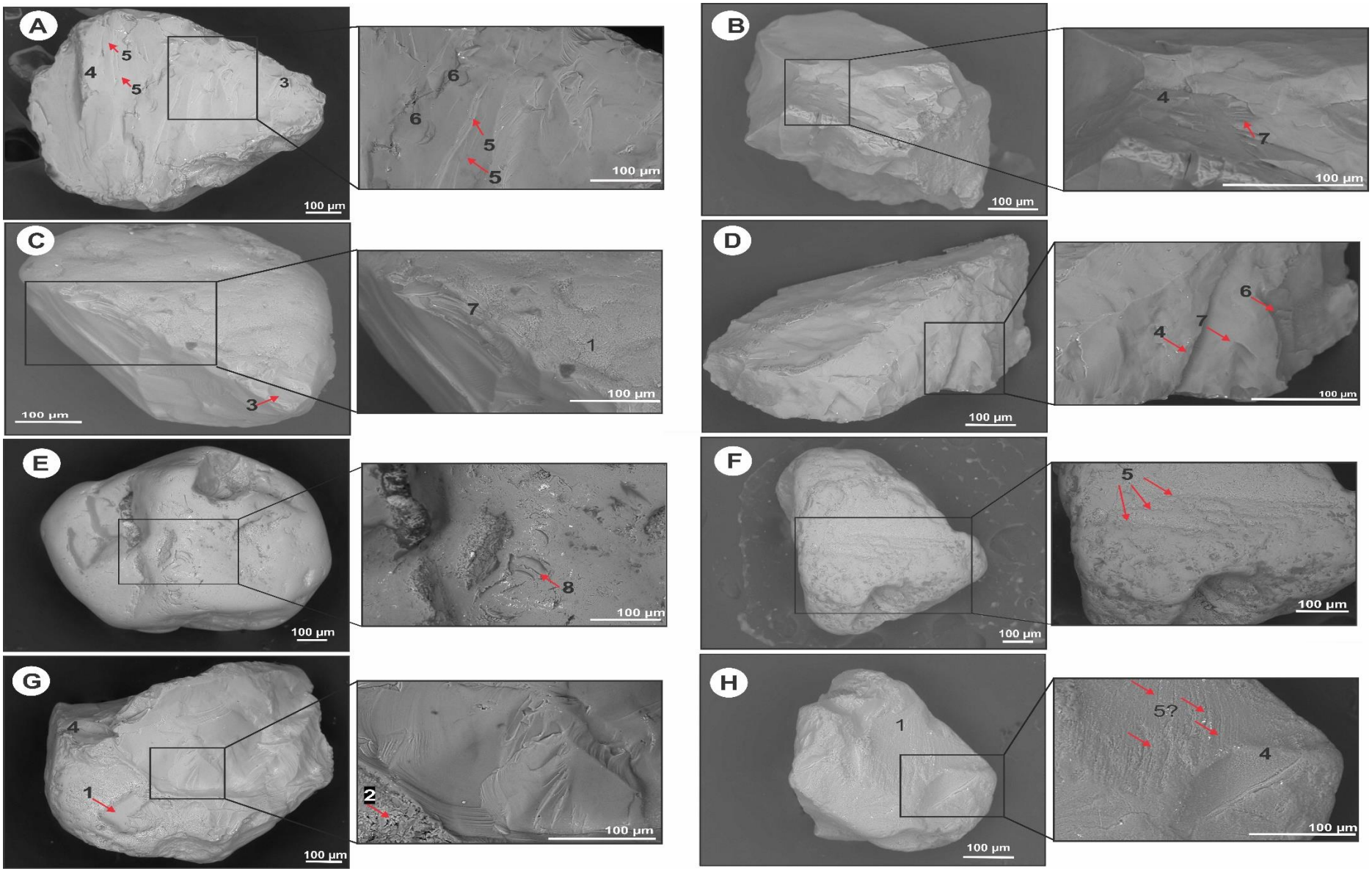
A
5
4
5
3
100 µm
6
6
5
5
100 µm
B
100 µm
4
7
100 µm
C
100 µm
3
7
1
100 µm
D
100 µm
6
4
7
100 µm
E
100 µm
8
100 µm
F
100 µm
5
100 µm
G
4
1
100 µm
2
100 µm
H
1
100 µm
5?
4
100 µm

Figure 18: See figure on previous page. SEM micrographs of representative quartz grain surface textures in ODP Hole 907A. ***A****. Subangular, low relief quartz grain with fresh looking surface and mechanical surface textures, breakage block(4), subparallel lineations(5), and arcuate steps (6).* ***B****. Angular-, high relief grain with fresh looking surface and mechanical surface textures, breakage block (4) and straight steps (7).* ***C****. Subrounded-, low relief grain, with one fresh looking surface displaying mechanical surface textures; conchoidal fracture (3), straight steps (7), rest of the grain looks abraded and displays silica precipitation (1).* ***D****. Subangular-, medium relief grain with fresh looking surface displaying breakage blocks (4), straight (7) and arcuate (6) steps.* ***E****. Subrounded-, medium relief grain displaying chattermarks (8).* ***F****. Subrounded-, low relief grain showing subparallel lineations (5).* ***G****. Subangular-, high relief grain with fresh looking surface displaying mechanical surface textures, breakage block (4) and one side chemically altered by euhedral silica overgrowths (1) and dissolution (2).* ***H****. Subrounded-, medium relief grain displaying surface characterized by silica precipitation (1), possible subparallel lineations (5), and breakage block (4).*

4 Discussion

ODP Site 907 is presently located under the influence of both southward flowing fresh and cold East Greenland Current and the northward flowing warm and saline Atlantic water (see Chapter 1.2.2), hence, the site is ideally suited to study how circulation and paleoenvironmental conditions in the Norwegian-Greenland Sea may have evolved. In the following chapter, the results of this thesis will be discussed and subsequently compared to other paleoclimate proxy records from the Norwegian-Greenland Sea in order to depict paleoenvironmental changes in the Iceland Sea, and its implications for paleoclimate across a 1-million year interval during the early Late Miocene (11.0 Ma to 9.98 Ma).

4.1 A 1-Myr record of ice rafting in the Iceland Sea

At present day, ODP Site 907 is located in an open-ocean environment on the Iceland Plateau (Thiede and Myhre, 1996). Plate tectonic reconstructions of the Norwegian-Greenland Sea indicate that open-ocean conditions have persisted on the Iceland Plateau at least since the Middle Miocene (Thiede et al., 1998). Away from the continental slope or bathymetrical highs, where turbidity currents or other slope processes may transport coarse-grained terrigenous material, the occurrence of material such as quartz or rock fragments larger than 125 μm indicates transport through ice rafting from surrounding continents (e.g. Gilbert, 1990, Bond et al., 1992, Nürnberg et al., 1994, Fronval and Jansen, 1996).

Visual inspection of the coarse fraction is important in order to verify its nature as ice rafted debris. As it may also be composed of predominant biogenic and/or volcanic material. Sieving of the sediments revealed very abundant aggregates and ash, making it evident that the coarse fraction is overrepresented in coulter counter results (Figs.11 and 12). In addition, abundant ash and aggregates complicate the interpretation of the coarse-grained terrigenous input as a proxy for ice rafting, since apparent variations in quartz abundance may be the result of variations in ash input, as Stabell and Koç (1996) point out in a diatom study from the same site. However, if ash transport and deposition at the study site are relatively constant and without larger variations throughout the studied interval, then increased abundance of quartz may still record events of increased ice rafting. Late Miocene ash layers at ODP Site 907 apparently show affinity to explosive eruptions on Iceland, and were most likely airborne before deposition (Werner et al., 1993). Nevertheless, the study presented here reveals a continuous presence of non-volcanic, terrigenous material larger than 125 μm at ODP Site 907, which regardless of ash input, indicates ice rafting in the Iceland Sea during the early Late Miocene (Fig.19)(e.g. Fronval and Jansen, 1996).

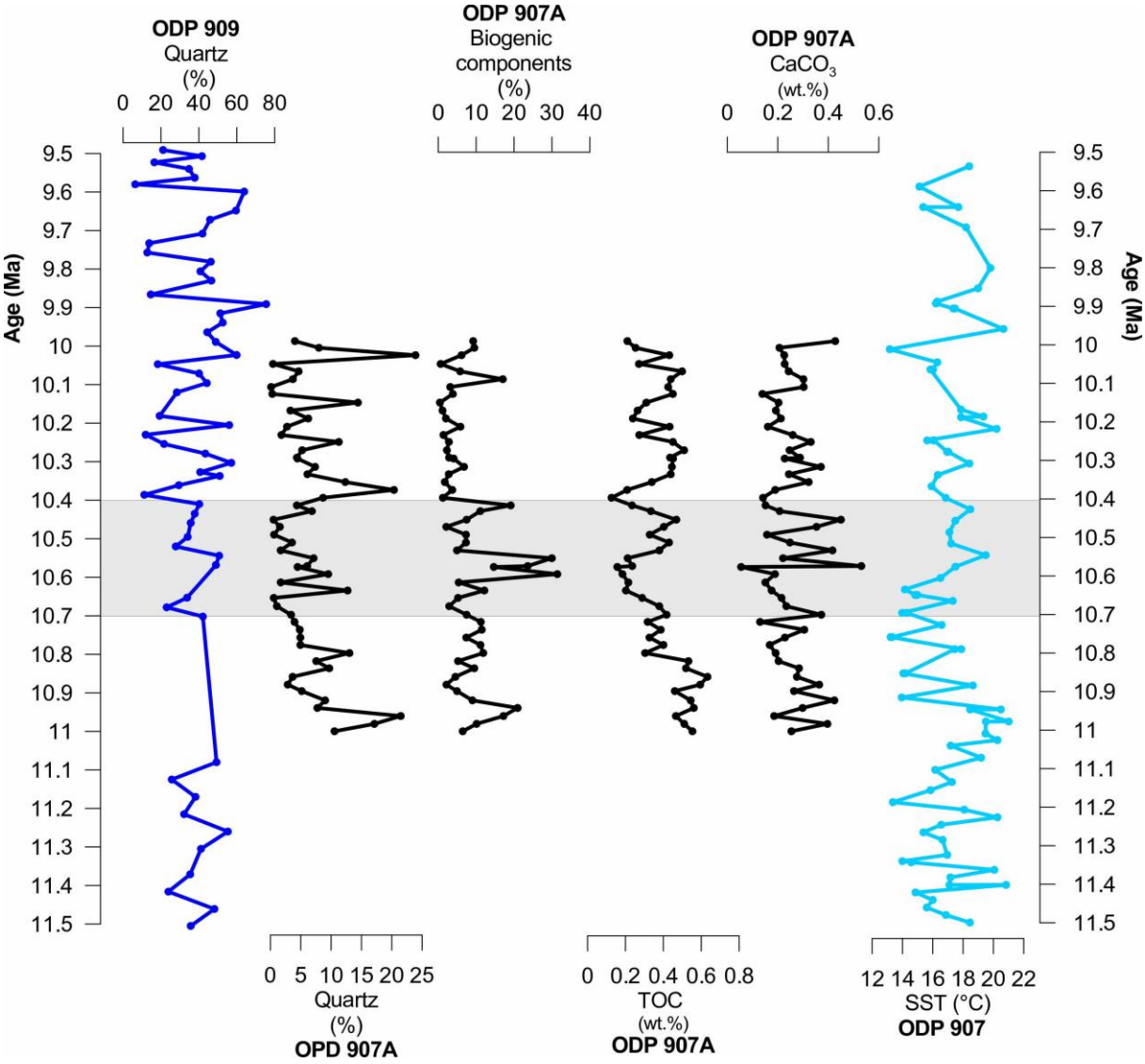

Figure 19: Comparison of abundance (%) of quartz and biogenic components (combined 125 µm to 1 mm fractions). TOC (wt.%) and $CaCO_3$ (wt.%) in ODP Hole 907A to quartz abundance in ODP Site 909 (Winkler et al., 2002) and SST reconstruction from Site 907 (Herbert et al., 2016). The highlighted interval is the timing for Mi-6 proposed by Westerhold et al. (2005).

4.1.1 Iceberg or Sea Ice Rafted Debris

In studies of IRD from subpolar regions, coarse-grained sediments in hemipelagic sediments are usually considered iceberg rafted (e.g. Bond et al., 1992). It is a common consensus to assume that sea ice rafted debris usually encompass an assemblage of finer sediment (< 250 µm) compared to iceberg rafted debris (Nürnberg et al., 1994, Darby, 2008). The most common sediment entrainment process of sea ice is thought to be suspension freezing, where open-water convection at shallow depths (<30 m) causes super-cooled bottom water to form crystals near the seafloor (Reimnitz et al., 1993). As sea ice crystals form, they incorporate material suspended by turbulent mixing, which then floats to the surface with the sea ice. This material is usually finer than >250 µm, however under certain circumstances sea ice may entrain up to cobble size material (Reimnitz

et al., 1987). In the Arctic Ocean, coarser sea ice sediments (>250 μm) are common due to the vast extension of the continental shelf, where sea ice typically entrain sediment by freezing to the bottom in shallow marine environments (Reimnitz et al., 1987, St John, 2008). In contrast, sediments picked up by glaciers can be any grain size and consist of everything in the vicinity of a glacier (Gilbert, 1990). This implies that iceberg rafted debris may show any shape, form, and texture. However, typical features used to distinguish iceberg transported material are produced by mechanical breakage (e.g. Vos et al., 2014, St John et al., 2015). Sediments transported by sea ice, or exposed to periglacial environment, are prone to chemical weathering, which may erase pre-existing glacial signatures (Woronko, 2016). However, when glaciers calve into the ocean, glacial signatures on the grains are better preserved, which makes it possible to distinguish sediment as transported by icebergs (St John et al., 2015).

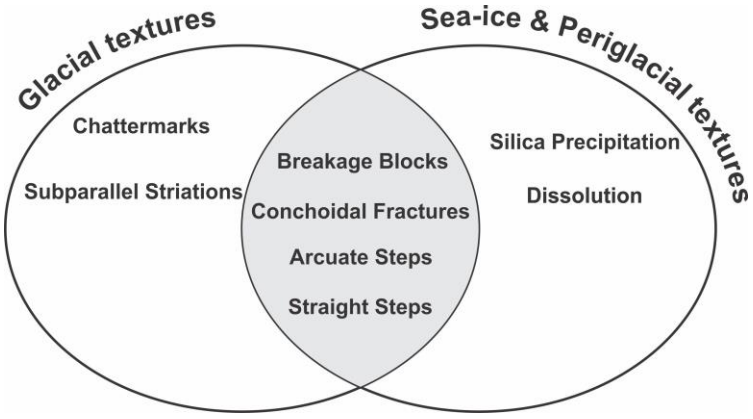

Figure 20: Quartz micro-textures typical for glacial environment, periglacial environment and sea ice transport (St John et al., 2015, Woronko, 2016).

SEM analysis of quartz grains from the >250 μm grain size fractions reveal surface textures indicative of both iceberg and sea ice transport. Typical grain surface textures of glacially abraded quartz are angular to subangular outlines, high relief, and mechanical breakage textures such as subparallel lineations, chattermarks, conchoidal fractures, straight and arcuate steps (e.g. St John et al. 2015, Woronko, 2016), (Fig.20). Grains bearing these glacial micro-textures appear throughout the analyzed section (Fig.17), confirming that ice rafting with icebergs has occurred several times during this ~1 Myr time interval. However, most grains analyzed also display textures indicative of sea ice transport (Figs.17 and 20), these being predominantly rounded grains with signs of silica precipitation and dissolution features (St John et al., 2015). Given the abundance of silica precipitation observed, it is also possible that the sediment has been transported to the study site by sea ice. If a glacial entrainment of grains prior to sea ice transport have occurred, then the glacial signatures were not completely erased by chemical weathering during sea ice transport. However, sea ice transport of analyzed sediments seems less likely considering the distance from the study site to the Arctic Ocean and recently published SST

reconstructions from ODP Site 907 (Herbert et al., 2016, see also discussion below). In addition, careful SEM examination of grains bearing features of both iceberg and sea ice transport suggests that the glacial micro-textures are the youngest surface features overprinting older textures (Fig.18). The grains are therefore interpreted to be transported as iceberg rafted debris.

If IRD was indeed transported by sea ice to the study site, its formation during this time interval must be discussed. A recent IP_{25} –sea ice biomarker study suggests that a seasonal sea ice cover existed in the central Arctic Ocean during the late Middle to early Late Miocene (Stein et al., 2016), presenting a possible source of sea ice. As Fram Strait is open for water mass exchange since at least the Middle Miocene (Jakobsson et al., 2007), sea ice may have been transported from the Arctic Ocean to the Norwegian-Greenland Sea via the Transpolar Drift and the EGC. However, the reconstruction of paleo-bathymetry of the Barents sea and provenance study at Site 909 suggests that IRD at ~14 Ma was transported by icebergs calving from an early Barents Sea Ice Sheet (Knies and Gaina, 2008). In addition, for potential Arctic Ocean sea ice or icebergs to reach the Iceland Sea rather cold surface waters are required. Early Late Miocene sea surface temperature reconstructions in the Iceland Sea indicate warm surface waters around 16–17 °C (Fig.19, Herbert et. al., 2016), which seems unlikely for sea ice to survive transport from the Arctic Ocean as far south as the Iceland Sea. In comparison, seasonal sea ice cover has been indicated to exist in the Iceland Sea in the Late Pliocene (3.5 –3.0 Ma), during a time when sea surface temperatures were only 2 to 3 °C higher than the present-day (Herbert et al., 2016, Clotten et al., 2018).

Given the prevalence of relatively warm surface waters in the Iceland Sea, a more likely source of the IRD recorded between 11–10 Ma at ODP Site 907 are icebergs coming from sources closer to the study site. Evidence for the occurrence of IRD at ~11 Ma has been reported from Site 918 in the Irminger Basin off the southeastern coast of Greenland and IRD originating from Greenland has been described from that site since at least ~9.5 Ma (Helland and Holmes, 1997). This suggests Greenland as the most likely source of IRD in the Iceland Sea, similar to the suggested source of younger IRD at Site 907 (Fronval and Jansen, 1996). A gneissic dropstone observed by the Shipboard Scientific Party (1995) at depth equal to 10.2 Ma during drilling of Hole 907A further supports the possibility of ice rafting with Greenland as the most likely source, as large parts of East Greenland is composed of Caledonian metamorphic rocks and Precambrian basement (Thrane, 2002). However, no such dropstone was discovered in this study and the lithology of rock fragments observed in the coarse fraction have not been described due to time constrains, thus it remains unclear from where they originate.

4.1.2 Late Miocene IRD in the Norwegian-Greenland Sea

Atlantic inflow across the Greenland Scotland Ridge and increased production of North Atlantic deep water is thought to have occurred already from 12.5 Ma as indicated by a change from siliceous to biogenic carbonate deposition (Wright et al., 1992, Fronval and Jansen, 1996). This initial change in circulation towards more modern-like thermohaline circulation coincides with pulses of IRD reported from the Vøring Plateau. This indicates cooling in the Northern Hemisphere and consequential buildup of small-scale glaciers on the continents surrounding the Norwegian-Greenland Sea (Fronval and Jansen, 1996, Thiede et al., 2011). Prior to this study, however, the IRD record from Iceland Sea ODP Site 907 only extended back to ~8 Ma (Fig.21) (Fronval and Jansen, 1996). The high resolution record presented in this thesis confirms the occurrence of IRD back to 11 Ma and indicates continuous ice rafting in the Iceland Sea in the early Late Miocene (11 to 9.98 Ma). The presence of IRD in the Iceland Sea coincides with IRD recorded in the Fram Strait (Winkler et al., 2002), on the Vøring Plateau (Fronval and Jansen, 1996), and in the Irminger Basin (Helland and Holmes, 1997), where the earliest IRD pulse is dated to ~11 Ma (Helland and Holmes, 1997) .

Ice rafting in the Irminger Basin and in the Iceland Sea suggests the build-up of small-scale glaciations on Greenland, probably related to strengthening of the East Greenland Current precursor, and development of a stronger east-west temperature gradient within the Norwegian-Greenland Sea. Global $\delta^{13}C$-records indicate significant increase of proto-NADW after 12 Ma, likely related to both shoaling in the Central American Seaway and depth variations of the Greenland-Scotland Ridge (Wright and Miller, 1996, Droxler et al., 1998, Poore et al., 2006). In particular, uplift of the Icelandic Plume underlying the Denmark Strait affects the signal of proto-NADW and indicates the Denmark Strait as the main area of deep water overflow from the Norwegian-Greenland Sea into the North Atlantic during the Late Miocene (Poore et al., 2006). According to Wei (1998), both deep waters and cold surface waters were exported through the Denmark Strait with the proto-EGC, therefore supporting the inferred cooling and occurrence of IRD along the East Greenland margin. In addition, uplift of Greenland initiated around 11 to 10 Ma (Japsen et al., 2006), may have promoted the formation of glaciers in mountain areas and subsequent growth large enough to reach sea level.

4.2 Rare Pumice Occurrence— possible indications of surface currents?

A flat rock covered in pyrite crystals has been described during shipboard analysis as a dropstone occurring around 10.28 Ma but it was noted as a possible contaminant (Shipboard Scientific Party, 1995). Interestingly, the timing of its occurrence coincides with the rounded and sometimes flat pumice observed in the > 1 mm coarse fraction during this study (Fig.14). Pumice is a volcanic rock typically produced by plinian eruptions (Sparks et al., 1977). Its most likely source is Iceland similar to that of the ashes in this interval of Hole 907A (Sparks et al., 1977, Werner et al., 1993). Oceanic transport of rounded pumice by currents has been reported off Reykjanes around 1200 AD, and pumice has been observed rafting around the northern and western coast of Iceland for several months with the Irminger current (Larsen et al., 2014). Although speculative, this may indicate that Miocene surface currents north of Iceland were somewhat similar to the modern-day surface currents in the area. The contemporaneous occurrence of the described dropstones with the pumice observed during this study may suggest that this is not a dropstone, but a misidentified volcanic rock with phenocrysts similar to some of the pumice clasts identified here (see microscope pictures in Fig.12).

4.3 Biological Turnover

The most prominent feature of the Hole 907A record studied in this thesis is a significant drop in biogenic components at ~10.4 Ma (Figs.15 and 19). The decrease is evident in both agglutinated and calcareous foraminifera, as well as in radiolaria and sponge spicules, which all are commonly present before 10.4 Ma but are very rare thereafter— indicating incisive environmental changes occurring in the Iceland Sea around this time. At the same time, a dinoflagellate cyst disappearance event (Schreck et al., 2013) and a decrease in diatom abundance (Stabell and Koç, 1996) have been reported from ODP Site 907, both interpreted as a biologic response to cooling surface waters and possible ice rafting in the Iceland Sea. In agreement with their interpretation, the Hole 907A record shows an increase of coarse fraction wt.% (>63 μm, Figure 11) at 10.37 Ma, which coincides with maxima in quartz abundance (Figure 19). This may indicate increased ice rafting, however, mass accumulation rates of IRD should be calculated to further strengthen this interpretation. A drop in TOC occurs contemporaneously with the increase in coarse fraction wt.%, and as the C/N ratio < 10 (Schreck et al., 2013) indicates a marine source of the organic matter at Site 907 (Stein, 1990), this may reflect a decrease in marine productivity at ~10.4 Ma. A general cooling in the Northern Hemisphere after ~10.5 Ma is also indicated by bottom water cooling at North Atlantic ODP Site 982 (Andersson and Jansen, 2003), supporting the changes observed in the Iceland Sea.

From 11 to 10.6 Ma, just prior to the biological turnover, the TOC values show a gradual decrease which is consistent with an overall decreasing SST trend at the study site observed by Herbert et al. (2016) (Fig.19). Therefore, the decreasing TOC trend may reflect reduced marine productivity during this time as a response to declining SSTs. However, this interpretation remains tentative, as there are also other ways to interpret the decreasing TOC values. Firstly, the overall low TOC values (0.13–0.63 wt.%) need to be treated with care, as the TOC record from ODP Site 907 Hole C yields values of a similarly low range (0.11–0.84 wt.%), which may have resulted from diagenetic affects (Hyun and Kim, 1999). Secondly, changes in sedimentation rates may also influence the preservation of TOC (Meyers, 1997), however, the age model, based on linear interpolation (see Material and Methods chapter), does not allow the resolution of this in more detail. Finally, decreasing TOC values may also reflect increased oxidation of organic carbon associated with enhanced ventilation of bottom waters (Meyers, 1997). Notwithstanding, if the TOC decrease between ~11 to 10.6 Ma indeed reflects changes in productivity related to the decreasing surface temperatures (Herbert et al., 2016), it may suggest the increased influence of an East Greenland Current precursor, transporting cold and fresh waters from the Arctic Ocean into the Iceland Sea. This is supported by a calcareous nannofossil record from ODP Site 918 indicating the initial flow of the East Greenland Current through the Denmark Strait at around 12 Ma (Wei, 1998). It is also supported by indications of improved water mass exchange in the Fram Strait around 11 Ma, and cooling after 10.5 Ma, as inferred from increased bulk accumulation rates and clay mineral assemblages at ODP Site 909 (Wolf-Welling et al., 1996, Winkler et al., 2002).

An increase in $CaCO_3$ has been observed after 10.6 Ma in the Hole 907A record (Fig.19). Increasing $CaCO_3$ contents in Norwegian-Greenland Sea sediments have been interpreted as an enhanced influence of Atlantic waters (Bohrmann et al., 1990). However, carbonate values are generally low (0.06–0.53 wt.%) at ODP Site 907, and do not show any clear trends throughout the studied interval, except for the significant increase at ~10.6 Ma. This increase coincides with a temporary (~150 kyr) increase in TOC and SSTs (Fig.19, Herbert et al., 2016) just prior to the biological turnover event at ~10.4 Ma, which may suggest influence of warmer Atlantic waters. The preservation of carbonate depends on water depth and ocean chemistry (Bohrmann et al., 1990), thus during times of increased overturning, lowering of the lysocline could explain increased carbonate preservation, which might indicate enhanced ventilation of bottom waters after 10.6 Ma. However, the prominent increase in $CaCO_3$ occurs right at the transition between core 14H and 13H, thus drilling disturbance at this level may be partly responsible for the sudden increase observed. However, interpretation of the Hole 907A $CaCO_3$ record remain speculative and needs further support from other proxy records.

4.4 Iceland Sea cooling and ice rafting in response to the Mi-6 event

The Miocene events, as described in the introduction, are well-defined cooling events indicated in deep-sea $\delta^{18}O$-records (Miller et al., 1991, Turco et al., 2001, Westerhold et al., 2005), and have mostly been related to ice volume increase on the Antarctic continent (Miller et al., 1991, and references therein). The Mi-6 event is a well-defined cooling event lasting from 10.7 to 10.4 Ma (Turco et al., 2001, Westerhold et al., 2005). The event is interpreted to reflect mostly increased continental ice volume on Antarctica, and subsequent glacioeustatic sea level fall of around ~50 meters (John et al., 2004, Westerhold et al., 2005), related to low-amplitude variations in the 1.2 Ma obliquity cycle of the Earth (Turco et al., 2001).

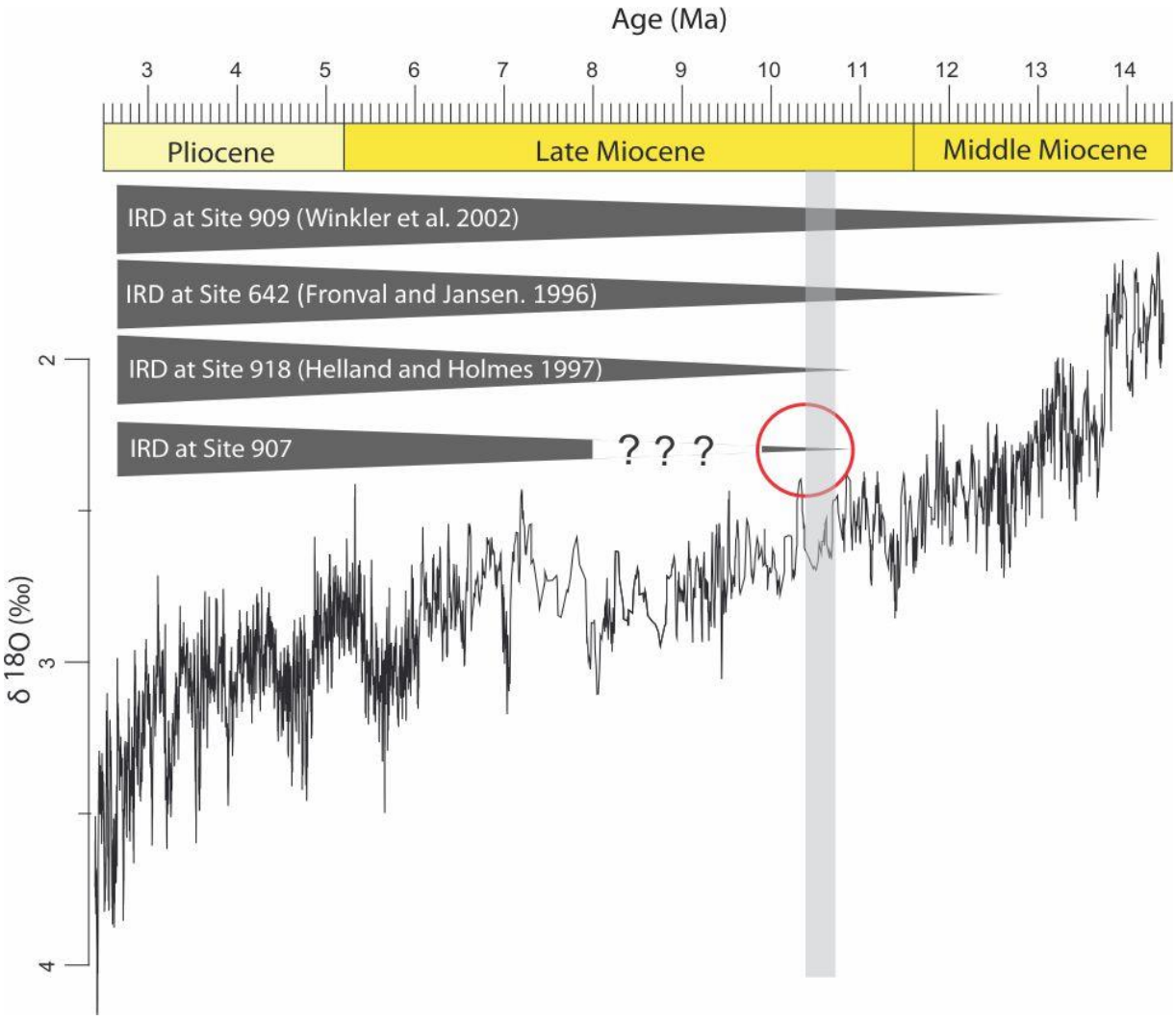

Figure 21: Modified version of Fig.5 (for details see Chapter 1.2.4), highlighting (red circle) the extension of the IRD record at ODP Hole 907A from 8 Ma (Fronval and Jansen, 1996). back the interval between 11 to 9.98 Ma (this study).The extended IRD record coincides with the suggested timing of the Mi-6 event (grey shaded area, Westerhold et al., 2005). Question marks illustrate the interval at Hole 907A where no information on IRD exists yet (9.98–8 Ma) (Figure courtesy of M. Schreck, modified for this thesis).

North Atlantic Ocean Site 982 reveals heavier $\delta^{18}O$-values around 10.55 and 10.4 Ma (Andersson and Jansen, 2003), likely corresponding to the Mi-6 event. The Mi-6 event occurs around the time when a proto-EGC strengthening is suggested by Wei (1998), and increased coarse fraction is observed at ODP Site 909 (~10.5 Ma, Wolf-Welling et al., 1996). Cooling in the Fram Strait is also indicated by changes in the clay mineral assemblage, which have been relate to the Mi-6 event (Winkler et al., 2002). Nonetheless, discrepancies and uncertainties in age models and due to low-resolution proxy records complicates identification of short-term climatic events across different records. The analyzed interval from ODP Hole 907A, however, has a well-constrained age model (Fig. 7, Channell et al., 1999, Schreck et al., 2012) and high-resolution sampling interval (~20 kyr, see Material and Methods Chapter), which allows unambiguous identification of potentially intensified ice rafting related to the global Mi-6 cooling event. A coarsening of the bulk grain-size assemblage and a maxima in quartz abundance occurring contemporaneously with the biological turnover at ODP Site 907, possibly indicate cooling and intensified ice rafting at ~10.4 Ma (Figs. 9 and 19, for details see Chapter 4.3). The timing of these significant changes correspond favorably to the timing for the Mi-6 event (10.7–10.4 Ma, Westerhold et al., 2005), and suggests a response of the high northern latitudes to this globally recognized cooling event.

5 Conclusions

The main objectives of this thesis were to find evidence of ice rafting in the Iceland Sea potentially associated with the global Mi-6 cooling event, and to possibly differentiate the mode for IRD transport as iceberg or sea ice rafted. To address these research objectives, sediments with excellent age-control from ODP Hole 907A have been studied in the time interval from 11–9.98 Ma at ~ 20-kyr resolution using sedimentological and geochemical analysis. The results of this analysis have been discussed within the regional and global perspective of Late Miocene paleoenvironmental evolution.

The common occurrence of terrigenous material in the >125 μm sediment fraction from ODP Site 907 is interpreted as IRD, and suggests continuous ice rafting in the Iceland Sea from 11 Ma to 9.98 Ma. Thus, this thesis extends the Late Miocene IRD-record of Fronval and Jansen (1996) from ODP Site 907 from ~8 Ma to 11 Ma (Fig.21).

Quartz grain surface textures, analyzed with scanning electron microscopy, suggests glacial entrainment prior to deposition, therefore indicating iceberg transport of terrigenous sediment to the Iceland Sea. Transport by icebergs rather than sea ice is favored by warmer sea surface temperatures indicated in the Iceland Sea, and supported by a contemporaneous sea surface temperature decline (Herbert et al., 2016). In turn, the occurrence of iceberg-transported material between 11–10 Ma at the study site suggests small-scale glaciers large enough to reach sea level since at least the early Late Miocene. Late Miocene cooling and possible glaciers forming on Greenland is supported by the occurrences of IRD at 11 Ma off southeast Greenland (Helland and Holmes, 1997). As well as, indications for intensified water exchange at the Fram Strait (Winkler et al., 2002) and onset of the proto-East Greenland Current exporting cooler surface waters to the south (Wei, 1998).

Significant changes are observed in the coarse fraction record of ODP Site 907 at ~10.4 Ma, interpreted as a cooling response in the Iceland Sea to the globally recognized Mi-6 event. An increase in coarse fraction wt.% (> 63 μm) and concomitant maxima in quartz grain abundance suggests intensified ice rafting at that time. This corresponds to an apparent biological turnover event characterized by a significant decrease in the biogenic components of the coarse fraction observed in this study, and also to similar events observed in other micropaleontological studies from ODP Site 907 (Stabell and Koç, 1996, Schreck et al., 2013). The evidence obtained during this thesis from ODP Site 907 in the Iceland Sea suggests a direct response of the high northern latitudes to the global Mi-6. However, additional data from other records in the Norwegian-Greenland Sea are necessary to further confirm the findings of this thesis and to better understand the implications of the Mi-6 events, and potentially other Mi-events in high northern latitudes.

6 Future Work

Although this study has provided further evidence of Late Miocene cooling and extended the IRD record in the Iceland Sea beyond 8 Ma, there is certainly potential for expanded studies of Late Miocene climate at high northern latitudes. Paleoclimate reconstructions could be improved both in regards to methods used in this study and also by analysis of sediments beyond the study interval of this thesis.

Visual inspection of the sediment during this study revealed abundance of ash, siliceous biogenic components and aggregates. In terms of the bulk grain size analysis using coulter counter, this yielded an overrepresentation of the coarse fraction. Removal of ash and biogenic components prior to grain size distribution analysis would improve its accuracy. The following methods as suggested by Krissek (1999) are proposed: 1. Dissolution of biogenic opal to minimise the bias of biosiliceous components. 2. Density separation using heavy liquids, e.g. sodium polytungstate, to separate the very abundant ash from terrigenous material. Since there are both abundant biogenic components and ash, a combination of these two methods should be preferred.

Extraction of IRD using heavy liquid separation, would allow calculation of mass accumulation rates (MAR) in order to determine the depositional rate of IRD independent of ash influence. Since the input of individual components may change over time, the variable input of a major sediment component might mask the fluctuations in accumulation rate of a minor component. By determining variations in the accumulation rate of IRD components over time, periods of increased ice rafting could be verified, and as discussed in this thesis, related to the Mi-6 event. Methodology for calculating the MAR of individual sediment components is described by Krissek (1999).

Furthermore, calculating the MAR of ash may provide information about the frequency of volcanic eruptions during the Late Miocene. Which has been done previously to compare relationships between volcanic eruptions and ice rafting events (e.g. Prueher and Rea, 2001). Characterization of the temporal variation of volcanic activity would complement the existing study of volcanic ashes at ODP Site 907 by (Werner et al., 1993).

The fine fraction (<63 μm) of the sediment was preserved during sieving for potential clay mineralogy and provenance study. Clay mineral assemblages can be used to assess provenance of fine fraction sediments and thus potential transport pathways (e.g. ocean currents, iceberg and sea ice drift trajectories), as well as weathering conditions on the circum-Arctic continents (e.g. Winkler et al., 2002). At ODP Site 907 clay mineral analysis may be used to further characterize intensified ice rafting associated with the Mi-6 event, as increased proportions of illite and chlorite

clay minerals are usually interpreted as enhanced physical weathering on continents, associated with cold and dry conditions (Ehrmann et al., 1992).

The IRD observed at ODP Site 907 during this study has been related to small-scale glaciation on Greenland. A method to provide more detailed information on the provenance of IRD is Fe-oxide analysis (e.g. Darby, 2014). If Fe-oxide minerals are present in the coarse fraction, these can be analysed for trace minerals and subsequently matched to potential source areas. This has been proven successful in distinguishing provenance of Miocene IRD in the Arctic Ocean (Darby, 2014), and Eocene to Oligocene IRD at ODP Site 913 in the Greenland Sea (Tripati and Darby, 2018).

As the sediments from ODP Site 907 analysed during this study contain benthic calcareous foraminifera, $\delta^{18}O$ -analysis may be conducted to further support evidence for the Mi-6 event in the Iceland Sea. Bottom water cooling is observed in relation to the Mi-6 in the North Atlantic (Andersson and Jansen, 2003). Thus bottom water-cooling may also be expected in the Iceland Sea.

Although this study extended the IRD record at Site 907 from 8 Ma back to the interval between 11–10 Ma, it still leaves a 2 million-years gap for the interval between 8 and 10 Ma (Fig.21). Increased ice rafting is observed around 9 Ma at several sites in the Norwegian-Greenland Sea (e.g. Winkler et al., 2002, Fronval and Jansen, 1996), which may be related to the Mi-7 event (9.45 Ma, Miller et al., 1991). Ultimately, the initiation of ice rafting in the Iceland Sea is still uncertain since the IRD record is continuous only from 11 to 9.98 Ma, which suggests onset of ice rafting prior to 11 Ma. Indeed, IRD is observed back to 12.6 Ma at the Vøring Plateau ODP Site 642 (Fronval and Jansen, 1996) and in the Fram Strait ODP Site 909 at least since 14 Ma (Wolf-Welling et al., 1996). Hence, ice rafting may also have commenced earlier than presently known at ODP Site 907 (Fig.21).

Works cited

ABELS, H., HILGEN, F., KRIJGSMAN, W., KRUK, R., RAFFI, I., TURCO, E. & ZACHARIASSE, W. 2005. Long - period orbital control on middle Miocene global cooling: Integrated stratigraphy and astronomical tuning of the Blue Clay Formation on Malta. *Paleoceanography,* 20.

ANDERSON, J. B. 1999. *Antarctic marine geology*, Cambridge University Press.

ANDERSSON, C. & JANSEN, E. 2003. A Miocene (8–12 Ma) intermediate water benthic stable isotope record from the northeastern Atlantic, ODP Site 982. *Paleoceanography,* 18.

BERGGREN, W. A. 1972. Late Pliocene-Pleistocene glaciation. *Initial Reports of the Deep Sea Drilling Project,* 12**,** 953.

BLINDHEIM, J. & ØSTERHUS, S. 2005. The Nordic Seas, main oceanographic features. *The Nordic seas: an integrated perspective***,** 11-37.

BOHRMANN, G., HENRICH, R. & THIEDE, J. 1990. Miocene to Quaternary paleoceanography in the northern North Atlantic: Variability in carbonate and biogenic opal accumulation. *Geological history of the polar oceans: Arctic versus Antarctic.* Springer.

BOND, G., HEINRICH, H., BROECKER, W., LABEYRIE, L., MCMANUS, J., ANDREWS, J., HUON, S., JANTSCHIK, R., CLASEN, S. & SIMET, C. 1992. Evidence for massive discharges of icebergs into the North Atlantic ocean during the last glacial period. *Nature,* 360**,** 245.

BRADLEY, R. S. 1999. *Paleoclimatology: reconstructing climates of the Quaternary*, Elsevier.

BROECKER, W. S. 1991. The great ocean conveyor. *Oceanography,* 4**,** 79-89.

BRUCH, A., UTESCHER, T., MOSBRUGGER, V., GABRIELYAN, I. & IVANOV, D. 2006. Late Miocene climate in the circum-Alpine realm—a quantitative analysis of terrestrial palaeofloras. *Palaeogeography, Palaeoclimatology, Palaeoecology,* 238**,** 270-280.

BUTZIN, M., LOHMANN, G. & BICKERT, T. 2011. Miocene ocean circulation inferred from marine carbon cycle modeling combined with benthic isotope records. *Paleoceanography,* 26.

CHANNELL, J., AMIGO, A. E., FRONVAL, T., RACK, F. & LEHMAN, B. Magnetic stratigraphy at Sites 907 and 985 in the Norwegian–Greenland Sea and a revision of the Site 907 composite section. Proceedings of the Ocean Drilling Program, Scientific Results, 1999. 131-148.

CLOTTEN, C., STEIN, R., FAHL, K. & DE SCHEPPER, S. 2018. Seasonal sea ice cover during the warm Pliocene: Evidence from the Iceland Sea (ODP Site 907). *Earth and Planetary Science Letters,* 481**,** 61-72.

COHEN, J., SCREEN, J. A., FURTADO, J. C., BARLOW, M., WHITTLESTON, D., COUMOU, D., FRANCIS, J., DETHLOFF, K., ENTEKHABI, D. & OVERLAND, J. 2014. Recent Arctic amplification and extreme mid-latitude weather. *Nature geoscience,* 7**,** 627.

DARBY, D. A. 2008. Arctic perennial ice cover over the last 14 million years. *Paleoceanography,* 23.

DARBY, D. A. 2014. Ephemeral formation of perennial sea ice in the Arctic Ocean during the middle Eocene. *Nature Geoscience,* 7**,** 210-213.

DE SCHEPPER, S., GIBBARD, P. L., SALZMANN, U. & EHLERS, J. 2014. A global synthesis of the marine and terrestrial evidence for glaciation during the Pliocene Epoch. *Earth-Science Reviews,* 135**,** 83-102.

DECONTO, R., POLLARD, D. & HARWOOD, D. 2007. Sea ice feedback and Cenozoic evolution of Antarctic climate and ice sheets. *Paleoceanography,* 22.

DROXLER, A. W., BURKE, K., CUNNINGHAM, A. D., HINE, A., ROSENCRANTZ, E., DUNCAN, D. S., HALLOCK, P. & ROBINSON, E. 1998. Caribbean constraints on circulation between Atlantic and Pacific Oceans over the past 40 million years. *OXFORD MONOGRAPHS ON GEOLOGY AND GEOPHYSICS,* 39**,** 169-191.

EHRMANN, W. U., MELLES, M., KUHN, G. & GROBE, H. 1992. Significance of clay mineral assemblages in the Antarctic Ocean. *Marine Geology,* 107**,** 249-273.

ELDRETT, J. S., HARDING, I. C., WILSON, P. A., BUTLER, E. & ROBERTS, A. P. 2007. Continental ice in Greenland during the Eocene and Oligocene. *Nature,* 446**,** 176.

ENGEN, Ø., FALEIDE, J. I. & DYRENG, T. K. 2008. Opening of the Fram Strait gateway: A review of plate tectonic constraints. *Tectonophysics,* 450**,** 51-69.

FALEIDE, J. I., TSIKALAS, F., BREIVIK, A. J., MJELDE, R., RITZMANN, O., ENGEN, O., WILSON, J. & ELDHOLM, O. 2008. Structure and evolution of the continental margin off Norway and the Barents Sea. *Episodes,* 31**,** 82-91.

FISHER, R. V. 1961. Proposed classification of volcaniclastic sediments and rocks. *Geological Society of America Bulletin,* 72**,** 1409-1414.

FLOWER, B. P. & KENNETT, J. P. 1994. The middle Miocene climatic transition: East Antarctic ice sheet development, deep ocean circulation and global carbon cycling. *Palaeogeography, palaeoclimatology, palaeoecology,* 108**,** 537-555.

FRONVAL, T. & JANSEN, E. Late Neogene paleoclimates and paleoceanography in the Iceland-Norwegian Sea: evidence from the Iceland and Vøring Plateaus. Proceedings of the Ocean Drilling Program. Scientific Results, 1996. Ocean Drilling Program, 455-468.

GILBERT, R. 1990. Rafting in glacimarine environments. *Geological Society, London, Special Publications,* 53**,** 105-120.

GRADSTEIN, F. M., OGG, J. G., SCHMITZ, M. & OGG, G. 2012. *The geologic time scale 2012*, elsevier.

HANAN, B. B. & SCHILLING, J.-G. 1997. The dynamic evolution of the Iceland mantle plume: the lead isotope perspective. *Earth and Planetary Science Letters,* 151**,** 43-60.

HANSEN, B. & ØSTERHUS, S. 2000. North atlantic–nordic seas exchanges. *Progress in Oceanography,* 45**,** 109-208.

HANSEN, B., ØSTERHUS, S., TURRELL, W. R., JÓNSSON, S., VALDIMARSSON, H., HÁTÚN, H. & OLSEN, S. M. 2008. The inflow of Atlantic water, heat, and salt to the nordic seas across the Greenland–Scotland ridge. *Arctic–Subarctic Ocean Fluxes.* Springer.

HELLAND, P. & HOLMES, M. A. 1997. Surface textural analysis of quartz sand grains from ODP Site 918 off the southeast coast of Greenland suggests glaciation of southern Greenland at 11 Ma. *Palaeogeography, Palaeoclimatology, Palaeoecology,* 135**,** 109-121.

HENRICH, R., WOLF, T., BOHRMANN, G. & THIEDE, J. Cenozoic paleoclimatic and paleoceanographic changes in the northern hemisphere revealed by variability of coarse-fraction composition in sediments from the V ring Plateau-ODP Leg 104 drill sites. Proc ODP, Sci Results, 1989. 75-188.

HERBERT, T. D., LAWRENCE, K. T., TZANOVA, A., PETERSON, L. C., CABALLERO-GILL, R. & KELLY, C. S. 2016. Late Miocene global cooling and the rise of modern ecosystems. *Nature Geoscience,* 9**,** 843.

HILGEN, F., LOURENS, L., VAN DAM, J. A., BEU, A., BOYES, A., COOPER, R., KRIJGSMAN, W., OGG, J., PILLER, W. & WILSON, D. 2012. The neogene period. *The geologic time scale.* Elsevier.

HUBER, R., MEGGERS, H., BAUMANN, K.-H. & HENRICH, R. 2000. Recent and Pleistocene carbonate dissolution in sediments of the Norwegian–Greenland Sea. *Marine Geology,* 165**,** 123-136.

HUYBRECHTS, P., GREGORY, J., JANSSENS, I. & WILD, M. 2004. Modelling Antarctic and Greenland volume changes during the 20th and 21st centuries forced by GCM time slice integrations. *Global and Planetary Change,* 42**,** 83-105.

HYUN, S. & KIM, S.-R. 1999. Geochemical study for provenance and paleoceanography on ODP Site 907 sediments of the North Atlantic Ocean. *Geosciences Journal,* 3**,** 95-106.

JAKOBSSON, M., BACKMAN, J., RUDELS, B., NYCANDER, J., FRANK, M., MAYER, L., JOKAT, W., SANGIORGI, F., O'REGAN, M. & BRINKHUIS, H. 2007. The early Miocene onset of a ventilated circulation regime in the Arctic Ocean. *Nature,* 447**,** 986-990.

JANSEN, E., FRONVAL, T., RACK, F. & CHANNELL, J. E. 2000. Pliocene - Pleistocene ice rafting history and cyclicity in the Nordic Seas during the last 3.5 Myr. *Paleoceanography,* 15**,** 709-721.

JANSEN, E. & SJØHOLM, J. 1991. Reconstruction of glaciation over the past 6 Myr from ice-borne deposits in the Norwegian Sea. *Nature,* 349**,** 600.

JAPSEN, P., BONOW, J. M., GREEN, P. F., CHALMERS, J. A. & LIDMAR-BERGSTRÖM, K. 2006. Elevated, passive continental margins: Long-term highs or Neogene uplifts? New evidence from West Greenland. *Earth and Planetary Science Letters,* 248**,** 330-339.

JOHN, C. M., KARNER, G. D. & MUTTI, M. 2004. δ18O and Marion Plateau backstripping: combining two approaches to constrain late middle Miocene eustatic amplitude. *Geology,* 32**,** 829-832.

KATZ, M. E., MILLER, K. G., WRIGHT, J. D., WADE, B. S., BROWNING, J. V., CRAMER, B. S. & ROSENTHAL, Y. 2008. Stepwise transition from the Eocene greenhouse to the Oligocene icehouse. *Nature Geoscience,* 1**,** 329.

KLEIVEN, H. F., JANSEN, E., FRONVAL, T. & SMITH, T. 2002. Intensification of Northern Hemisphere glaciations in the circum Atlantic region (3.5–2.4 Ma)–ice-rafted detritus evidence. *Palaeogeography, Palaeoclimatology, Palaeoecology,* 184**,** 213-223.

KNIES, J. & GAINA, C. 2008. Middle Miocene ice sheet expansion in the Arctic: Views from the Barents Sea. *Geochemistry, Geophysics, Geosystems,* 9.

KNIES, J., HALD, M., EBBESEN, H., MANN, U. & VOGT, C. 2003. A deglacial–middle Holocene record of biogenic sedimentation and paleoproductivity changes from the northern Norwegian continental shelf. *Paleoceanography,* 18.

KODAIRA, S., MJELDE, R., GUNNARSSON, K., SHIOBARA, H. & SHIMAMURA, H. 1998. Evolution of oceanic crust on the Kolbeinsey Ridge, north of Iceland, over the past 22 Myr. *TERRA NOVA-OXFORD-,* 10**,** 27-31.

KRISSEK, L. A. 1999. 14. Data Report: Mass accumulation Rates and Composition of Neogene Ice-Rafted Debris, Site 918, Irminger Basin. *Proceedings of the Ocean Drilling Program, Scientific Results Vol. 163.* College Station, TX.

KRYLOV, A. A., ANDREEVA, I. A., VOGT, C., BACKMAN, J., KRUPSKAYA, V. V., GRIKUROV, G. E., MORAN, K. & SHOJI, H. 2008. A shift in heavy and clay mineral provenance indicates a middle Miocene onset of a perennial sea ice cover in the Arctic Ocean. *Paleoceanography,* 23.

LOURENS, L. & HILGEN, F. 1997. Long-periodic variations in the Earth's obliquity and their relation to third-order eustatic cycles and late Neogene glaciations. *Quaternary International,* 40**,** 43-52.

MCCAVE, I., HALL, I. R. & BIANCHI, G. G. 2006. Laser vs. settling velocity differences in silt grainsize measurements: estimation of palaeocurrent vigour. *Sedimentology,* 53**,** 919-928.

MERICO, A., TYRRELL, T. & WILSON, P. A. 2008. Eocene/Oligocene ocean de-acidification linked to Antarctic glaciation by sea-level fall. *Nature,* 452**,** 979.

MEYERS, P. A. 1997. Organic geochemical proxies of paleoceanographic, paleolimnologic, and paleoclimatic processes. *Organic geochemistry,* 27**,** 213-250.

MILLER, K. G., WRIGHT, J. D. & FAIRBANKS, R. G. 1991. Unlocking the ice house: Oligocene - Miocene oxygen isotopes, eustasy, and margin erosion. *Journal of Geophysical Research: Solid Earth,* 96**,** 6829-6848.

MILLIMAN, J. D. 1993. Production and accumulation of calcium carbonate in the ocean: budget of a nonsteady state. *Global Biogeochemical Cycles,* 7**,** 927-957.

MYHRE, A., THIEDE, J. & FIRTH, J. 1. North Atlantic-Arctic gateways. Proceedings of the Ocean Drilling Program, Initial Reports, 1995. 57-111.

NISANCIOGLU, K. H., RAYMO, M. E. & STONE, P. H. 2003. Reorganization of Miocene deep water circulation in response to the shoaling of the Central American Seaway. *Paleoceanography,* 18.

NÜRNBERG, D., WOLLENBURG, I., DETHLEFF, D., EICKEN, H., KASSENS, H., LETZIG, T., REIMNITZ, E. & THIEDE, J. 1994. Sediments in Arctic sea ice: implications for entrainment, transport and release. *Marine Geology,* 119**,** 185-214.

POORE, H., SAMWORTH, R., WHITE, N., JONES, S. & MCCAVE, I. 2006. Neogene overflow of northern component water at the Greenland - Scotland Ridge. *Geochemistry, Geophysics, Geosystems,* 7.

PORTER, J. J. 1962. Electron microscopy of sand surface texture. *Journal of Sedimentary Research,* 32.

PRUEHER, L. M. & REA, D. K. 2001. Volcanic triggering of late Pliocene glaciation: Evidence from the flux of volcanic glass and ice-rafted debris to the North Pacific Ocean. *Palaeogeography, Palaeoclimatology, Palaeoecology,* 173**,** 215-230.

RAHMSTORF, S. 2002. Ocean circulation and climate during the past 120,000 years. *Nature,* 419**,** 207.

RAYMO, M. 1994. The initiation of Northern Hemisphere glaciation. *Annual Review of Earth and Planetary Sciences,* 22**,** 353-383.

REIMNITZ, E., KEMPEMA, E. & BARNES, P. 1987. Anchor ice, seabed freezing, and sediment dynamics in shallow Arctic seas. *Journal of Geophysical Research: Oceans,* 92**,** 14671-14678.

REIMNITZ, E., MCCORMICK, M., MCDOUGALL, K. & BROUWERS, E. 1993. Sediment export by ice rafting from a coastal polynya, Arctic Alaska, USA. *Arctic and Alpine Research***,** 83-98.

RUDELS, B., BJÖRK, G., NILSSON, J., WINSOR, P., LAKE, I. & NOHR, C. 2005. The interaction between waters from the Arctic Ocean and the Nordic Seas north of Fram Strait and along the East Greenland Current: results from the Arctic Ocean-02 Oden expedition. *Journal of Marine Systems,* 55**,** 1-30.

RUDELS, B., FAHRBACH, E., MEINCKE, J., BUDÉUS, G. & ERIKSSON, P. 2002. The East Greenland Current and its contribution to the Denmark Strait overflow. *ICES Journal of Marine Science,* 59**,** 1133-1154.

SCHRECK, M., MATTHIESSEN, J. & HEAD, M. J. 2012. A magnetostratigraphic calibration of Middle Miocene through Pliocene dinoflagellate cyst and acritarch events in the Iceland Sea (Ocean Drilling Program Hole 907A). *Review of Palaeobotany and Palynology,* 187**,** 66-94.

SCHRECK, M., MEHEUST, M., STEIN, R. & MATTHIESSEN, J. 2013. Response of marine palynomorphs to Neogene climate cooling in the Iceland Sea (ODP Hole 907A). *Marine Micropaleontology,* 101**,** 49-67.

SCHUUR, E. A., BOCKHEIM, J., CANADELL, J. G., EUSKIRCHEN, E., FIELD, C. B., GORYACHKIN, S. V., HAGEMANN, S., KUHRY, P., LAFLEUR, P. M. & LEE, H. 2008. Vulnerability of permafrost carbon to climate change: Implications for the global carbon cycle. *AIBS Bulletin,* 58**,** 701-714.

SEKI, O., FOSTER, G. L., SCHMIDT, D. N., MACKENSEN, A., KAWAMURA, K. & PANCOST, R. D. 2010. Alkenone and boron-based Pliocene pCO 2 records. *Earth and Planetary Science Letters,* 292**,** 201-211.

SHEVENELL, A. E., KENNETT, J. P. & LEA, D. W. 2004. Middle Miocene southern ocean cooling and Antarctic cryosphere expansion. *Science,* 305**,** 1766-1770.

SHIPBOARD SCIENTIFIC PARTY 1995. Site 907. *In:* MYHRE, A. M., THIEDE, J., FIRTH, J.V., ET AL. (ed.) *Proceedings of the Ocean Drilling Program, Inital Reports.* 151, Ocean Drilling Program: Texas A & M University, College Station, Texas.

ST JOHN, K. 2008. Cenozoic ice‐rafting history of the central Arctic Ocean: Terrigenous sands on the Lomonosov Ridge. *Paleoceanography,* 23.

ST JOHN, K., PASSCHIER, S., TANTILLO, B., DARBY, D. & KEARNS, L. 2015. Microfeatures of modern sea-ice-rafted sediment and implications for paleo-sea-ice reconstructions. *Annals of Glaciology,* 56**,** 83-93.

ST.JOHN, K. E. & KRISSEK, L. A. 2002. The late Miocene to Pleistocene ice‐rafting history of southeast Greenland. *Boreas,* 31**,** 28-35.

STABELL, B. & KOÇ, N. Recent to middle Miocene diatom productivity at Site 907, Iceland Plateau. 1996. Ocean Drilling Program.

STEIN, R. 1990. Organic carbon content/sedimentation rate relationship and its paleoenvironmental significance for marine sediments. *Geo-Marine Letters,* 10**,** 37-44.

STICKLEY, C. E., ST JOHN, K., KOÇ, N., JORDAN, R. W., PASSCHIER, S., PEARCE, R. B. & KEARNS, L. E. 2009. Evidence for middle Eocene Arctic sea ice from diatoms and ice-rafted debris. *Nature,* 460**,** 376.

THIEDE, J., JESSEN, C., KNUTZ, P., KUIJPERS, A., MIKKELSEN, N., NØRGAARD-PEDERSEN, N. & SPIELHAGEN, R. F. 2011. Million years of Greenland Ice Sheet history recorded in ocean sediments. *Polarforschung,* 80**,** 141-149.

THIEDE, J. & MYHRE, A. M. 36. The palaeoceanographic history of the North Atlantic–Arctic gateways: synthesis of the Leg 151 drilling results. Proceedings of the Ocean Drilling Program, Scientific Results, 1996. 645-658.

THIEDE, J., WINKLER, A., WOLF-WELLING, T., ELDHOLM, O., MYHRE, A. M., BAUMANN, K.-H., HENRICH, R. & STEIN, R. 1998. Late Cenozoic history of the polar North Atlantic: results from ocean drilling. *Quaternary Science Reviews,* 17**,** 185-208.

THRANE, K. 2002. Relationships between Archaean and Palaeoproterozoic crystalline basement complexes in the southern part of the East Greenland Caledonides: an ion microprobe study. *Precambrian Research,* 113**,** 19-42.

TRIPATI, A. & DARBY, D. 2018. Evidence for ephemeral middle Eocene to early Oligocene Greenland glacial ice and pan-Arctic sea ice. *Nature communications,* 9**,** 1038.

TURCO, E., HILGEN, F., LOURENS, L., SHACKLETON, N. & ZACHARIASSE, W. 2001. Punctuated evolution of global climate cooling during the Late Middle to Early Late Miocene: High‐resolution planktonic foraminiferal and oxygen isotope records from the Mediterranean. *Paleoceanography,* 16**,** 405-423.

VOS, K., VANDENBERGHE, N. & ELSEN, J. 2014. Surface textural analysis of quartz grains by scanning electron microscopy (SEM): From sample preparation to environmental interpretation. *Earth-Science Reviews,* 128**,** 93-104.

WEI, W. 1998. Calcarous Nannofossils from the Southeast Greenland Margin: Biostratigraphy and Paleoceanography. *In:* SAUNDERS, A. D., LARSEN, H.C., WISE, S.W. (ed.) *Proceedings of the Ocean Drilling Program.* College Station, Texas: Ocean Drilling Program.

WENTWORTH, C. K. 1922. A scale of grade and class terms for clastic sediments. *The journal of geology,* 30**,** 377-392.

WERNER, R., WALLRABE-ADAMS, H.-J., LACASSE, C., SCHMINCKE, H.-U. & THIEDE, J. Distribution, chemical composition, and sources of Oligocene to Miocene volcanic ashes from Sites 907,908, and 913. PROCEEDINGS-OCEAN DRILLING PROGRAM SCIENTIFIC RESULTS, 1993. NATIONAL SCIENCE FOUNDATION, 333-350.

WESTERHOLD, T., BICKERT, T. & RÖHL, U. 2005. Middle to late Miocene oxygen isotope stratigraphy of ODP site 1085 (SE Atlantic): new constrains on Miocene climate variability and sea-level fluctuations. *Palaeogeography, Palaeoclimatology, Palaeoecology,* 217**,** 205-222.

WINKLER, A., WOLF-WELLING, T., STATTEGGER, K. & THIEDE, J. 2002. Clay mineral sedimentation in high northern latitude deep-sea basins since the Middle Miocene (ODP Leg 151, NAAG). *International Journal of Earth Sciences,* 91**,** 133-148.

WOLF-WELLING, T. C., CREMER, M., O'CONNELL, S., WINKLER, A. & THIEDE, J. Cenozoic Arctic Gateway paleoclimate variability: indications from changes in coarse-fraction composition. PROCEEDINGS-OCEAN DRILLING PROGRAM SCIENTIFIC RESULTS, 1996. NATIONAL SCIENCE FOUNDATION, 515-568.

WORONKO, B. 2016. Frost weathering versus glacial grinding in the micromorphology of quartz sand grains: Processes and geological implications. *Sedimentary Geology,* 335**,** 103-119.

WRIGHT, J. D. & MILLER, K. G. 45. MIOCENE STABLE ISOTOPE STRATIGRAPHY, SITE 747, KERGUELEN PLATEAU1. Proceedings of the Ocean Drilling Program: Scientific results, 1988. The Program, 855.

WRIGHT, J. D. & MILLER, K. G. 1996. Control of North Atlantic deep water circulation by the Greenland‐Scotland Ridge. *Paleoceanography,* 11**,** 157-170.

WRIGHT, J. D., MILLER, K. G. & FAIRBANKS, R. G. 1992. Early and middle Miocene stable isotopes: implications for deepwater circulation and climate. *Paleoceanography,* 7**,** 357-389.

ZACHOS, J., PAGANI, M., SLOAN, L., THOMAS, E. & BILLUPS, K. 2001. Trends, rhythms, and aberrations in global climate 65 Ma to present. *Science,* 292**,** 686-693.

ZACHOS, J. C., DICKENS, G. R. & ZEEBE, R. E. 2008. An early Cenozoic perspective on greenhouse warming and carbon-cycle dynamics. *Nature,* 451**,** 279.

Appendix

APPENDIX A

Geochemical Data

Sample		Depth (mbsf)	Age (Ma)	TC (wt.%)	TOC (wt%)	IC (wt.%)	CaCO3 (wt.%)
13H1	5-7	111.85	9.986994	0.2615	0.2102	0.0513	0.4275
	34-36	112.14	10.00436	0.2783	0.2535	0.0248	0.206667
	66-68	112.46	10.02353	0.4586	0.4315	0.0271	0.225833
	104-106	112.84	10.04628	0.2983	0.271	0.0273	0.2275
	136-138	113.16	10.06545	0.5281	0.4989	0.0292	0.243333
13H2	20-22	113.5	10.08581	0.4753	0.4391	0.0362	0.301667
	54-56	113.84	10.10617	0.462	0.4257	0.0363	0.3025
	84-86	114.14	10.12414	0.4671	0.4504	0.0167	0.139167
	121,5-123,	114.515	10.1466	0.3348	0.3104	0.0244	0.203333
13H3	6-8	114.86	10.16726	0.2873	0.2642	0.0231	0.1925
	40,5-42,5	115.205	10.18792	0.2648	0.2393	0.0255	0.2125
	76-78	115.56	10.20918	0.4526	0.4333	0.0193	0.160833
	112-114	115.92	10.23074	0.3041	0.273	0.0311	0.259167
	142-144	116.22	10.2487	0.4902	0.4505	0.0397	0.330833
13H4	28-30	116.58	10.27026	0.5392	0.5096	0.0296	0.246667
	60-62	116.9	10.28943	0.4701	0.4355	0.0346	0.288333
	64-66	116.94	10.29182	0.4784	0.4511	0.0273	0.2275
	100-102	117.3	10.31338	0.4897	0.4452	0.0445	0.370833
	132-134	117.62	10.33255	0.4683	0.439	0.0293	0.244167
13H5	16-18	117.96	10.35291	0.3778	0.3391	0.0387	0.3225
	50-52	118.3	10.37327	0.2318	0.209	0.0228	0.19
	84-86	118.64	10.39363	0.1438	0.1268	0.017	0.141667
	117-119	118.97	10.4134	0.2529	0.2347	0.0182	0.151667
	142-144	119.22	10.42837	0.3596	0.3347	0.0249	0.2075
13H6	29-31	119.59	10.45053	0.5225	0.4685	0.054	0.45
	60-62	119.9	10.46909	0.445	0.4026	0.0424	0.353333
	94-96	120.24	10.48945	0.3472	0.3283	0.0189	0.1575
	128-130	120.58	10.50982	0.4599	0.4301	0.0298	0.248333
13H7	12-14	120.92	10.53018	0.429	0.379	0.05	0.416667
	46-48	121.26	10.55054	0.2382	0.2117	0.0265	0.220833
	80-82	121.6	10.5709	0.2996	0.2359	0.0637	0.530833
13H-CC	11-13	121.73	10.57869	0.1937	0.1908	0.0029	0.024167
14H1	34-36	121.64	10.5733	0.1638	0.1572	0.0066	0.055
	65-67	121.95	10.59186	0.207	0.1843	0.0227	0.189167
	101-104	122.31	10.61342	0.2334	0.2153	0.0181	0.150833
	136-138	122.66	10.63438	0.2236	0.2025	0.0211	0.175833
14H2	18-20	122.98	10.65355	0.3141	0.2883	0.0258	0.215
	54-56	123.34	10.67511	0.4066	0.3785	0.0281	0.234167
	91-93	123.71	10.69727	0.4617	0.417	0.0447	0.3725
	122-124	124.02	10.71583	0.3327	0.3171	0.0156	0.13
14H3	6-8	124.36	10.73619	0.423	0.3864	0.0366	0.305
	40-42	124.7	10.75656	0.3541	0.3267	0.0274	0.228333
	72-74	125.02	10.77572	0.4206	0.4004	0.0202	0.168333
	107-109	125.37	10.79668	0.3268	0.3038	0.023	0.191667
	142-144	125.72	10.81764	0.557	0.5326	0.0244	0.203333
14H4	23-25	126.03	10.83621	0.5537	0.5196	0.0341	0.284167
	60-62	126.4	10.85836	0.666	0.6329	0.0331	0.275833
	94-96	126.74	10.87873	0.6381	0.5944	0.0437	0.364167
	122-124	127.02	10.8955	0.4923	0.4606	0.0317	0.264167
14H5	12-14	127.42	10.91945	0.595	0.5441	0.0509	0.424167
	45-47	127.75	10.93921	0.5964	0.5606	0.0358	0.298333
	80-82	128.1	10.96017	0.4887	0.4664	0.0223	0.185833
	114-116	128.44	10.98054	0.558	0.5104	0.0476	0.396667
	146-148	128.76	10.9997	0.5839	0.5534	0.0305	0.254167

APPENDIX B

Sieving Grain Size Distribution*

	Sample	Depth (mbsf)	Age (Ma)	<63 µm (wt.%)	63-125 µm (wt.%)	125-250 µm (wt.%)	250-500 µm (wt.%)	500-1000 µm (wt.%)	1000-2000 µm (wt.%)	>2000 µm (wt.%)
13H1	5-7	111.85	9.986994	87.73419	6.542155	1.326698	0.067916	0.0363	0	0
	34-36	112.14	10.00436	87.57398	5.689176	0.966236	0.080437	0	0	0
	66-68	112.46	10.02353	87.16024	6.549703	1.655786	0.238131	0.025223	0.008902	0
	104-106	112.84	10.04628	82.53262	7.617177	3.749667	3.140479	0.047936	0	0
	136-138	113.16	10.06545	88.863	4.341496	1.396426	0.227002	0.027134	0	0
13H2	20-22	113.5	10.08581	87.06802	4.940081	1.163563	0.108502	0.004049	0	0
	54-56	113.84	10.10617	82.24125	5.19375	5.79375	1.16875	0.025	0.0025	0
	84-86	114.14	10.12414	83.83089	5.690426	3.081761	0.560447	0.022362	0.006988	0
	121.5-123.	114.515	10.1466	83.21718	7.039637	2.501239	0.414533	0.033031	0	0
13H3	6-8	114.86	10.16726	86.29507	4.590135	1.815247	0.159641	0.072646	0	0
	40.5-42.5	115.205	10.18792	87.00509	4.287894	1.576806	0.280773	0.040692	0	0
	76-78	115.56	10.20918	86.8427	5.651024	1.920687	0.317911	0.079974	0.005948	0
	112-114	115.92	10.23074	75.81515	8.798788	9.066667	1.031515	0.038182	0	0
	142-144	116.22	10.2487	82.51535	8.241256	3.353319	0.443255	0.099929	0.003569	0
13H4	28-30	116.58	10.27026	80.08992	8.540464	4.074302	0.37151	0.035021	0	0
	60-62	116.9	10.28943	75.09573	9.424321	3.14489	0.252264	0.063389	0.025873	0.201405
	64-66	116.94	10.29182	78.12077	10.30453	3.47267	0.321707	0.075482	0.063509	0.0363
	100-102	117.3	10.31338	80.19991	9.500704	2.628813	0.20366	0.032848	0	0
	132-134	117.62	10.33255	76.20147	11.55381	4.129238	0.636855	0.047666	0.003931	0
13H5	16-18	117.96	10.35291	67.81811	19.27023	6.648849	1.389755	0.282851	0.060134	0
	50-52	118.3	10.37327	81.58571	6.058824	0.996639	0.259664	0.171429	0.438655	9.043326
	84-86	118.64	10.39363	89.84488	2.425208	0.50554	0.128809	0.018006	0	0
	117-119	118.97	10.4134	89.36495	4.716995	0.647193	0.024279	0.000759	0.004552	0
	142-144	119.22	10.42837	84.54862	9.734862	1.147706	0.136697	0.03578	0	0
13H6	29-31	119.59	10.45053	79.69447	10.93391	4.146262	0.735645	0.04442	0	0
	60-62	119.9	10.46909	80.61053	7.161721	5.227003	0.686202	0.054154	0	0
	94-96	120.24	10.48945	77.92168	11.67931	5.225062	0.515251	0.026381	0	0
	128-130	120.58	10.50982	81.48813	6.701847	3.630607	0.278364	0.01715	0.05409	0
13H7	12-14	120.92	10.53018	81.45874	6.859223	3.699029	0.273058	0.036408	0.012136	0
	46-48	121.26	10.55054	81.34622	11.56327	2.154657	0.217047	0.07645	0.09754	0
	80-82	121.6	10.5709	88.34953	5.684112	0.884112	0.123364	0.057944	0.02243	0
13H-CC	11-13	121.73	10.57869	83.06201	4.678179	1.245683	0.05573	0.039246	0	0
14H1	34-36	121.64	10.5733	84.19467	10.07172	1.047131	0.05123	0.008197	0.018443	0
	65-67	121.95	10.59186	87.88833	5.603622	1.099598	0.168008	0.017103	0	0
	101-104	122.31	10.61342	83.87652	7.470533	2.949486	0.289991	0.011225	0	0
	136-138	122.66	10.63438	86.5759	5.209733	2.089224	0.210892	0.041715	0	0
14H2	18-20	122.98	10.65355	80.74616	8.171192	4.726682	0.188312	0.011216	0	0
	54-56	123.34	10.67511	78.68497	7.361658	3.945078	0.856995	0.333679	0.013472	0
	91-93	123.71	10.69727	84.04404	8.724093	2.32513	0.658031	0.056995	0	0
	122-124	124.02	10.71583	87.14087	3.910714	0.979167	0.22619	0.013889	0	0
14H3	6-8	124.36	10.73619	70.92468	2.679487	0.466346	0.128205	0.075321	0	0
	40-42	124.7	10.75656	86.92999	7.219436	1.056426	0.095089	0.020899	0	0
	72-74	125.02	10.77572	82.94092	9.807976	2.304284	0.082718	0.009601	0.005908	0
	107-109	125.37	10.79668	85.41035	6.335415	2.123996	0.156111	0.008921	0.015165	0
	142-144	125.72	10.81764	85.34524	7.002976	2.728175	0.365079	0.049603	0.003968	0.030445
14H4	23-25	126.03	10.83621	86.62825	7.159445	2.317158	0.119584	0.033795	0.003466	0
	60-62	126.4	10.85836	85.92416	6.249559	2.153439	0.240741	0.0194	0	0
	94-96	126.74	10.87873	85.4	5.489209	1.888489	0.623022	0.015827	0	0
	122-124	127.02	10.8955	63.91502	9.236722	0.74608	0.20435	0.004047	0	0
14H5	12-14	127.42	10.91945	85.02353	6.578547	1.507958	0.177163	0.015225	0.00692	0.54918
	45-47	127.75	10.93921	88.63006	4.144509	0.261767	0.084228	0.007432	0	0
	80-82	128.1	10.96017	82.22642	7.605414	1.509434	0.14356	0.013946	0	0
	114-116	128.44	10.98054	88.90711	5.521327	0.736493	0.092891	0.018957	0	0
	146-148	128.76	10.9997	89.29231	3.094118	0.698643	0.142986	0.00724	0.00543	0

*samples highlighted in yellow were sieved two times

Appendix B

Coulter Counter Grain Size Distribution

Sample		Depth (mbsf)	Age (Ma)	< 3.9 µm (wt.%)	3.9-63 µm (wt.%)	63-125 µm (wt.%)	125-250 µm (wt.%)	250-500 µm (wt.%)	500-1 µm (wt.%)	1-2 µm (wt.%)
13H1	5-7	111.85	9.986994	14.06542	59.825187	16.56709	8.030208	1.480466	0.031619	0
	34-36	112.14	10.00436	25.31957	62.313233	9.438443	2.779038	0.149711	0	0
	66-68	112.46	10.02353	26.11243	58.284833	8.696318	3.834207	2.244731	0.827366	9.88E-05
	104-106	112.84	10.04628	25.23799	56.865537	8.652133	5.285649	3.619496	0.339198	0
	136-138	113.16	10.06545	26.92136	57.222627	10.64547	4.847633	0.362904	0	0
13H2	20-22	113.5	10.08581	24.79897	55.50385	12.77597	6.094194	0.783374	0.043658	0
	54-56	113.84	10.10617	22.03632	49.953823	10.01096	9.853827	7.351349	0.793709	0
	84-86	114.14	10.12414	15.93367	55.687257	16.38215	9.232956	2.389435	0.374525	0
	121,5-123,	114.515	10.1466	21.02288	55.005793	14.52832	7.689726	1.496543	0.256725	0
13H3	6-8	114.86	10.16726	23.75719	59.412283	8.523444	4.516295	2.508141	1.100849	0.181803
	40,5-42,5	115.205	10.18792	19.7572	47.874603	16.39126	9.51674	4.787032	1.673147	0
	76-78	115.56	10.20918	21.10936	59.057947	12.68101	6.445281	0.706426	0	0
	112-114	115.92	10.23074	16.6635	55.999897	13.59132	10.12782	3.459037	0.158425	0
	142-144	116.22	10.2487	20.61724	57.615047	13.46181	6.581054	1.54072	0.184137	0
13H4	28-30	116.58	10.27026	20.90766	49.07638	16.95409	11.33634	1.725539	0	0
	60-62	116.9	10.28943	16.79138	57.29501	13.30627	7.435991	3.502966	1.668384	0
	64-66	116.94	10.29182	20.83862	59.965637	12.85672	5.883232	0.455783	0	0
	100-102	117.3	10.31338	22.06011	55.588363	14.49031	7.184109	0.67713	0	0
	132-134	117.62	10.33255	13.97285	53.42706	19.39043	11.98064	1.229012	0	0
13H5	16-18	117.96	10.35291	15.68018	57.492663	13.77994	8.924348	3.271043	0.782782	0.069035
	50-52	118.3	10.37327	18.70122	68.707397	8.438935	3.667367	0.485072	0	0
	84-86	118.64	10.39363	15.02049	29.889029	4.878531	4.268141	5.076168	12.98558	27.88207
	117-119	118.97	10.4134	23.02053	68.855257	5.644961	2.136257	0.342982	0	0
	142-144	119.22	10.42837	17.60528	63.75095	12.35975	4.272654	1.415179	0.596181	0
13H6	29-31	119.59	10.45053	20.02365	65.11548	9.69323	4.739632	0.428005	0	0
	60-62	119.9	10.46909	21.08985	61.662177	7.62629	4.266818	2.940199	2.411872	0.002796
	94-96	120.24	10.48945	13.30476	54.064947	15.5018	12.66391	4.372571	0.092028	0
	128-130	120.58	10.50982	19.89802	59.361327	10.76456	6.696273	3.009038	0.270786	0
13H7	12-14	120.92	10.53018	20.69104	58.871993	9.123903	7.080839	3.968227	0.263978	0
	46-48	121.26	10.55054	16.1291	65.663343	12.78591	5.120474	0.301165	0	0
	80-82	121.6	10.5709	19.00284	67.66546	8.360522	3.510235	1.00554	0.455405	0
13H-CC	11-13	121.73	10.57869	17.29818	61.425083	13.06144	5.257354	1.67423	1.071324	0.212403
14H1	34-36	121.64	10.5733	15.33841	63.592617	16.31904	4.749157	0.000784	0	0
	65-67	121.95	10.59186	17.80799	64.573233	10.52972	5.306639	1.632735	0.149673	0
	101-104	122.31	10.61342	15.47526	61.429907	14.77027	7.339155	0.985419	0	0
	136-138	122.66	10.63438	17.79715	63.185213	9.138808	4.92599	2.662126	2.288973	0.00172
14H2	18-20	122.98	10.65355	14.26617	61.017237	14.76627	8.707395	1.242919	0	0
	54-56	123.34	10.67511	18.26004	56.361487	11.30248	7.961618	4.88956	1.224808	0
	91-93	123.71	10.69727	18.44497	59.543287	14.70619	6.626046	0.679503	0	0
	122-124	124.02	10.71583	22.28264	65.27766	7.298229	3.867586	1.127339	0.146536	0
14H3	6-8	124.36	10.73619	29.31247	56.371488	4.290403	2.350812	5.051608	2.622911	0.000331
	40-42	124.7	10.75656	18.66034	62.571107	11.00608	4.998801	2.532583	0.231104	0
	72-74	125.02	10.77572	13.79817	57.329873	18.48316	9.14688	1.201529	0.040378	0
	107-109	125.37	10.79668	16.50382	64.535817	11.68517	6.283832	0.991354	0	0
	142-144	125.72	10.81764	15.57908	58.579083	16.84647	8.090234	0.905145	0	0
14H4	23-25	126.03	10.83621	14.47321	63.161257	13.4493	8.005489	0.910734	0	0
	60-62	126.4	10.85836	19.19567	60.624723	12.81417	6.687776	0.677651	0	0
	94-96	126.74	10.87873	13.72418	53.83313	18.21341	8.425732	5.033519	0.770027	0
	122-124	127.02	10.8955	13.75965	59.304683	21.87617	5.051955	0.007556	0	0
14H5	12-14	127.42	10.91945	21.03657	57.429587	12.39986	7.000195	2.021794	0.111992	0
	45-47	127.75	10.93921	21.50551	63.781853	11.86851	2.76711	0.077018	0	0
	80-82	128.1	10.96017	15.39772	72.57321	9.353442	2.617932	0.057694	0	0
	114-116	128.44	10.98054	19.9393	64.348813	10.46349	4.482434	0.765959	0	0
	146-148	128.76	10.9997	21.66609	59.123383	7.52532	4.858426	5.426978	1.399824	0

APPENDIX C

125-250 µm

Sample		Depth (mbsf)	Age (Ma)	Agglutinated foraminifera (grain %)	Calcareous foraminifera (grain %)	Radiolaria (grain %)	Spicules (grain %)	Quartz (grain %)	Feldspar (grain %)	Biotite (grain %)	Gypsum (grain %)	Unclassified rock fragments (grain %)	Ash (grain %)	Aggregates (grain %)	Oxidized aggregates (grain %)	Unidentified (grain %)
13H1	5-7	111.85	9.986994	0	0	2.2026432	3.964758	0	0	0	0	0	88.54626	5.28634361	0	0
	34-36	112.14	10.00436	0	0	1.5444015	3.088803	2.316602	0	0.19305	0	0.579150579	77.79923	14.4787645	0	0
	66-68	112.46	10.02353	0	0	1.7283951	4.197531	3.45679	0	0	0	0	65.67901	24.9382716	0	0
	104-106	112.84	10.04628	0	0	0.4081633	0.816327	0	0	0	0	0	86.93878	11.8367347	0	0
	136-138	113.16	10.06545	0.199600798	0	2.1956088	3.193613	1.996008	0	0	0	0.199600798	75.4491	15.3692615	0.199600798	1.19760479
13H2	20-22	113.5	10.08581	0	0	22.44898	1.855288	0.742115	0	0	0	0	61.9666	12.6159555	0.371057514	0
	54-56	113.84	10.10617	0	0	4.75	1	0	0	0	0	0	86.75	6	0	1.5
	84-86	114.14	10.12414	0	0	2.2587269	1.64271	0	0	0	0	0	91.58111	4.5174538	0	0
	121,5-123,!	114.515	10.1466	0	0	0.2222222	0.444444	5.555556	0.444444	0.222222	0	4	67.77778	21.3333333	0	0
13H3	6-8	114.86	10.16726	0	0	0.5736138	0.573614	1.912046	0	0	0	0.191204589	76.09943	19.1204589	1.529636711	0
	40,5-42,5	115.205	10.18792	0	0	1.6736402	0	1.464435	0	0	0	0.209205021	50.62762	46.0251046	0	0
	76-78	115.56	10.20918	0.177304965	0	3.5460993	4.432624	0.886525	0.177305	0	0	0.354609929	73.22695	7.9787234	9.219858156	0
	112-114	115.92	10.23074	0	0	0.8237232	0.658979	0.329489	0	0	0	0	89.62109	7.74299835	0.329489292	0.494233937
	142-144	116.22	10.2487	0	0	1.4675052	1.257862	3.354298	0	0	0	0	72.74633	20.5450734	0.628930818	0
13H4	28-30	116.58	10.27026	0	0	0.6833713	0.683371	2.505695	0	0	0	0	89.74943	5.92255125	0.455580866	0
	60-62	116.9	10.28943	0.236966825	0	1.1848341	0.947867	0.473934	0	0	0	0.473933649	84.59716	10.9004739	0	1.184834123
	64-66	116.94	10.29182	0	0	4.296875	0	0.976563	0	0	0.585938	0	88.08594	6.0546875	0	0
	100-102	117.3	10.31338	0	0	4.0441176	1.654412	1.286765	0	0	0	0	68.19853	24.8161765	0	0
	132-134	117.62	10.33255	0	0.226244344	1.3574661	0	1.357466	0	0	0	0	77.82805	19.2307692	0	0
13H5	16-18	117.96	10.35291	0	0	0.8421053	1.052632	3.157895	0	0	0	0	59.57895	34.9473684	0	0.421052632
	50-52	118.3	10.37327	0	0	1.9880716	2.7833	3.976143	0	0	0	1.590457256	84.09543	5.16898608	0	0.397614314
	84-86	118.64	10.39363	0	0	1.25	1	5	0.25	0	0	1.5	21.25	69.5	0.25	0
	117-119	118.97	10.4134	0	0.459770115	12.183908	0.91954	0.91954	0	0	0	0	71.72414	1.37931034	0	12.4137931
	142-144	119.22	10.42837	0	0	7.5213675	4.273504	1.880342	0	0	0	0	56.92308	29.4017094	0	0
13H6	29-31	119.59	10.45053	0.189035917	0	6.9943289	3.969754	0.189036	0	0	0	0.189035917	74.85822	13.2325142	0.189035917	0.189035917
	60-62	119.9	10.46909	0	0	0.7058824	0.470588	0.941176	0	0	0	0	82.35294	14.8235294	0	0.705882353
	94-96	120.24	10.48945	0	0	10.271318	0.775194	0.193798	0	0	0	0	81.20155	6.78294574	0.19379845	0.581395349
	128-130	120.58	10.50982	0.192307692	0	5.9615385	1.730769	0.576923	0	0	0	0	87.88462	3.07692308	0.576923077	0
13H7	12-14	120.92	10.53018	0	0	2.1978022	3.076923	0.21978	0	0	0	0	86.59341	6.59340659	1.318681319	0
	46-48	121.26	10.55054	0	0.208768267	8.3507307	3.966597	1.461378	0	0	0	0	69.93737	16.0751566	0	0
	80-82	121.6	10.5709	0	0	11.637931	12.06897	3.017241	0.215517	0	0	0	67.88793	4.74137931	0	0.431034483
13H-CC	11-13	121.73	10.57869	0	0	0.2247191	0.674157	0.449438	0	0	0	0.224719101	68.76404	29.6629213	0	0
14H1	34-36	121.64	10.5733	0	0.606060606	4.6464646	5.252525	0.808081	0	0	0	0	85.85859	2.42424242	0.404040404	0
	65-67	121.95	10.59186	0.189393939	0.378787879	13.068182	15.5303	1.893939	0	0	0	0	61.36364	6.62878788	0.946969697	0
	101-104	122.31	10.61342	0	0	4.5833333	0.416667	0.416667	0.625	0	0	0	91.25	2.5	0	0.208333333
	136-138	122.66	10.63438	0	0	6.3926941	2.968037	2.054795	0	0	0	0.228310502	74.65753	12.3287671	1.369863014	0
14H2	18-20	122.98	10.65355	0	0.213219616	1.9189765	1.279318	0	0	0	0	0	95.94883	0.63965885	0	0
	54-56	123.34	10.67511	0	0.204918033	1.2295082	1.844262	0.204918	0	0	0	0	90.77869	2.66393443	3.073770492	0
	91-93	123.71	10.69727	0	0.378071834	6.0491493	2.457467	2.646503	0	0	0	0.56710775	73.72401	13.4215501	0.56710775	0.189035917
	122-124	124.02	10.71583	0	0	6.9271758	7.637655	2.486679	0	0	0	0	76.73179	5.5062167	0	0.710479574
14H3	6-8	124.36	10.73619	0	0.211864407	6.5677966	5.084746	3.389831	0	0	0	0.211864407	45.33898	31.3559322	7.838983051	0
	40-42	124.7	10.75656	0	0	3.8961039	2.597403	1.948052	0	0	0	0.324675325	79.54545	11.525974	0	0.162337662
	72-74	125.02	10.77572	0	0.222222222	4.8888889	0	1.777778	0	0.222222	0	0.222222222	86.66667	4.88888889	0.222222222	0.888888889
	107-109	125.37	10.79668	0	0	7.4468085	4.787234	3.014184	0.177305	0	0	0	81.20567	3.0141844	0	0.354609929
	142-144	125.72	10.81764	0.243902439	0	2.9268293	0.487805	1.95122	0	0	0	0	78.78049	9.02439024	6.585365854	0
14H4	23-25	126.03	10.83621	0	0.359066427	3.2315978	0.359066	0.718133	0	0	0	0	86.71454	8.61759425	0	0
	60-62	126.4	10.85836	0.205761317	0	0.4115226	1.234568	1.646091	0.205761	0	0	0	87.86008	8.02469136	0.205761317	0.205761317
	94-96	126.74	10.87873	0	0	0.921659	1.612903	1.843318	0.230415	0	0	0.230414747	91.47465	2.30414747	0.921658986	0.460829493
	122-124	127.02	10.8955	0	0.194931774	3.8986355	1.754386	3.31384	0	0	0	0	87.1345	3.7037037	0	0
14H5	12-14	127.42	10.91945	0	0	8.8659794	4.536082	1.85567	0	0	2.268041	1.030927835	72.78351	6.18556701	2.474226804	0
	45-47	127.75	10.93921	0	0.589390963	12.573674	11.78782	1.768173	0	0	0	0.392927308	48.52652	23.1827112	1.178781925	0
	80-82	128.1	10.96017	0	0.197628458	10.27668	2.371542	2.56917	0	0	0	0	76.87747	7.50988142	0.197628458	0
	114-116	128.44	10.98054	0.198412698	0.396825397	3.7698413	1.388889	3.769841	0.198413	0	0	0	85.9127	0.3968254	3.968253968	0
	146-148	128.76	10.9997	0.173611111	0	0.8680556	1.388889	2.777778	0.173611	0	0	0	63.88889	28.6458333	2.083333333	0

APPENDIX C

250-500 µm

Sample		Depth (mbsf)	Age (Ma)	Agglutinated foraminifera (grain %)	Calcareous foraminifera (grain %)	Radiolaria (grain %)	Spicules (grain %)	Quartz (grain %)	Feldspar (grain %)	Biotite (grain %)	Gypsum (grain %)	Unclassified rock fragments (grain %)	Ash (grain %)	Aggregates (grain %)	Oxidized aggregates (grain %)	Unidentified (grain %)
13H1	5-7	111.85	9.986994	3.896103896	2.597402597	1.298701299	7.792208	12.12121	0	0	0	0.865800866	41.55844	29.43722944	0	0.432900433
	34-36	112.14	10.00436	6.296296296	4.074074074	4.074074074	4.444444	18.88889	0	0	0	0.37037037	29.25926	32.59259259	0	0
	66-68	112.46	10.02353	0.64516129	1.505376344	1.720430108	2.580645	41.93548	0	0	0	1.290322581	14.62366	35.48387097	0.215053763	0
	104-106	112.84	10.04628	0	0	0	0	0.241546	0	0	0	0.241545894	89.61353	8.45410628	0.724637681	0.724637681
	136-138	113.16	10.06545	3.409090909	2.045454545	0.227272727	0.681818	7.045455	0	0	0	0.227272727	48.18182	34.31818182	3.863636364	0
13H2	20-22	113.5	10.08581	3.472222222	1.62037037	0.694444444	2.314815	7.175926	0	0	0	0.231481481	56.94444	22.22222222	5.092592593	0.231481481
	54-56	113.84	10.10617	0	0.448430493	0	0.672646	0	0	0	0	0	87.89238	10.98654709	0	0
	84-86	114.14	10.12414	0.224215247	0.448430493	0	3.139013	0.672646	0	0	0	0	84.75336	9.417040359	1.121076233	0.224215247
	121,5-123,	114.515	10.1466	0	0	0	0.22779	23.46241	0	0	0	1.138952164	11.8451	60.59225513	2.505694761	0.227790433
13H3	6-8	114.86	10.16726	0.477326969	0.238663484	0	0.477327	5.011933	0	0	0	0.238663484	80.19093	13.36515513	0	0
	40,5-42,5	115.205	10.18792	1.219512195	0.487804878	0.487804878	0.487805	11.70732	0	0	0	0.731707317	12.92683	71.95121951	0	0
	76-78	115.56	10.20918	1.154734411	1.847575058	0	0.692841	5.080831	0	0	0	0.230946882	53.57968	13.39491917	24.01847575	0
	112-114	115.92	10.23074	0.389863548	0.584795322	0	0.389864	3.31384	0	0	0	0	74.8538	17.1539961	3.313840156	0
	142-144	116.22	10.2487	1.411764706	0.941176471	0	0.705882	18.11765	0	0	0	0.941176471	28	47.52941176	2.352941176	0
13H4	28-30	116.58	10.27026	1.384083045	0.346020761	0.346020761	0.865052	6.574394	0	0	0	0.173010381	71.10727	15.91695502	3.287197232	0
	60-62	116.9	10.28943	3.178484108	0	0	0.244499	7.579462	0	0.244499	0	0.244498778	69.19315	19.07090465	0	0.244498778
	64-66	116.94	10.29182	1.969365427	1.312910284	0	0.875274	8.752735	0	0	0	0	66.30197	20.78774617	0	0
	100-102	117.3	10.31338	5.197505198	0.831600832	0.415800416	1.871102	13.92931	0	0	0	0.831600832	40.33264	36.59043659	0	0
	132-134	117.62	10.33255	0.686498856	0.686498856	0	2.745995	10.75515	0	0	0	0.228832952	50.80092	34.09610984	0	0
13H5	16-18	117.96	10.35291	0.220264317	0.660792952	0	1.321586	23.56828	0	0	0	0.440528634	31.4978	42.07048458	0	0.220264317
	50-52	118.3	10.37327	0.505050505	0	0	2.525253	42.92929	0	0.757576	0	2.272727273	48.9899	2.02020202	0	0
	84-86	118.64	10.39363	0	0	0	0	13.17365	0	0.299401	0	0.598802395	14.07186	71.55688623	0	0.299401198
	117-119	118.97	10.4134	16.30434783	13.04347826	6.52173913	9.782609	20.65217	0	0	0	0	25	8.695652174	0	0
	142-144	119.22	10.42837	4.597701149	5.172413793	0.287356322	0.574713	15.51724	0	0	0	0.574712644	9.195402	64.08045977	0	0
13H6	29-31	119.59	10.45053	2.059496568	0.457665904	0.228832952	0.457666	0.915332	0	0	0	0.457665904	70.93822	24.48512586	0	0
	60-62	119.9	10.46909	1.372997712	1.14416476	0.228832952	0.457666	2.059497	0	0	0	0.457665904	73.68421	20.36613272	0.228832952	0
	94-96	120.24	10.48945	1.6985138	0.636942675	0.636942675	0	0.849257	0	0	0	0	80.46709	14.64968153	1.061571125	0
	128-130	120.58	10.50982	3.75	2.75	0.25	0	6.75	0	0	0	0.75	82.75	2	1	0
13H7	12-14	120.92	10.53018	1.686746988	2.168674699	0	0.481928	3.13253	0.240964	0	0	0.240963855	73.01205	13.4939759	5.542168675	0
	46-48	121.26	10.55054	9.226932668	8.229426434	9.476309227	24.4389	11.97007	0	0.74813	0	0.748129676	15.71072	19.20199501	0.249376559	0
	80-82	121.6	10.5709	9.142857143	8.571428571	5.714285714	0.571429	14.28571	0	0	0	0	49.14286	12	0	0.571428571
13H-CC	11-13	121.73	10.57869	1.285347044	0.514138817	0	0.257069	4.113111	0	0	0	0	21.07969	72.75064267	0	0
14H1	34-36	121.64	10.5733	9.210526316	8.552631579	3.947368421	5.921053	16.44737	0	0	0	0	26.31579	0	29.60526316	0
	65-67	121.95	10.59186	9.263657957	11.40142518	4.513064133	9.501188	18.76485	0.23753	0	0	0.712589074	30.87886	1.90023753	12.82660333	0
	101-104	122.31	10.61342	2.391304348	2.826086957	0	0.434783	3.043478	0	0	0	0.217391304	89.34783	1.739130435	0	0
	136-138	122.66	10.63438	9.292035398	3.982300885	0	1.769912	22.78761	0	0	0	0.442477876	28.09735	8.628318584	25	0
14H2	18-20	122.98	10.65355	3.472222222	2.083333333	0.462962963	1.157407	1.157407	0	0	0	0	78.93519	12.73148148	0	0
	54-56	123.34	10.67511	2.457002457	0.737100737	0	0	1.719902	0	0	0	1.474201474	74.44717	7.371007371	11.79361179	0
	91-93	123.71	10.69727	3.146067416	0.898876404	1.797752809	0.224719	4.269663	0	0.224719	0	0	64.04494	25.16853933	0.224719101	0
	122-124	124.02	10.71583	2.591792657	2.375809935	0	2.37581	5.831533	0	0	0	0.863930886	82.28942	3.455723542	0	0.215982721
14H3	6-8	124.36	10.73619	6.113537118	4.80349345	0	0.873362	8.296943	0	0	0	0	3.49345	31.87772926	44.54148472	0
	40-42	124.7	10.75656	5.780346821	2.312138728	0.578034682	0.578035	9.82659	0	0	0	0.289017341	18.78613	58.67052023	3.179190751	0
	72-74	125.02	10.77572	8.495145631	3.155339806	1.941747573	4.126214	8.495146	0.242718	0	0	0.72815534	59.2233	7.281553398	6.310679612	0
	107-109	125.37	10.79668	2.360515021	6.43776824	0	2.7897	25.32189	0	0	0	0	56.22318	2.145922747	4.721030043	0
	142-144	125.72	10.81764	3.917050691	0.921658986	0.921658986	1.152074	11.98157	0	0	0	0	69.12442	6.68202765	5.069124424	0.230414747
14H4	23-25	126.03	10.83621	9.359605911	3.694581281	1.97044335	2.216749	21.18227	0	0.246305	0	0.738916256	22.9064	37.43842365	0.246305419	0
	60-62	126.4	10.85836	3.538175047	1.675977654	0.744878957	0.931099	5.400372	0	0	0	0.931098696	58.10056	22.53258845	6.145251397	0
	94-96	126.74	10.87873	0.921658986	0.460829493	0.230414747	0.230415	3.456221	0	0	0	0.460829493	90.553	0.921658986	2.304147465	0.460829493
	122-124	127.02	10.8955	2.669902913	0.485436893	0.242718447	0.485437	7.281553	0.242718	0	0	0.485436893	87.86408	0	0.242718447	0
14H5	12-14	127.42	10.91945	1.45631068	0.970873786	0.970873786	0.728155	17.47573	0	0.242718	0	0.242718447	37.62136	24.51456311	15.53398058	0.242718447
	45-47	127.75	10.93921	3.9408867	2.216748768	2.216748768	7.389163	15.27094	0	0	0	0.492610837	8.128079	57.8817734	2.463054187	0
	80-82	128.1	10.96017	8.258928571	6.473214286	1.5625	6.026786	42.85714	0	0.223214	0	2.232142857	27.45536	4.464285714	0.223214286	0.223214286
	114-116	128.44	10.98054	10	0.869565217	0	9.130435	46.08696	0	0.869565	0	0.869565217	11.73913	0.869565217	19.13043478	0.434782609
	146-148	128.76	10.9997	5.852417303	3.053435115	0	3.562341	22.1374	0.763359	0.508906	0	1.272264631	58.26972	2.544529262	2.03562341	0

APPENDIX C

500-1000 µm

Sample		Depth (mbsf)	Age (Ma)	Agglutinated foraminifera (grain %)	Calcareous foraminifera (grain %)	Radiolaria (grain %)	Spicules (grain %)	Quartz (grain %)	Feldspar (grain %)	Biotite (grain %)	Gypsum (grain %)	Unclassified rock fragments (grain %)	Ash (grain %)	Aggregates (grain %)	Oxidized aggregates (grain %)	Unidentified (grain %)
13H1	5-7	111.85	9.986994	0	0	0	0	0	0	0	0	0	33.33333	66.66666667	0	0
	34-36	112.14	10.00436	0	0	0	0	0	0	0	0	0	0	0	0	0
	66-68	112.46	10.02353	0	0	0	0	12.5	0	0	0	0	12.5	75	0	0
	104-106	112.84	10.04628	0	0	0	0	5.172414	0	0	0	0	68.96552	24.13793103	1.724137931	0
	136-138	113.16	10.06545	0	0	0	0	14.28571	0	0	0	0	14.28571	67.85714286	3.571428571	0
13H2	20-22	113.5	10.08581	0	0	0	0	33.33333	0	0	0	0	66.66667	0	0	0
	54-56	113.84	10.10617	0	0	0	0	2.631579	0	0	0	0	60.52632	34.21052632	2.631578947	0
	84-86	114.14	10.12414	3.703703704	0	0	0	0	0	0	11.11111	0	40.74074	37.03703704	7.407407407	0
	121,5-123,!	114.515	10.1466	0	0	0	0	15.78947	0	0	5.263158	0	21.05263	52.63157895	5.263157895	0
13H3	6-8	114.86	10.16726	0	0	0	0	3.448276	0	0	3.448276	0	93.10345	0	0	0
	40,5-42,5	115.205	10.18792	0	0	0	0	6.976744	0	0	0	0	9.302326	81.39534884	2.325581395	0
	76-78	115.56	10.20918	0	0	0	0	3.174603	0	0	0	0	11.11111	17.46031746	68.25396825	0
	112-114	115.92	10.23074	0	0	0	0	4.651163	0	0	0	2.325581395	4.651163	67.44186047	20.93023256	0
	142-144	116.22	10.2487	1.694915254	0	0	0	25.42373	0	0	0	1.694915254	11.86441	54.23728814	5.084745763	0
13H4	28-30	116.58	10.27026	2.857142857	0	0	0	17.14286	0	0	0	0	34.28571	31.42857143	14.28571429	0
	60-62	116.9	10.28943	2.43902439	0	0	0	12.19512	0	0	0	0	68.29268	14.63414634	2.43902439	0
	64-66	116.94	10.29182	1.538461538	0	0	0	1.538462	0	0	0	0	60	36.92307692	0	0
	100-102	117.3	10.31338	2.941176471	0	0	0	11.76471	0	0	0	0	79.41176	5.882352941	0	0
	132-134	117.62	10.33255	1.818181818	0	0	0	7.272727	0	0	0	0	18.18182	72.72727273	0	0
13H5	16-18	117.96	10.35291	0	0	0	0	7.878788	0	0	0	0	48.48485	42.42424242	1.212121212	0
	50-52	118.3	10.37327	0	0	0	0	10.9589	0	0	0	1.369863014	80.82192	1.369863014	0	5.479452055
	84-86	118.64	10.39363	0	0	0	0	0	0	0	0	0	25	75	0	0
	117-119	118.97	10.4134	0	0	0	0	0	0	0	0	0	100	0	0	0
	142-144	119.22	10.42837	3.125	0	0	0	3.125	0	0	0	0	18.75	75	0	0
13H6	29-31	119.59	10.45053	4.347826087	0	0	0	0	0	0	0	0	30.43478	65.2173913	0	0
	60-62	119.9	10.46909	0	0	0	0	2.777778	0	0	0	0	88.88889	8.333333333	0	0
	94-96	120.24	10.48945	18.18181818	0	0	0	9.090909	0	0	0	0	45.45455	27.27272727	0	0
	128-130	120.58	10.50982	0	0	0	0	33.33333	0	0	0	22.22222222	44.44444	0	0	0
13H7	12-14	120.92	10.53018	10	0	0	0	5	0	0	0	0	25	50	10	0
	46-48	121.26	10.55054	5.882352941	0	0	17.64706	29.41176	0	2.941176	0	0	14.70588	29.41176471	0	0
	80-82	121.6	10.5709	0	0	0	0	0	0	0	0	0	60	40	0	0
13H-CC	11-13	121.73	10.57869	0	0	0	0	4.166667	0	0	0	0	0	95.83333333	0	0
14H1	34-36	121.64	10.5733	100	0	0	0	0	0	0	0	0	0	0	0	0
	65-67	121.95	10.59186	0	0	0	0	33.33333	0	0	0	0	33.33333	0	16.66666667	16.66666667
	101-104	122.31	10.61342	16.66666667	0	0	0	0	0	0	0	0	16.66667	66.66666667	0	0
	136-138	122.66	10.63438	7.142857143	0	0	0	21.42857	0	0	0	7.142857143	14.28571	0	50	0
14H2	18-20	122.98	10.65355	5.882352941	0	0	0	0	0	0	0	0	11.76471	82.35294118	0	0
	54-56	123.34	10.67511	0.724637681	0	0	0	2.173913	0	0	51.44928	0	6.521739	10.86956522	28.26086957	0
	91-93	123.71	10.69727	3.571428571	0	0	0	3.571429	0	0	0	0	32.14286	60.71428571	0	0
	122-124	124.02	10.71583	0	0	0	0	0	0	0	0	0	100	0	0	0
14H3	6-8	124.36	10.73619	0	0	0	0	0	0	0	0	4.545454545	4.545455	18.18181818	72.72727273	0
	40-42	124.7	10.75656	0	0	0	0	18.18182	0	0	0	9.090909091	0	72.72727273	0	0
	72-74	125.02	10.77572	11.11111111	0	0	0	0	0	0	0	0	55.55556	11.11111111	22.22222222	0
	107-109	125.37	10.79668	0	0	0	0	0	0	0	0	0	50	33.33333333	16.66666667	0
	142-144	125.72	10.81764	0	0	0	0	29.41176	0	0	0	0	35.29412	23.52941176	11.76470588	0
14H4	23-25	126.03	10.83621	6.25	0	0	0	31.25	0	0	0	0	31.25	31.25	0	0
	60-62	126.4	10.85836	7.142857143	0	0	0	7.142857	0	0	0	0	50	21.42857143	14.28571429	0
	94-96	126.74	10.87873	0	0	0	0	18.18182	0	0	0	9.090909091	72.72727	0	0	0
	122-124	127.02	10.8955	0	0	0	0	16.66667	0	0	0	0	83.33333	0	0	0
14H5	12-14	127.42	10.91945	0	0	0	0	8.333333	0	0	0	8.333333333	25	16.66666667	41.66666667	0
	45-47	127.75	10.93921	50	0	0	0	0	0	0	0	0	50	0	0	0
	80-82	128.1	10.96017	0	0	0	0	20	0	0	0	0	60	20	0	0
	114-116	128.44	10.98054	0	0	0	0	28.57143	0	0	0	0	28.57143	0	42.85714286	0
	146-148	128.76	10.9997	0	0	0	0	0	0	0	0	0	100	0	0	0

APPENDIX C

1000–2000 µm

Sample		Depth (mbsf)	Age (Ma)	Agglutinated foraminifera (no. Grains)	Calcareous foraminifera (no. Grains)	Radiolaria (no. Grains)	Spicules (no. Grains)	Quartz (no. Grains)	Feldspar (no. Grains)	Biotite (no. Grains)	Gypsum (no. Grains)	Rock Fragments (no. Grains)	Pumice (no. Grains)	Ash (no. Grains)	Aggregates (no. Grains)	Oxidized aggregates (no. Grains)	Unidentified (no. Grains)
13H1	5-7	111.85	9.986994	–	–	–	–	–	–	–	–	–	–	–	–	–	–
	34-36	112.14	10.00436	–	–	–	–	–	–	–	–	–	–	–	–	–	–
	66-68	112.46	10.02353	–	–	–	–	–	–	–	–	–	–	1	–	–	–
	104-106	112.84	10.04628	–	–	–	–	–	–	–	–	–	–	–	–	–	–
	136-138	113.16	10.06545	–	–	–	–	–	–	–	–	–	–	–	–	–	–
13H2	20-22	113.5	10.08581	–	–	–	–	–	–	–	–	–	–	–	–	–	–
	54-56	113.84	10.10617	–	–	–	1	–	–	–	–	–	–	–	–	–	–
	84-86	114.14	10.12414	–	–	–	–	–	–	–	–	–	–	1	–	–	–
	121,5-123,!	114.515	10.1466	–	–	–	–	–	–	–	–	–	–	–	–	–	–
13H3	6-8	114.86	10.16726	–	–	–	–	–	–	–	–	–	–	–	–	–	–
	40,5-42,5	115.205	10.18792	–	–	–	–	–	–	–	–	–	–	–	–	–	–
	76-78	115.56	10.20918	–	–	–	–	–	–	–	–	–	–	1	–	–	–
	112-114	115.92	10.23074	–	–	–	–	–	–	–	–	–	–	–	–	–	–
	142-144	116.22	10.2487	–	–	–	–	–	–	–	–	–	–	1	–	–	–
13H4	28-30	116.58	10.27026	–	–	–	–	–	–	–	–	–	–	–	–	–	–
	60-62	116.9	10.28943	–	–	–	–	–	–	–	–	–	–	2	–	–	–
	64-66	116.94	10.29182	–	–	–	–	–	–	–	–	1	6	3	1	–	–
	100-102	117.3	10.31338	–	–	–	–	–	–	–	–	–	–	1	–	–	–
	132-134	117.62	10.33255	–	–	–	–	–	–	–	–	–	–	–	–	–	–
13H5	16-18	117.96	10.35291	–	–	–	–	–	–	–	–	–	–	4	1	–	–
	50-52	118.3	10.37327	–	–	–	–	–	–	–	–	–	44	–	–	–	1
	84-86	118.64	10.39363	–	–	–	–	–	–	–	–	–	–	–	–	–	–
	117-119	118.97	10.4134	–	–	–	–	–	–	–	–	–	–	1	–	–	–
	142-144	119.22	10.42837	–	–	–	–	–	–	–	–	–	–	–	–	–	–
13H6	29-31	119.59	10.45053	–	–	–	–	–	–	–	–	–	–	–	–	–	–
	60-62	119.9	10.46909	–	–	–	–	–	–	–	–	–	–	–	–	–	–
	94-96	120.24	10.48945	–	–	–	–	–	–	–	–	–	–	–	–	–	–
	128-130	120.58	10.50982	1	–	–	–	–	–	–	–	–	–	2	–	–	–
13H7	12-14	120.92	10.53018	–	–	–	–	–	–	–	–	–	–	1	–	–	–
	46-48	121.26	10.55054	–	–	–	–	–	–	–	–	–	–	2	–	–	–
	80-82	121.6	10.5709	–	–	–	–	–	–	–	–	–	–	–	–	–	–
13H-CC	11-13	121.73	10.57869	–	–	–	–	–	–	–	–	–	–	–	–	–	–
14H1	34-36	121.64	10.5733	–	–	–	–	–	–	–	–	–	–	–	–	–	–
	65-67	121.95	10.59186	–	–	–	–	–	–	–	–	–	–	–	–	–	–
	101-104	122.31	10.61342	–	–	–	–	–	–	–	–	–	–	–	–	–	–
	136-138	122.66	10.63438	–	–	–	–	–	–	–	–	–	–	–	–	–	–
14H2	18-20	122.98	10.65355	–	–	–	–	–	–	–	–	–	–	–	–	–	–
	54-56	123.34	10.67511	–	–	–	–	–	–	–	1	–	–	–	–	–	–
	91-93	123.71	10.69727	–	–	–	–	–	–	–	–	–	–	–	–	–	–
	122-124	124.02	10.71583	–	–	–	–	–	–	–	–	–	–	–	–	–	–
14H3	6-8	124.36	10.73619	–	–	–	–	–	–	–	–	–	–	–	–	–	–
	40-42	124.7	10.75656	–	–	–	–	–	–	–	–	–	–	–	–	–	–
	72-74	125.02	10.77572	–	–	–	–	–	–	–	–	–	–	1	–	–	–
	107-109	125.37	10.79668	1	–	–	–	–	–	–	–	–	–	1	–	–	–
	142-144	125.72	10.81764	–	–	–	–	–	–	–	–	–	–	1	–	–	–
14H4	23-25	126.03	10.83621	–	–	–	–	–	–	–	–	–	–	1	–	–	–
	60-62	126.4	10.85836	–	–	–	–	–	–	–	–	–	–	–	–	–	–
	94-96	126.74	10.87873	–	–	–	–	–	–	–	–	–	–	–	–	–	–
	122-124	127.02	10.8955	–	–	–	–	–	–	–	–	–	–	–	–	–	–
14H5	12-14	127.42	10.91945	–	–	–	–	–	–	–	–	–	–	1	–	–	–
	45-47	127.75	10.93921	–	–	–	–	–	–	–	–	–	–	–	–	–	–
	80-82	128.1	10.96017	–	–	–	–	–	–	–	–	–	–	–	–	–	–
	114-116	128.44	10.98054	–	–	–	–	–	–	–	–	–	–	–	–	–	–
	146-148	128.76	10.9997	–	–	–	–	–	–	–	–	–	–	1	–	–	–

APPENDIX C

>2000 µm

Sample		Depth (mbsf)	Age (Ma)	Agglutinated foraminifera (no. Grains)	Calcareous foraminifera (no. Grains)	Radiolaria (no. Grains)	Spicules (no. Grains)	Quartz (no. Grains)	Feldspar (no. Grains)	Biotite (no. Grains)	Gypsum (no. Grains)	Rock Fragments (no. Grains)	Pumice (no. Grains)	Ash (no. Grains)	Aggregates (no. Grains)	Oxidized aggregates (no. Grains)	Unidentified (no. Grains)
13H1	5-7	111.85	9.986994	–	–	–	–	–	–	–	–	–	–	–	–	–	–
	34-36	112.14	10.00436	–	–	–	–	–	–	–	–	–	–	–	–	–	–
	66-68	112.46	10.02353	–	–	–	–	–	–	–	–	–	–	–	–	–	–
	104-106	112.84	10.04628	–	–	–	–	–	–	–	–	–	–	–	–	–	–
	136-138	113.16	10.06545	–	–	–	–	–	–	–	–	–	–	–	–	–	–
13H2	20-22	113.5	10.08581	–	–	–	–	–	–	–	–	–	–	–	–	–	–
	54-56	113.84	10.10617	–	–	–	–	–	–	–	–	–	–	–	–	–	–
	84-86	114.14	10.12414	–	–	–	–	–	–	–	–	–	–	–	–	–	–
	121,5-123,5	114.515	10.1466	–	–	–	–	–	–	–	–	–	–	–	–	–	–
13H3	6-8	114.86	10.16726	–	–	–	–	–	–	–	–	–	–	–	–	–	–
	40,5-42,5	115.205	10.18792	–	–	–	–	–	–	–	–	–	–	–	–	–	–
	76-78	115.56	10.20918	–	–	–	–	–	–	–	–	–	–	–	–	–	–
	112-114	115.92	10.23074	–	–	–	–	–	–	–	–	–	–	–	–	–	–
	142-144	116.22	10.2487	–	–	–	–	–	–	–	–	–	–	–	–	–	–
13H4	28-30	116.58	10.27026	–	–	–	–	–	–	–	–	–	–	–	–	–	–
	60-62	116.9	10.28943	–	–	–	–	–	–	–	–	–	2	–	–	–	–
	64-66	116.94	10.29182	–	–	–	–	–	–	–	–	–	1	–	–	–	–
	100-102	117.3	10.31338	–	–	–	–	–	–	–	–	–	–	–	–	–	–
	132-134	117.62	10.33255	–	–	–	–	–	–	–	–	–	–	–	–	–	–
13H5	16-18	117.96	10.35291	–	–	–	–	–	–	–	–	–	–	–	–	–	–
	50-52	118.3	10.37327	–	–	–	–	–	–	–	–	–	32	–	–	–	–
	84-86	118.64	10.39363	–	–	–	–	–	–	–	–	–	–	–	–	–	–
	117-119	118.97	10.4134	–	–	–	–	–	–	–	–	–	–	–	–	–	–
	142-144	119.22	10.42837	–	–	–	–	–	–	–	–	–	–	–	–	–	–
13H6	29-31	119.59	10.45053	–	–	–	–	–	–	–	–	–	–	–	–	–	–
	60-62	119.9	10.46909	–	–	–	–	–	–	–	–	–	–	–	–	–	–
	94-96	120.24	10.48945	–	–	–	–	–	–	–	–	–	–	–	–	–	–
	128-130	120.58	10.50982		–	–	–	–	–	–	–	–	–	–	–	–	–
13H7	12-14	120.92	10.53018	–	–	–	–	–	–	–	–	–	–	–	–	–	–
	46-48	121.26	10.55054	–	–	–	–	–	–	–	–	–	–	–	–	–	–
	80-82	121.6	10.5709	–	–	–	–	–	–	–	–	–	–	–	–	–	–
13H-CC	11-13	121.73	10.57869	–	–	–	–	–	–	–	–	–	–	–	–	–	–
14H1	34-36	121.64	10.5733	–	–	–	–	–	–	–	–	–	–	–	–	–	–
	65-67	121.95	10.59186	–	–	–	–	–	–	–	–	–	–	–	–	–	–
	101-104	122.31	10.61342	–	–	–	–	–	–	–	–	–	–	–	–	–	–
	136-138	122.66	10.63438	–	–	–	–	–	–	–	–	–	–	–	–	–	–
14H2	18-20	122.98	10.65355	–	–	–	–	–	–	–	–	–	–	–	–	–	–
	54-56	123.34	10.67511	–	–	–	–	–	–	–		–	–	–	–	–	–
	91-93	123.71	10.69727	–	–	–	–	–	–	–	–	–	–	–	–	–	–
	122-124	124.02	10.71583	–	–	–	–	–	–	–	–	–	–	–	–	–	–
14H3	6-8	124.36	10.73619	–	–	–	–	–	–	–	–	–	–	–	–	–	–
	40-42	124.7	10.75656	–	–	–	–	–	–	–	–	–	–	–	–	–	–
	72-74	125.02	10.77572	–	–	–	–	–	–	–	–	–	–	–	–	–	–
	107-109	125.37	10.79668		–	–	–	–	–	–	–	–	–	–	–	–	–
	142-144	125.72	10.81764	–	–	–	–	–	–	–	–	–	–	1	–	–	–
14H4	23-25	126.03	10.83621	–	–	–	–	–	–	–	–	–	–	–	–	–	–
	60-62	126.4	10.85836	–	–	–	–	–	–	–	–	–	–	–	–	–	–
	94-96	126.74	10.87873	–	–	–	–	–	–	–	–	–	–	–	–	–	–
	122-124	127.02	10.8955	–	–	–	–	–	–	–	–	–	–	–	–	–	–
14H5	12-14	127.42	10.91945	–	–	–	–	–	–	–	–	–	–	2	–	–	–
	45-47	127.75	10.93921	–	–	–	–	–	–	–	–	–	–	–	–	–	–
	80-82	128.1	10.96017	–	–	–	–	–	–	–	–	–	–	–	–	–	–
	114-116	128.44	10.98054	–	–	–	–	–	–	–	–	–	–	–	–	–	–
	146-148	128.76	10.9997	–	–	–	–	–	–	–	–	–	–	–	–	–	–

APPENDIX D

Quartz surface texture analysis

	Sample	Depth (mbsf)	Age (Ma)	Sample ID	No. of grains described	Angluar (%)	Subangular (%)	Subrounded (%)	Rounded (%)	Low relief (%)	Medium relief (%)	High relief (%)	Chattermarks (%)	Straight steps (%)	Arcuate steps (%)	Subparallel striations (%)	Breakage blocks (%)	Conchoidal fractures (%)	Dissolution (%)	Adhering particles (%)	Chemical abration (%)	Silica precipitation (%)
13H1	5-7	111.85	9.986994	1	6	100	0	0	0	0	0	100	0	0	100	0	100	0	0	100	0	100
13H1	66-68	112.46	10.02353	2	3	0	37.5	37.5	25	50	50	0	0	37.5	25	0	62.5	87.5	87.5	25	0	100
13H1	104-106	112.84	10.04628	3	1	50	16.66667	33.33333	0	33.33333	33.33333	33.33333	0	66.66667	50	0	66.66667	83.33333333	50	16.66667	0	100
13H1	136-138	113.16	10.06545	4	8	0	100	0	0	0	66.66667	33.33333	33.33333333	33.33333	33.33333	0	100	66.66666667	0	0	0	100
13H2	54-56	113.84	10.10617	5	8	0	75	25	0	12.5	50	37.5	25	50	62.5	12.5	87.5	75	75	25	0	87.5
13H2	84-85	114.14	10.12414	6	6	16.66667	16.66667	50	16.66667	33.33333	33.33333	33.33333	33.33333333	50	50	0	50	83.33333333	66.66666667	0	0	100
13H2	121-123	114.515	10.1466	7	6	0	33.33333	66.66667	0	16.66667	83.33333	0	0	16.66667	16.66667	0	33.33333	100	83.33333333	0	0	83.33333333
13H3	112-114	115.92	10.23074	8	8	0	37.5	62.5	0	25	75	0	0	37.5	25	0	25	87.5	75	12.5	0	87.5
13H3	142-144	116.22	10.2487	9	13	15.38462	61.53846	15.38462	7.692308	15.38462	30.76923	53.84615	7.692307692	61.53846	46.15385	0	69.23077	76.92307692	30.76923077	7.692308	0	53.84615385
13H4	64-66	116.94	10.29182	10	5	20	20	40	20	20	40	40	20	40	40	0	20	100	20	20	0	40
13H5	16-18	117.96	10.35291	11	8	18.18182	45.45455	13.63636	18.18182	13.63636	45.45455	36.36364	13.63636364	45.45455	50	4.545454545	31.81818	68.18181818	45.45454545	9.090909	4.545455	68.18181818
13H5	50-52	118.3	10.37327	12	1	14.28571	35.71429	28.57143	21.42857	35.71429	42.85714	28.57143	7.142857143	28.57143	50	0	35.71429	92.85714286	35.71428571	14.28571	0	57.14285714
13H5	117-119	118.97	10.4134	13	22	12.5	62.5	25	12.5	25	62.5	25	0	50	37.5	12.5	12.5	75	62.5	0	0	87.5
13H5	142-144	119.22	10.42837	14	14	0	0	100	0	0	100	0	0	0	0	0	100	0	100	0	0	100
13H6	29-31	119.59	10.45053	15	3	0	57.14286	28.57143	14.28571	14.28571	85.71429	0	14.28571429	28.57143	28.57143	0	42.85714	71.42857143	85.71428571	0	0	85.71428571
13H6	60-62	119.9	10.46909	16	7	10	10	50	30	30	50	20	10	40	60	0	40	90	70	40	0	70
13H6	94-96	120.24	10.48945	17	10	16.66667	66.66667	16.66667	0	0	66.66667	33.33333	0	50	33.33333	0	33.33333	100	66.66666667	33.33333	0	66.66666667
13H6	128-130	120.58	10.50982	18	6	33.33333	0	33.33333	33.33333	33.33333	66.66667	0	0	33.33333	33.33333	0	33.33333	100	100	33.33333	0	100
13H7	12-14	120.92	10.53018	19	7	28.57143	42.85714	28.57143	0	28.57143	42.85714	28.57143	14.28571429	42.85714	14.28571	0	57.14286	71.42857143	71.42857143	0	0	85.71428571
13H7	46-48	121.26	10.55054	20	9	22.22222	66.66667	0	11.11111	0	55.55556	44.44444	11.11111111	88.88889	33.33333	0	44.44444	88.88888889	11.11111111	44.44444	0	33.33333333
14H1	65-67	121.95	10.59186	21	6	0	50	0	50	50	0	50	0	50	100	0	100	100	50	0	0	100
14H1	101-104	122.31	10.61342	22	9	33.33333	16.66667	50	0	16.66667	66.66667	16.66667	0	33.33333	33.33333	16.66666667	66.66667	66.66666667	83.33333333	0	0	83.33333333
14H1	136-138	122.66	10.63438	23	2	33.33333	11.11111	22.22222	33.33333	22.22222	44.44444	33.33333	0	33.33333	33.33333	11.11111111	66.66667	88.88888889	88.88888889	11.11111	11.11111	77.77777778
14H2	18-20	122.98	10.65355	24	5	0	40	60	0	20	60	20	0	60	0	0	20	100	80	0	0	80
14H2	54-56	123.34	10.67511	25	6	0	33.33333	33.33333	33.33333	16.66667	66.66667	16.66667	16.66666667	16.66667	16.66667	0	33.33333	83.33333333	100	0	0	66.66666667
14H2	91-93	123.71	10.69727	26	8	0	25	62.5	12.5	25	75	0	0	12.5	12.5	0	37.5	50	100	0	12.5	100
14H3	107-109	125.37	10.79668	27	6	33.33333	50	16.66667	0	0	50	50	33.33333333	83.33333	50	16.66666667	83.33333	66.66666667	83.33333333	0	0	33.33333333
14H3	142-144	125.72	10.81764	28	5	20	40	0	40	40	60	0	20	100	20	0	80	60	20	0	0	80
14H4	23-25	126.03	10.83621	29	10	20	40	40	0	20	40	40	0	30	30	20	60	90	60	10	10	60
14H4	94-96	126.74	10.87873	30	9	0	55.55556	22.22222	22.22222	0	77.77778	22.22222	0	11.11111	11.11111	11.11111111	44.44444	66.66666667	77.77777778	11.11111	0	77.77777778
14H5	80-82	128.1	10.96017	31	8	12.5	37.5	50	0	12.5	62.5	25	0	25	37.5	0	75	62.5	75	12.5	12.5	87.5
14H5	114-113	128.44	10.98054	32	9	0	87.5	0	12.5	12.5	25	62.5	0	37.5	25	0	87.5	75	87.5	0	0	100
14H5	146-148	128.76	10.9997	33	8	0	66.66667	22.22222	11.11111	22.22222	44.44444	33.33333	11.11111111	22.22222	22.22222	11.11111111	77.77778	66.66666667	88.88888889	0	11.11111	33.33333333